A FINITE ELEMENT APPROACH TO PREDICTING VIBROTHERMOGRAPHIC HEAT DETECTIONS OF FULLY EMBEDDED DELAMINATIONS WITHIN COMPOSITE PLATES

by

Corey Joseph Cook

A thesis submitted in partial fulfillment
of the requirements for the degree

of

Master of Science

in

Mechanical Engineering

MONTANA STATE UNIVERSITY
Bozeman, Montana

December 2012

APPROVAL

of a thesis submitted by

Corey Joseph Cook

This thesis has been read by each member of the thesis committee and has been found to be satisfactory regarding content, English usage, format, citation, bibliographic style, and consistency and is ready for submission to The Graduate School.

Dr. Ahsan Mian

Approved for the Department of Mechanical and Industrial Engineering

Dr. Christopher Jenkins

Approved for The Graduate School

Dr. Ronald W. Larsen

STATEMENT OF PERMISSION TO USE

In presenting this thesis in partial fulfillment of the requirements for a master's degree at Montana State University, I agree that the Library shall make it available to borrowers under rules of the Library.

If I have indicated my intention to copyright this thesis by including a copyright notice page, copying is allowable only for scholarly purposes, consistent with "fair use" as prescribed in the U.S. Copyright Law. Requests for permission for extended quotation from or reproduction of this thesis in whole or in parts may be granted only by the copyright holder.

Corey Joseph Cook

December 2012

ACKNOWLEDGEMENTS

My gratitude goes out to everyone who has contributed their knowledge, expertise, and resources towards assisting me with this project and thesis. Firstly, I would like to thank Resodyn Corporation for allowing me, and the rest of the research group, the opportunity and funding to work on this project. A special thanks in particular to both Peter Lucon (who served as thesis committee member) and Kyle Capp, whose collective insight, guidance, and diligence made this research possible.

Special thanks goes out to my advisor and thesis committee chair, Dr. Ahsan Mian, for all of his help in providing me the opportunity to work on this research, for his valuable insight and guidance, and for his overall support throughout my studies while at MSU. Thanks also to Dr. Douglas Cairns, for offering valuable insight and recommendations as thesis committee member.

My gratitude also to Darren Platt with whom I collaborated throughout much of this research, and who was the resounding voice and entertainment within the lab.

Thanks also to Dr. Ladean McKittrick, and Dr. Mike Edens, who both offered valuable insight and support with regards to finite element modeling at various points throughout this project.

TABLE OF CONTENTS

TABLE OF CONTENTS - CONTINUED

TABLE OF CONTENTS - CONTINUED

LIST OF TABLES

LIST OF TABLES - CONTINUED

LIST OF FIGURES

LIST OF FIGURES - CONTINUED

Figure Page

LIST OF FIGURES - CONTINUED

ABSTRACT

Vibrothermography is a Nondestructive Evaluation (NDE) technique which is particularly well suited for locating discontinuities, such as cracks and sub-surface delaminations within composite structures. The Vibrothermographic method relies on high-amplitude vibrational excitations within a structure to cause frictional rubbing along flaw surfaces. Frictional heat energy dissipated between flaw surfaces diffuses through the material of the structure to a surface where heat signatures are monitored using infra-red thermographic camera technologies. Vibrothermographic testing methods, developed in the late 1970's with the advent of improved IR camera technologies, have been somewhat slow to develop, due in part to a lack of understanding of the physics surrounding damaged areas of structures.

The focus of this research is on the use of Finite Element (FE) Analysis, using ANSYS® software, to simulate the Vibrothermographic method. One goal of the research is to produce algorithms predicting the likely-hood of thermal detection of numerous delamination flaws within a fiberglass/epoxy composite plate. The FE modeling attempts accurately characterize harmonic responses surrounding the "damaged" regions (flaw areas) of the plate. Harmonic response analyses are performed on the FE plate model, and nodal harmonic displacement data is subsequently utilized within transient analysis sub-modeling procedures. Each of the nine delamination flaws are analyzed within these sub-modeling procedures and the rates at which frictional heat energy dissipation, due rubbing, occur at the flaw faces are derived. Each delamination sub-model is subjected to a high-resolution frequency sweep analysis, where frequency dependent heat generation data is collected over a frequency bandwidth of 800-30000Hz.

The latter portion of the paper discusses the use of a novel finite element approach to estimating the likely hood of thermal detections for the flaws. The approach uses generic finite element model to predict thermal detection times for an expansive set of flaw and testing parameters. A response surface method of curve-fitting is applied to the collected detection time data, and the resulting equation is subsequently used to predict the heat-signature detectability for each flaw. The results of this method are ultimately compared to empirical vibrothermographic frequency-sweep data, and a preliminary assessment of the viability of the approach is made.

THE VIBROTHERMOGRAPHIC METHOD

Introduction to the Vibrothermographic Method

Vibrothermography is a non-destructive examination (NDE) technique used in locating areas of discontinuity, such as cracks or delaminations, within a material, based on the detection of vibration-induce frictional heating. The technique is particularly useful in identifying sub-surface flaws, such as debondings/delaminations, within composite material structures. During the vibrothermographic method, an electro-mechanical transducer is typically used to induce relatively high frequency harmonic excitations within a structure. The goal of inducing harmonic excitations within the structure is to cause areas of de-bonding, such as cracks or delaminations, to rub together in frictional contact, thus facilitating frictional heat energy dissipation. Any heat that is produced diffuses throughout the material over time. Once heat diffuses to a viewable surface, a portion of the heat energy is radiated as electro-magnetic energy within the infra-red frequency band. Infra-red (IR) thermal camera technology is utilized in an attempt to detect any heat signatures produced within the material of the structure, in hopes of identifying these hard to detect failures or manufacturing flaws. The vibrothermographic equipment utilized is represented in the schematic shown in Figure 1.

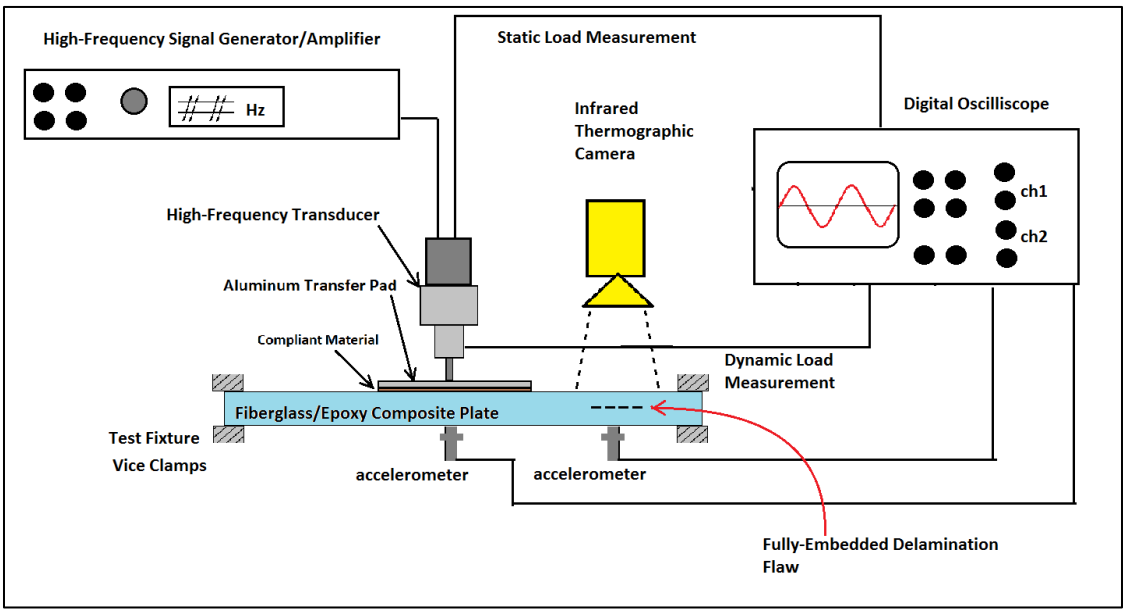

Figure 1. Schematic of Vibrothermographic System.

One of the many impediments to the wide-spread implementation of vibrothermography as a standard NDE technique is the inherent difficulty in reliably producing detectable heat generations within (initially) un-identified flaws. Even within controlled laboratory settings, the detectability of any flaw is typically affected by numerous factors such as: flaw size, flaw gap closure, inclusions within the flaw gap, excitation frequency, and IR camera sensitivities. Tests carried out in uncontrolled environments are subject to further difficulties, such as IR background noise, wind, etc. Progressive acceptance of the vibrothermographic method is also hampered by the uncertainty of the physics behind the vibration induce heat generations produced during such tests.

Vibrothermography was first extensively studied as a NDE method as early as the mid-1970's, due in part to the advent of commercially available Infra-red video camera technologies. Researches at Virginia Tech led pioneering research in this field after

discovering IR camera technology could be used to analyze structures with cracks which exhibit localized heating when subjected to high-frequency vibrational excitation. Using proper equipment, the NDE method has the ability to monitor and analyze relatively large areas within a relatively short period of time. This particular property has, no doubt, maintained the method's attractiveness as a viable NDE tool. The method is also subject to many difficulties however. One of the greatest impediments to the wide-spread utilization of the method has stemmed the lack of understanding of the interactions and responses surrounding flaws during vibrational excitation. This problem is inherent to the fact that the main goal of the method is typically to locate initially un-identified flaws. The methods by which flaws generate heat have also been investigated.

Numerous studies aiming to identify the primary modes by which heat generation is produced during vibrothermographic testing have been explored, beginning as early as the mid 1980's (cite Vtech_1986….). The effects of plastic deformation, impact (flap and chatter), and frictional slip along areas of delamination have often been proposed as being possible contributors of the vibration-induced heating.

Focus of Investigation

The primary focus of this paper is the investigation into the frequency dependence of flaw heat generations produced strictly by sliding frictional contact. It is hoped that such an analysis will provide insight into what magnitudes of heat generation may be expected when heat generation occurs solely from frictional energy dissipation (during relative sliding) along contacting flaw regions. Effects such as thermoelastic damping, may be culprit of giving false detections, especially for thin plates, during

vibrothermographic tests [1,10]. The contributions of other possible heat generation sources, such as plastic deformations and surface impact interactions will not be investigated in this document, though they may offer some contribution to the overall heat generations experienced during empirical testing. Ultimately, a routine for developing an algorithm which provides predictions of thermal detectability, and required detection times will be explored.

Difficulties in Accurately Predicting System Responses

Areas of damage existing within a material structure can significantly alter the resonant behaviors of that structure, perhaps locally, or possibly even system wide. Local resonances produced by regions of damage are dependent upon the local geometries and stress fields produced within the damaged regions [2]. Henneke proposed that heat generation patterns along flaws are dependent upon both local and system resonances. That is, the frequencies at which frictional heat generations are produced along a flaw may not be simply predicted as occurring at some resonant frequency of the transducer/sample system, but rather such predictions would depend on an intimate understanding of the response of the system around damaged areas. The combined response of local and global system resonances would be difficult, if not impossible, to anticipate without prior knowledge of the structures of the damaged areas. In this respect, as a basis for analyzing frictional heat dissipations along sub-surface damaged areas, a simplified representative model, with well-defined flaw geometries was created and analyzed. Analysis of this model is meant to serve as a preliminary attempt at quantifying frictional heat generations along fully embedded delaminations.

IMPLEMENTING FINITE ELEMENT MODELING AND EMPIRICAL TESTING TO CHARACTERIZE VIBRATIONAL HEAT GENERATION ALONG EMBEDDED FLAWS

Introduction to Design Layout and Construction of the 24”x16”x0.54” Fiberglass/Epoxy Plate and Accompanying Finite Element Models

Finite element models representing the plate geometries of a 24”x16”x0.54 fiberglass/epoxy composite plate were constructed via ANSYS Classic APDL; the models were created in an attempt to characterize and estimate the frictional heat generations occurring along numerous embedded flaws present within such a plate during empirical vibrothermographic testing procedures. The overall size and layout of the plate geometries were agreed upon between Resodyn Corporation and the MSU research group prior to beginning FEA modeling procedures and prior to the actual physical plates being constructed or tested. The design of the plate was purposely tailored to enable both the manufacture of the physical plate, and the creation of the finite element models to be completed in an efficient and feasible manner.

Throughout the process in which the 24”x16”x0.54” was designed, constructed, modeled and tested, numerous discrepancies between the modeled and physical plates were inadvertently introduced. The details of these discrepancies will be introduced early on as a primer for more detailed discussions later in this document. The proposed design and layout of the plate will first be discussed, followed by a discussion of the final geometries of the actual physical sample created, and finally by a discussion of the ANSYS finite element models. The simplifying assumptions made therein will also be

discussed; discrepancies between the modeled plated and physical manufactured plate will be pointed out wherever relevant.

Proposed Plate Design

The final proposed design of the composite plate, measuring 24”x16”x0.54” was to include nine separate flaws, occurring as fully embedded delaminations oriented at various points within the plate. As a matter of simplifying both the construction and modeling procedures of such a plate, all nine of the flaws were introduced as completely inter-laminar delaminations. That is, the delaminations occur only between laminate layers and don’t propagate transversely through any fiber-layers. To simplify the finite element modeling of the plate and flaws, rectangular flaw surface geometries were specified so that the entire plate could be meshed with an accurate, high quality, hexahedral brick mapped Finite Element mesh.

The nine rectangular (square) flaws can be separated into three different groups, with each individual group containing a specifically sized flaw. The first flaw group contains three 2”x2” flaws, the second group contains three 1”x1” flaws the third and final group contains three ½”x ½” flaws. All nine flaws occur as fully embedded delaminations, positioned at various locations and depths within the plate. The final proposed layout of the composite plate is displayed in a dimensioned CAD drawing, as provided by Resodyn Corporation., in Figure 2.

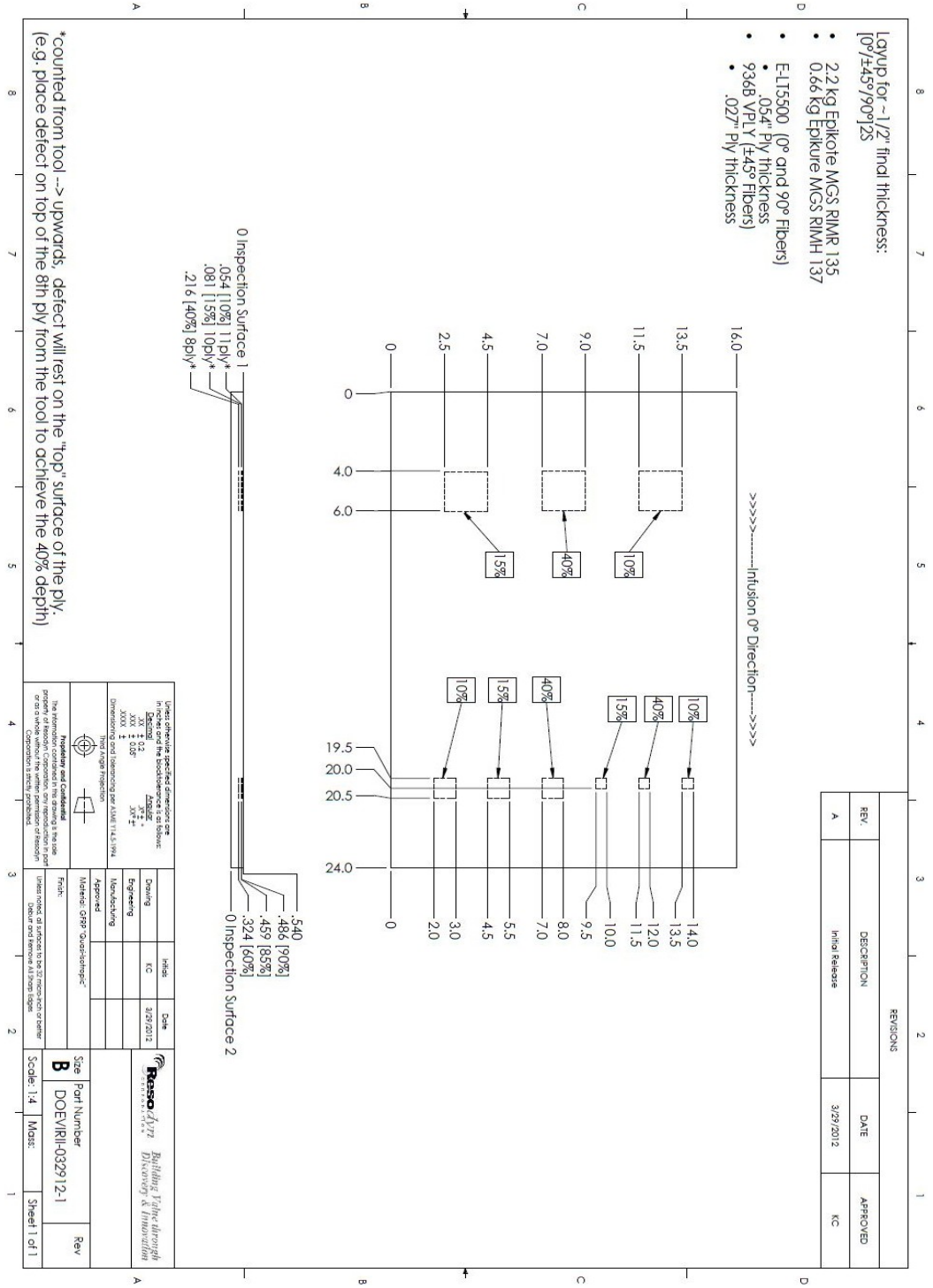

Figure 2. Detailed cad drawing of the 24”x16”x0.54” Fiberglass/Epoxy composite plate with included delamination flaws. Courtesy of Resodyn Corporation.

This proposed design, shown in the above figure, was the basis from which both the manufactured plate sample and the FE plate model were created.

Manufactured (Physical) Plate

The test sample manufactured by Resodyn Corporation was constructed using vacuum-bagging techniques, with one side of the plate laid up upon a tool surface, and the other exposed to plastic vacuum bagging. The focus of this paper isn't necessarily on the methods and procedures by which the plate was constructed, but rather the Finite Element modeling of such a plate, therefore many details of the plate construction are omitted from this document.

The manufactured plate was constructed from Epikote MGS RIMR 135 epoxy, with a combination of E-LT5500 (0° and 90°) and 936B VPLY (±45°) fibers. The Composite plate layup is described by a lamina order of [0°/±45°/90°]2S resulting in a total laminate plate thickness of 0.54 inches. The detailed layout of the plate is outlined in the dimensioned CAD drawing shown in Figure 2 above.

In order to produce the nine fully embedded delaminations of the model, small slips of polyurethane film (0.006" thickness) were sandwiched and taped together. The polyurethane slip pairs were taped together using a masking tape (0.005" thick) by folding the masking tape around the edges of the polyurethane. These polyurethane layers were added at various locations and depths within the composite plate layup during manufacturing in order to introduce regions which approximately rectangular delaminations. An illustration depicting how the polyurethane slip pairs were constructed is shown in Figure 3 below.

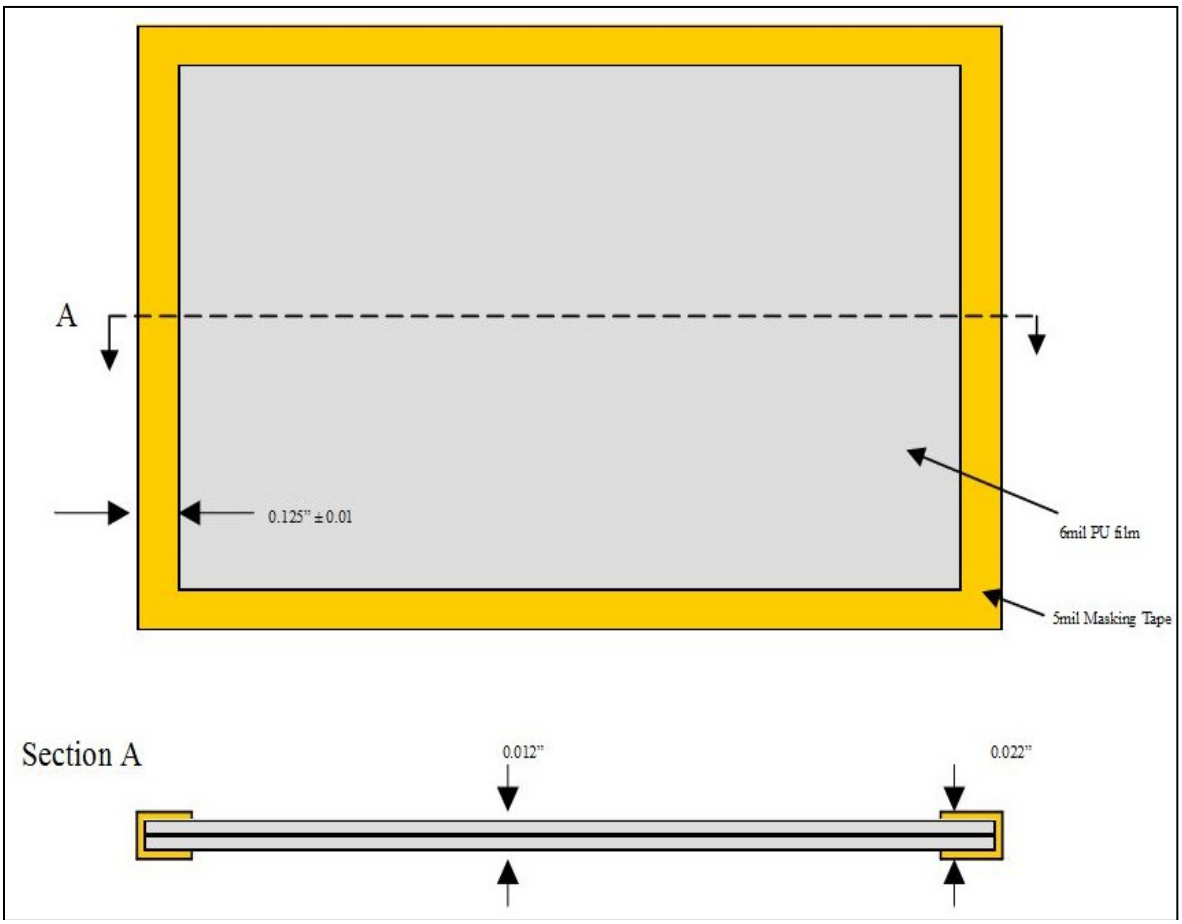

Figure 3. Each delamination in the plate was created by including polyurethane slips in the plate layup during manufacturing procedures. Courtesy of Resodyn Corporation.

The purpose for using the polyurethane film inclusions was to facilitate the introduction of delaminations of well-defined geometry. Reliably and consistently creating rectangular delamination areas within a composite plate such as this can be extremely difficult, especially when trying to maintain initially closed contact (essentially zero gap) between the delamination surface pairs. Originally the proposed plate design assumed that the delaminations would occur as simple un-bonded, rectangular areas between plate layers; the delaminations would simply be void space within the composite plate. Creation of such fully-embedded flaws with precise geometry is extremely

difficult. Instead the urethane slip pair method was employed. Figure 4 below shows a visual of the manufactured plate with polyurethane slip inclusions clearly visible through the epoxy/fiberglass material.

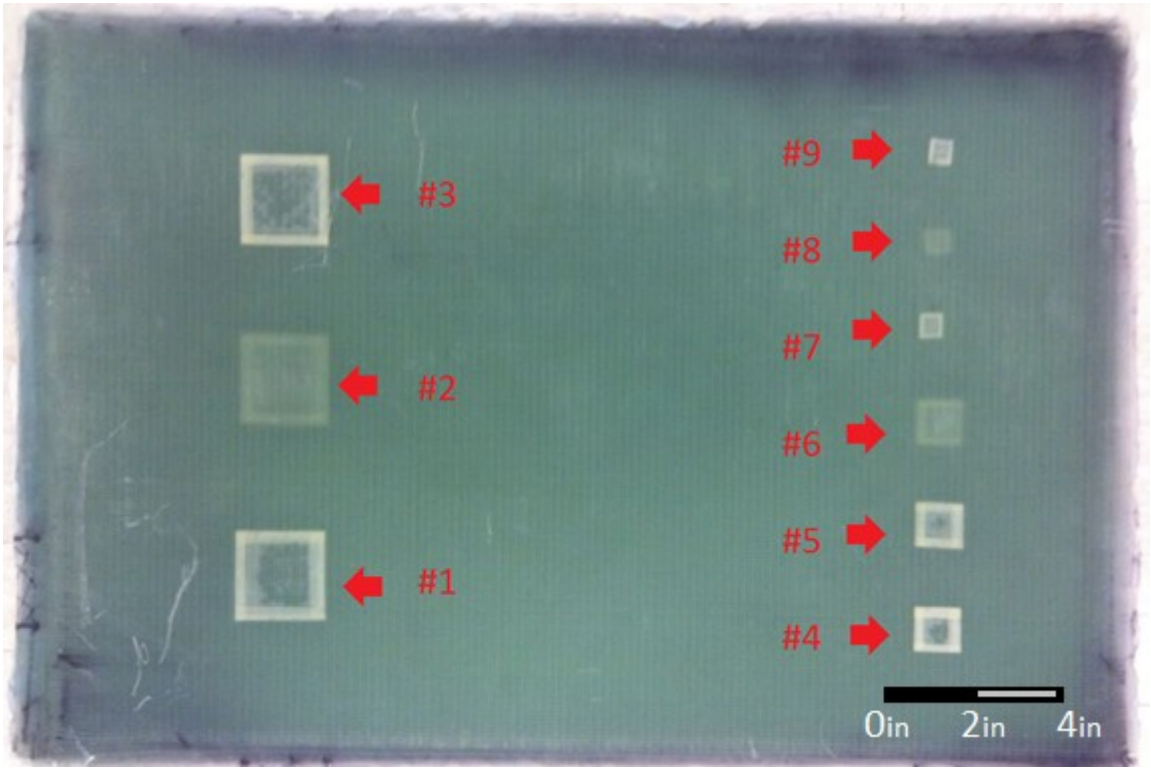

Figure 4. Fiber-Glass composite plate (24”x16”x 0.54 “), with nine separate embedded de-laminations.

Each of the three groups of inclusions contains flaws at three different depths, measured from the top surface of the plate. Each of the nine flaws has been assigned a number, as shown in the figure above; this flaw numbering will be used to reference each of the flaws throughout the remainder of this document.

An additional discrepancy between the proposed plate design and the actual manufactured plated was introduced after the manufactured plate was trimmed to size. After completion of the vacuum-bag molding process, the overall size of the plate was

greater than the proposed geometries, and the edges of the plate were non-square and inconsistent. Concerns were raised as to whether the untrimmed edges would negatively affect attempts to validate results between tests of the physical manufactured plate and results of the finite element plate model. The plate was therefore trimmed in order to square the edges; however the final width of the plate was reduced from 16" to 15.5". This reduction in the dimensions of the plate geometry will have affected the stiffness of the plate, which will subsequently affect the modal and harmonic responses of the plate.

Finite Element Model of Plate

The finite element model created with ANSYS classic APDL code, was based on the agreed upon plate design. The material properties of the fiberglass/epoxy composite plate, which were measured as (bulk) orthotropic properties, were supplied by Resodyn for the purposes of the FE analyses. In the FE models, the material properties were also assigned as orthotropic properties. A simplifying assumption was made with regards to modeling the plate; in this approach, rather than modeling the large plate as a series of stacked laminae, with varying unidirectional fiber orientations, the laminate plate was modeled as a monolithic material structure with assigned orthotropic material properties. The decision to model the composite laminate plate as a monolithic structure was made in order to drastically simplify the model construction. Modeling of alternating layers within a laminate plate would introduce significant complexity to the model and was therefore omitted from this analysis. The material properties assigned to the plate are provided for reference below in Table 1.

Table 1. Material Properties Employed within Structural FEA Model

Material Property		**Units**
ρ	1876	kg/m^3
ν	0.34	Poisson's Ratio
E_x	19.6	GPa
E_y	19.6	GPa
E_z	8.8	GPa
G_{xy}	6.4	GPa
G_{yz}	4.1	GPa
G_{xz}	4.1	GPa

The material properties (some orthotropic) presented in the table above are mass density, Poisson's ratio, Young's modulus, and shear modulus, respectively. Additional material specific properties, such as frictional coefficients and damping ratio, were either inferred from published articles or determined through empirical testing; determination of such properties will be discussed later in this document when appropriate.

Creation of the nine delamination flaws within the FE model was accomplished by creating coplanar areas which share both key-points and lines along their outer edges, but which do not share lines and key-points along their interiors. Creating the flaws in this manner assumes that adjacent flaw surfaces are initially coplanar (and hence, are initially completely in contact) along their surfaces. The validity of this assumption of initial co-planarity will be explored further later in this document when discussing static pre-loading of the plate. This method assumes that there are no other materials present between adjacent flaw surfaces (void).

It must be noted that this assumption varies drastically from the method by which the flaws in the manufactured plate were actually created. The introduction of foreign materials, such as the tapes, was not anticipated during the finite element model design.

In fact, if such a system was to be accurately modeled using finite element methods, the required total computational analysis time would likely be increased exponentially; the introduction of such materials drastically increase the complexity of the finite element model design, since implementation of dynamic contact regions (contact/target elements) would be required at all of the tape inclusion boundaries. Properly modeling such interactions between the foreign materials (polyurethane and masking tapes) and the monolithic plate structure would require defining complex Contact/Target interaction elements between all material interfaces. Implementation of Contact/Target elements leads to computationally intensive analyses, especially in the case where highly refined meshes are required (as is the case in these analyses, which will be discussed later).

In this regard, the modeled flaw surfaces were created as simple void (zero-gap) spaces between adjacent flaw surface pairs. As was mentioned at the beginning of this section, the rectangular flaw design was incorporated in order to allow for high-quality, accurate, mapped-brick meshing to be attained within the models. Utilization of mapped brick (hexahedral element) meshing within dynamic structural analyses is desirable when compared to using tetrahedral elements. Non-hexahedral element meshes are typically less accurate than hexahedral meshes within structural analyses since tetrahedral meshes tends to cause the modeled material to behave as un-realistically "stiff" when compared to high-quality hexahedral meshes. Using tetrahedral free-meshing would require more mesh refinement, which would in turn significantly drive up the computational costs of subsequent analyses.

Selection of an Appropriate ANSYS Element Technology

A solid element model using ANSYS SOLID 185 (3-D 8-Node Structural Solid) elements was created for the 16" x 24" x 0.54" plate. ANSYS suggests using 8-Node brick elements when performing finite element analyses dealing with wave propagation, or transient dynamic response for that matter. Other finite element meshing methods, such as elements supporting mid-side nodes, or exhibiting geometric degeneracy (degenerating to tetrahedral elements for example) can cause unbalanced mass distribution among element nodes, causing inaccuracies in the calculations of transient or harmonic responses; for these reasons in particular, the ANSYS SOLID-185 structural solid element was chosen. This element type supports translational degrees of freedom in three directions at each node and was utilized in calculating the structural responses of the plate due to harmonic loadings. The heat generation along flaw surfaces was derived from the structural responses and contact interactions occurring along such surfaces. In order to incorporate these contact interactions, special "contact" elements were implemented

When using ANSYS's implicit solver modules, complex contact interactions between modeled solid bodies are not automatically recognized or accounted for. Proper modeling of contact interactions through ANSYS typically requires the implementation of contact and target element regions. When contact/target elements are not properly employed within contact regions, body penetrations occur, and the stresses and forces which should be realized due to such contact interactions are completely ignored. For the purposes of the FE models explored in the research documented here, ANSYS's

"Conta173" and "Targe170" contact element technologies were used. These contact element pairs allow for 3-D, 4 node surface-to-surface contact [3]; the use of ANSYS SOLID 185 elements throughout the underlying solid model necessitates the use of 4 node contact elements. One major drawback to using ANSYS software in analyses which model transient contact interactions is that contact regions must be anticipated prior to the analysis, so that such regions may be meshed using contact/target element technologies ahead of time.

The ANSYS FE software package also offers an additional explicit-dynamics module; the module is paired with LS-DYNA explicit-dynamic solver technologies. The ANSYS LS-DYNA modules allows for the use of LS-DYNA structural elements, which are able to automatically incorporate surface-to-surface contacts, without the use of additional contact/target element meshing. The explicit solvers do not lend themselves well however, to use in transient high-frequency periodic, or harmonic analyses.

Defining Element Mesh Sizing

The finite element models were meshed by first defining the element mesh densities through ANSYS APDL code. The mesh was refined in order to provide at least 20 solid elements along the minimum expected wavelength (of the applied harmonic excitation frequency) within the model. ANSYS element technology literature suggests that at least 20 solid elements should occur across each wavelength in order to properly approximate wave propagation within a 3D solid model. The longitudinal wavelengths corresponding to the harmonic excitations were calculated [4] as:

$$\text{Wavelength} = \frac{C}{freq}$$

Equation 1

Where: C = Speed of sound through the material, m/s

freq =Harmonic excitation frequency, Hz

The speed of acoustic wave propagation (compressional) through the material, C is defined as:

$$C = \sqrt{\frac{E * (1 - \nu)}{\rho * (1 + \nu)(1 - 2 * \nu)}}$$

Equation 2

Where: E= Young's modulus (orthotropic),Pa

v= Poisson's ratio

ρ= density of material, kg/m^3

Utilizing the estimated material properties for the composite (as supplied by Resodyn Corporation; shown in Table 1), the minimum expected wavelength was calculated. During the FE modeling procedures, the assumption was made that the force transmitted unto the plate by the ultrasonic force transducer was imparted through a perfectly coupled, impedance-balanced region, resulting in a perfectly coupled (thus perfectly harmonic with no frequency superposition) transmission of the harmonic excitation energies. The highest frequency of interest, 30,000Hz was used in conjunction with Equation 1 & Equation 2 to calculate the minimum wavelength expected within the material structure during empirical testing.

$$\text{Wavelength} = \frac{\sqrt{\frac{8.89E9 * (1 - 0.34)}{1876 * (1 + 0.34)(1 - 2 * 0.34)}}}{30000Hz} \qquad \text{Equation 3}$$

$$= 0.090024meters$$

The maximum finite element edge length, for an accurate modal or harmonic analysis, was then calculated as:

$$e\_size = \frac{wavelength}{20} \qquad \text{Equation 4}$$

$$e\_size = \frac{0.090024meters}{20\ element}$$

$$= 4.5012\ mm$$

With the maximum element edge length calculated, the solid body model of the plate was meshed accordingly with a hexahedral mapped-brick mesh. Finally, the delamination regions were overlaid with the selected contact/target element combos in order to account for contact interaction phenomena experienced along the flaw sites.

The total solid-element count for the meshed full-scale plate model was typically around 70,000 8-node brick elements, with 86,000 nodes. The meshed plate is displayed in Figure 5 below; the fully-embedded delamination surface pairs are visible as well,

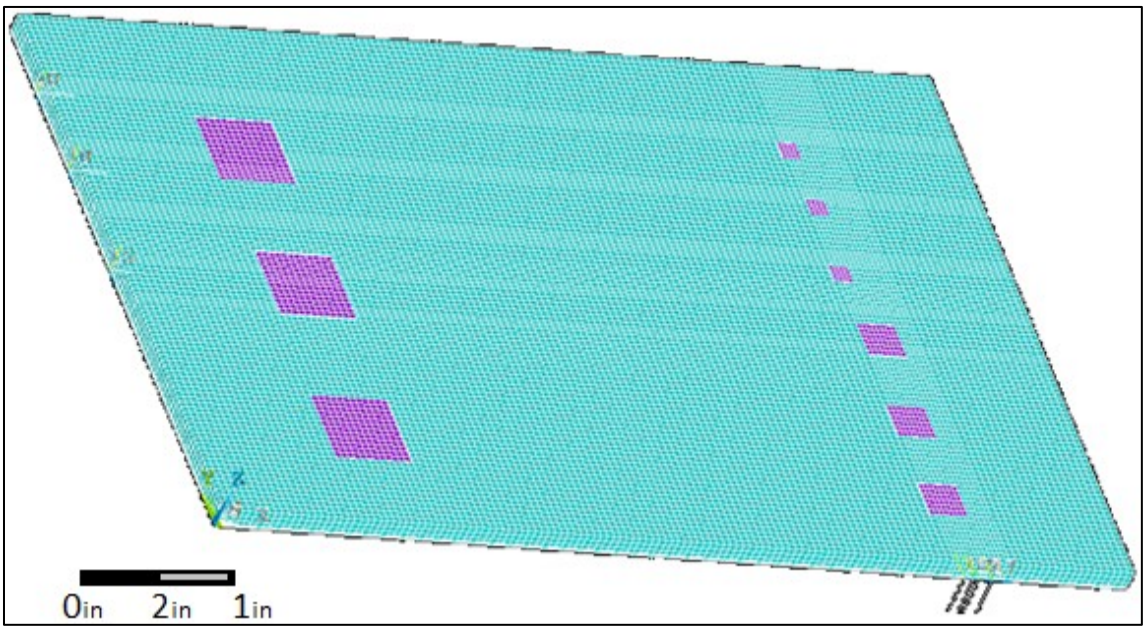

Figure 5. Map-meshed plate model with all nine delamination areas (contact/target elements) displayed for reference.

The flaw surface pairs (shown in purple in the figure above), were created by overlaying Contact/Target element pairs of "Conta173" and "Targe170" over the underlying meshed solid structural SOLID185 elements. The flaws displayed within the purple regions in the figure above occur at varying depths within the plate, as outlined in Figure 1.

Noted Discrepancies Between FE Models and Manufactured Plate

Up to this point, numerous discrepancies between the FE modeled plates and the manufactured plate have been pointed out; the discrepancies were inadvertently introduced throughout independent developments in the project. The most significant difference between the FE modeled plates and the manufactured plate is in the manufactured plate's inclusion of polyurethane tape slip pairs, used in the creation of the numerous rectangular delamination surfaces. The presence of such inclusions will no

doubt affect the local system responses at those points, and may even significantly affect the overall frequency dependent response of the plate/transducer system. Secondly, when the plates were trimmed in order to square edges and refine the geometry of the plate, the overall width dimension of the plate was altered from the original design specifications of 16in width. The trimming of the plate edges resulted in the width being reduced from 16inches to 15.5inches.

Furthermore, some broad simplifications of the plate construction were assumed within the FE models. In an attempt to simplify the construction of the FE models, the composite plate was modeled as a monolithic material structure (albeit the introduction of delaminations), rather than a series of adjacent composite lamina layers. Assuming a monolithic structure, the bulk material properties of the model were applied as orthotropic properties, corresponding to each of the primary global coordinate axes of the model.

During the analyses performed on the plate model (which will be discussed throughout this document, the force applied to the model through a virtual high frequency transducer was assumed to occur as a uniform, area specific, sinusoidal (varying with time) distributed force load .The application of uniform spatially averaged forces onto the FE plate is also a gross over-simplification of the actual interactions that are expected to occur between the manufactured plate and the high-frequency force transducer system. The un-bonded contact which exists between the plate and the force transducer system, in conjunction with the mismatch of mechanical impedance across the interface, leads to a less than ideal transmission of energy across the boundary (at certain frequencies) . These factors may lead to uncoupling between the plate and the transducer, as will be

shown in empirical data. It is important that these discrepancies between the physical plate and the FE models be clearly stated, if a reasonable evaluation of the quality and applicability of the methods employed in this research is to be made.

ESTIMATION OF ADDITIONAL MATERIAL PROPERTIES AND BEHAVIOURS FOR USE IN FINITE ELEMENT MODELING

Determination and Assumption of Additional Material Properties and for FE Modeling

The material properties used in the FE modeling of the plate are assumed as bulk orthotropic properties. As was mentioned earlier in this document, the plate was modeled as a monolithic structure (with internal flaws introduced), and individual laminae were not considered. In this regard, the material properties applied to the FE model represent the bulk moduli of the material; the various material properties and moduli were tested for and measured by Resodyn Corporation using representative samples of the fiberglass/epoxy used in the creation of the manufactured plates. Many of the material properties attributed to the models are outlined in Table 1, which were used in the calculations of minimum acoustical wavelength within the material structures.

In order to carry out the kinematic analyses performed throughout this document the additional system/material behaviour of damping also had to be considered. In order to approximate the damped structural response of the FE modeled plates, the structural damping ratio, or loss factor experienced within the plates was estimated through empirical testing. These tests were performed at Resodyn in conjunction with the MSU research group.

Implementation of Damping within FE Models

In kinematics, assumptions of system damping are often made when analyzing the modal or vibrational responses of discretized material systems. However, in reality when dealing with vibrating continuous systems, making reliable estimates of damping parameters which properly characterize the behaviour of those systems is often times quite difficult. In order to characterize the response of the system analyzed in this research through the use of Finite Element analysis, system damping had to be explored. The first step in determining how damping should be implemented was to identify the damping models supported by ANSYS.

The use of ANSYS FEA software allows damping to be implemented in two different ways. The first method, which relies on implementing Rayleigh damping parameters, is used in transient analyses and requires that two system dependent damping parameters be supplied to the model; the two Rayleigh damping parameters are denoted as α and β, which are the mass damping multiplier and stiffness matrix multiplier respectively. Application of damping using this method is used within ANSYS's transient structural analyses.

Another method by which damping may implemented into ANSYS models is via damping ratio, which is easily implemented within steady-state vibrational analyses such as modal and harmonic structural analyses. Damping ratio, ζ, is a non-dimensional quantity which represents the ratio between the actual damping value of the structure and the critical damping of the structure

$$\zeta \equiv \frac{c}{c_{cri}} \qquad \text{Equation 5}$$

This ratio is a considered system property, not a material property. The damping ratio for the relatively stiff and brittle composite plate explored here, which will be subject to rigidly clamped boundary conditions would be expected to be fairly small, representing an under-damped system ($\zeta<1$). This is precisely what is determined from the results of the following sections discussing damping ratio measurement.

Assuming steady-state vibrational conditions, the equations of motion of each degree of freedom in the discretized model (representing the continuous physical plate) can be represented by the following equation.

$$m\ddot{x} + c_{eq}\dot{x} + kx = F_o e^{i\omega t} \qquad \text{Equation 6}$$

Where the viscous damping matrix, c_{eq} can be represented by:

$$C_{eq} = \alpha M + \beta K \qquad \text{Equation 7}$$

Where: α= Rayleigh Mass Matrix Multiplier

B= Rayleigh Stiffness Matrix Multiplier

M= Mass Matrix

K= Stiffness Matrix

The values of α and β are not readily measured with typical testing procedures and are basically just mathematical tools which allow for the approximation of damping within structures. The actual physics behind structural and material damping typically are not well known. However, an estimation of the system's damping can made in the form of damping ratio, ζ. This damping ratio is readily measured using various testing and measurement techniques. Once measured, the damping ratio may be used in

conjunction with estimated modal frequencies (derived from ANSYS Modal analyses) to estimate the Rayleigh damping parameters α and β, for use in transient analyses. The values of α and β are estimated over specific frequency ranges by first measuring damping ratio at any two modal frequencies, let's say the k_{th} and m_{th} modes. The Rayleigh damping parameters can then be solved for within the following equations [5]:

$$\alpha + \beta\omega_k{}^2 = 2\omega_k\zeta_k \qquad \text{Equation 8}$$

and

$$\alpha + \beta\omega_m{}^2 = 2\omega_m\zeta_m \qquad \text{Equation 9}$$

since the resonant modal frequencies and damping ratios at those resonant frequencies can be identified and measured directly during testing.

Reliance on Rayleigh damping results in an approximately constant damping ratio being applied at modal frequencies occurring at the mid-point between the resonant k_{th} and m_{th} modal frequencies; while damping ratio increases around both the higher and lower modal frequencies. In order to specify both α and β given a measured value of ζ over the frequency range from ω_k and ω_m the following relationships are utilized.

$$\alpha = 2\zeta\frac{\omega_k\omega_m}{\omega_k + \omega_m} \qquad \text{Equation 10}$$

$$\beta = \frac{2\zeta}{\omega_k + \omega_m} \qquad \text{Equation 11}$$

where the applied value of ζ has been found taking the average of the values ζ_k and ζ_m [6]. Estimations for damping ratio, ζ, were experimentally determined at numerous resonant frequencies across the 0-30kHz bandwidth. The methods used in estimating those damping ratios will be discussed next.

Testing for Damping Ratios using the Half-Power Bandwidth Method.

Measuring small values of damping ratio over a large frequency bandwidth, 0-30kHz for the purpose of this research, requires a testing procedure which is able to accurately measure the necessary test variables even at relatively high frequencies. In order to meet the requirements of this testing the Half-Power Bandwidth method was employed. Half-Power bandwidth is a method used to measure and quantify very small damping within material structures. The method relies on identifying the amplitude of a resonant response peak (and its corresponding frequency), and from this amplitude information, inferring half-power response amplitudes (Equation 12):

$$A_{half} = \left(\frac{1}{\sqrt{2}}\right) \times A_{max} \qquad \text{Equation 12}$$

The half-power responses and their corresponding frequencies can then be used in Equation 13 (below) to estimate the damping ratio of a single-degree-of freedom viscously damped system [7]. Figure 6 below shows the plot of power or amplitude versus frequency.

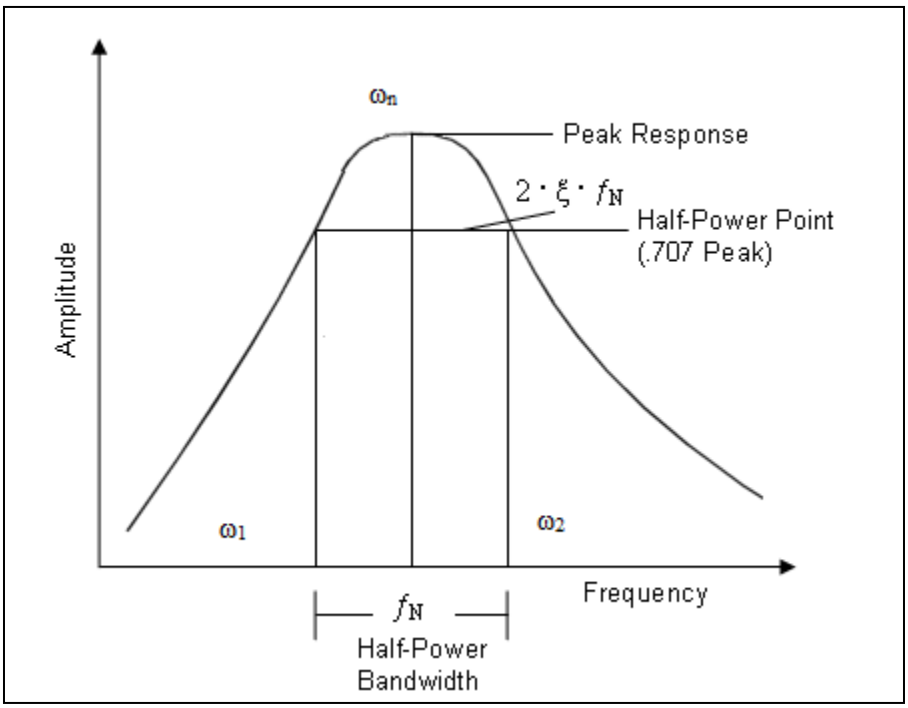

Figure 6. Illustration of Half-Power Bandwidth Method for use in damping ratio testing.

After identifying the resonant peak frequency and measuring the frequencies at the half power amplitude, the factored damping ratio may be ascertained.

$$2\zeta = \frac{\omega_2}{\omega_n} - \frac{\omega_1}{\omega_n} \qquad \text{Equation 13}$$

By further simple algebraic manipulation one can find ζ.

Testing for viscous damping ratios of the 16”x24”x 0.54“ plate was performed at Resodyn Corporation. The center of the manufactured plate was excited with the high frequency transducer in order to induce harmonic response within the plate, while displacements normal to the plate surface (z-direction) were measured via a single axis accelerometer. The accelerometer was placed on the side of the plate directly opposite of the transducer. Resonant peaks of the plate’s harmonic response were identified by analyzing acceleration data measured by the accelerometer with a digital oscilloscope.

Figure 7 shows a simplified schematic of the plate/transducer testing setup which was used during damping ratio testing.

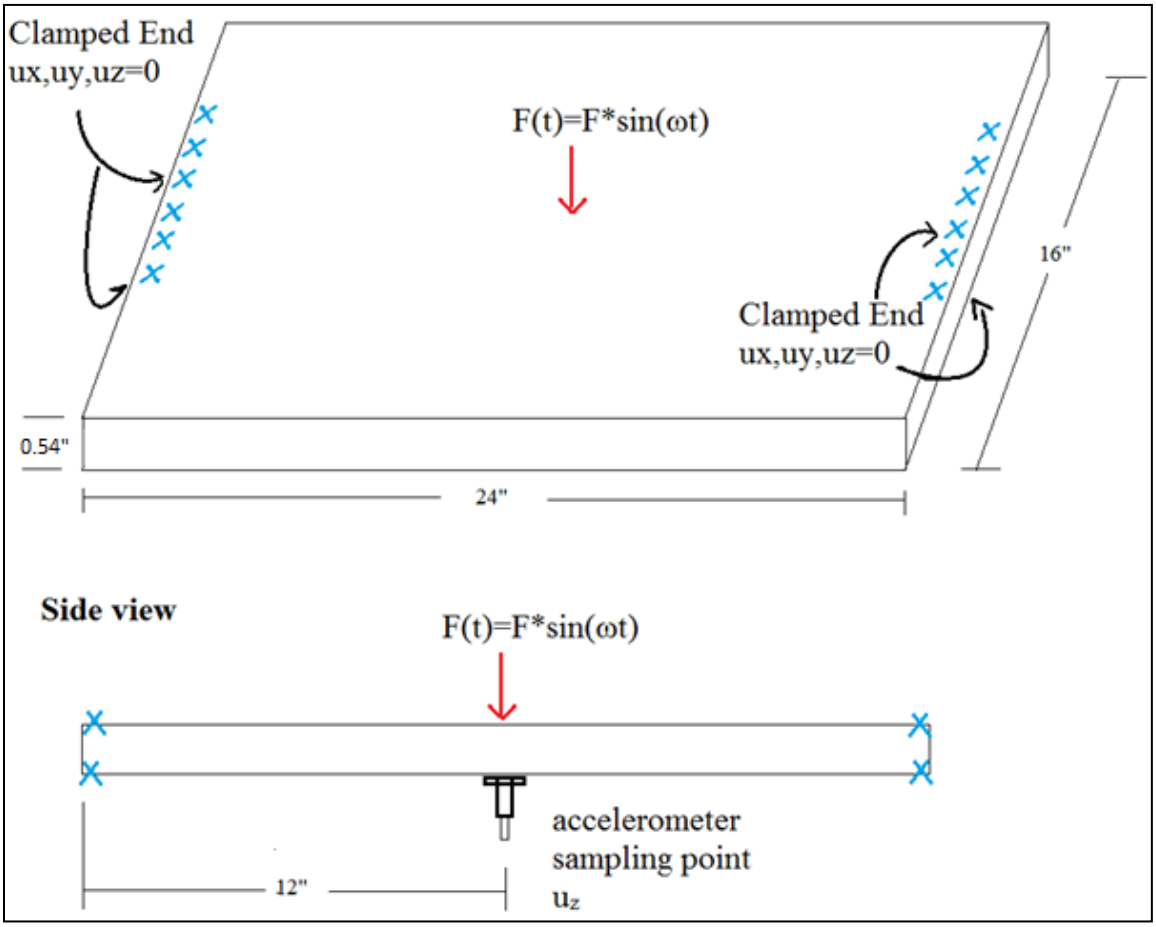

Figure 7. Simplified schematic of 24”x16”x0.54“ composite plate with clamped ends imposed, along with sinusoidal excitation force at transducer.

Actual pictures of the high-frequency force transducer system, and other equipment used during testing, are omitted from this document in order to mitigate violations of intellectual property agreements. A simplified representation of the high-frequency transducer at the point of application of the plate is shown in Figure 8 below.

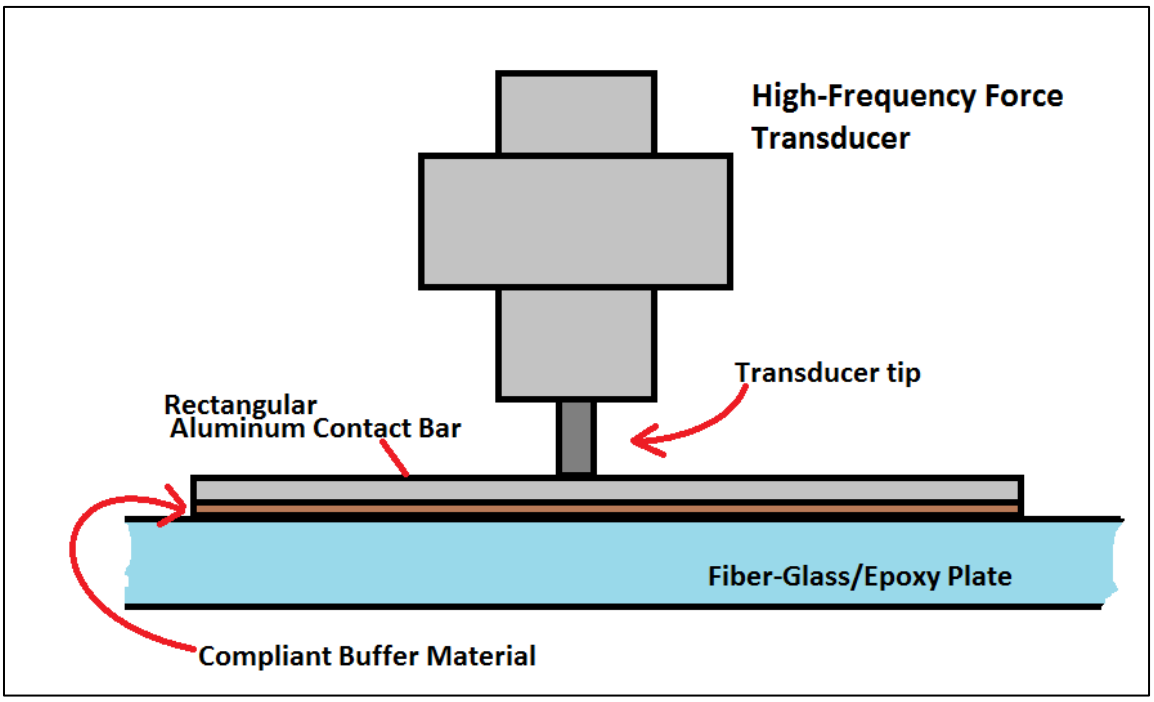

Figure 8. Schematic of high-frequency transducer and contacting pad system.

During damping ratio testing, the digital oscilloscope was utilized to analyze the harmonic response of the plate sampled at the uni-axial accelerometer. Placement of the accelerometer at the opposite side of the plate as the high frequency load transducer was chosen in order to approximate the response at the transducer tip. The accelerations measured at the accelerometer point were read by the oscilloscope as a periodic voltage signal, which was in turn converted to an acceleration value by use of the instrument's sensitivity data curve. The sensitivity of the accelerometer used for this testing was 1.923 *g* per millivolt (where the unit *g* represents standard gravity, or g-force, which is equivalently 9.81 meters/second^2). Figure 9 below shows an example of the oscilloscope readout for the accelerometer (cyan signal) and for the dynamic force transducer (magenta signal) at a driving frequency of 10.379kHz.

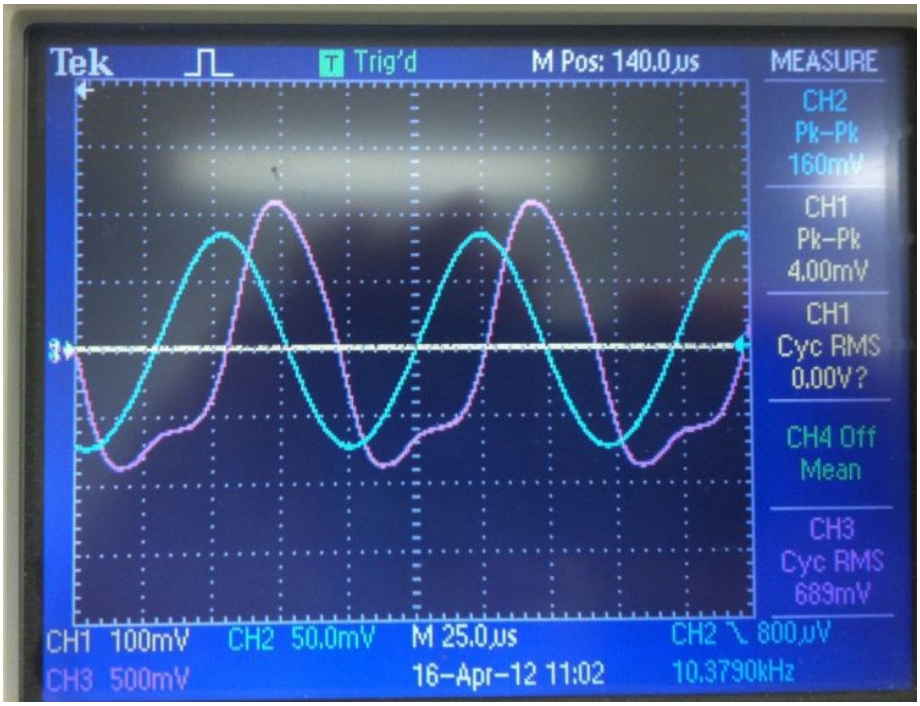

Figure 9. Oscilloscope instrumentation signal read-out. The cyan data represents accelerometer response, while the magenta curve represents load transducer force data.

An example calculation, showing how acceleration values were estimated from these measurements will now be demonstrated. The reading of 160mV peak-to-peak, from the figure above, corresponds to an acceleration amplitude of 153 g. Equation 14 gives an example of such a calculation:

$$Acceleration, \text{a} = \frac{Voltage}{2} * Sensitivity \qquad \text{Equation 14}$$

$$a = \frac{160mV}{2} * 1.923 \frac{g}{mV}$$

$$= 153.84\ g$$

$$= 1509.2\ m/s^2$$

From the oscilloscope readout above, the periodicity of the instrument signals is apparent, however, the magenta signal (transducer force being applied to plate)

shows a non-sinusoidal wave-form. It has been assumed that during these empirical tests the transducer and plate interface begins to un-coupled at certain frequencies (the possibility of which had been suggested earlier in this document) . This uncoupling at the transducer interface is observed to occur even though both a considerable pre-load force between the plate and transducer is applied, and a compliant buffer material is applied between the transducer and plate. The inclusion of the compliant buffer material may explain why more abrupt impact phenomena are not discernible in the time-history of the force signal.

One problem that was encountered while testing for damping ratios was the superposition of resonant frequency bandwidths. In other words, when a resonant peak was identified often times its corresponding half-power response points could not be easily identified, since the super-position of other resonant responses often occurred. The phenomenon may be more clearly demonstrated in the representative frequency dependent acceleration amplitude plot shown in Figure 10 below. The ω_{n1} and ω_{n2} represent the frequencies at which resonant frequency peaks occur, while the values ω_1 and ω_2 represent the respective half-power frequencies (only 1 for each in this case).

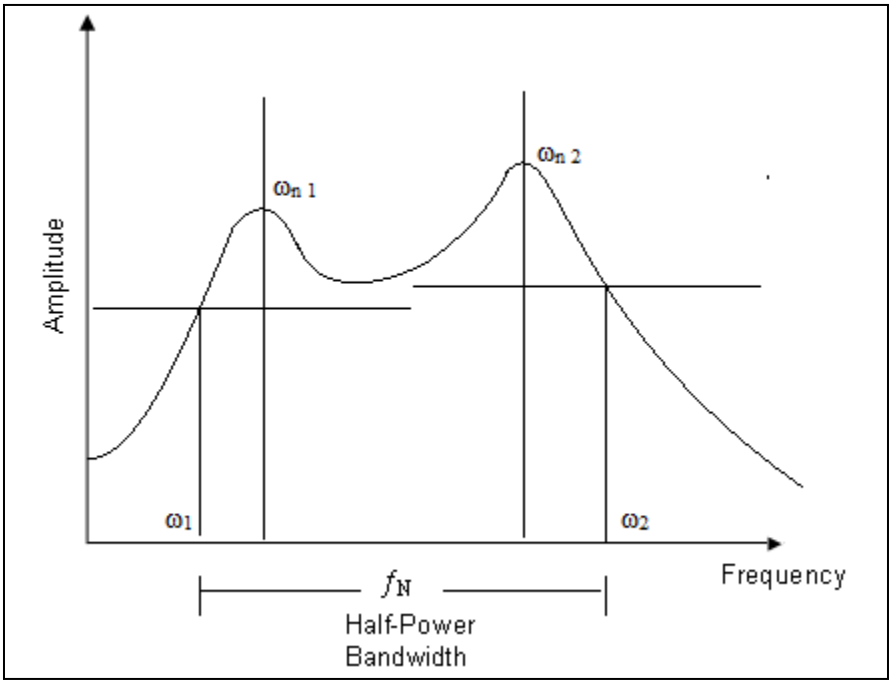

Figure 10. Superimposed resonant peaks, and corresponding Half-Power Bandwidth Method.

In such cases, approximations of the half-power points were assumed in a manner as described here. The damping ratio zeta was approximated via Equation 15 below:

$$2\zeta = \frac{\omega_2}{\omega_{n2}} - \frac{\omega_1}{\omega_{n1}} \qquad \text{Equation 15}$$

where ω_1 and ω_2 were extracted from either side of the peaks of the superimposed acceleration curves (as shown in Figure 10 above). This approach leads to a rough approximation of the half power frequencies in such cases. In some instances super position of as many as 4 or 5 resonant response peaks occurred; in such cases, the results were deemed ambiguous.

Damping ratio values for the 24”x16”x0.54” plate were estimated in this manner over a frequency band of 600Hz- 30,000Hz, the results of which were plotted in

Microsoft Excel® and are shown in Figure 11below. Data points were collected only where significant resonant responses were identified.

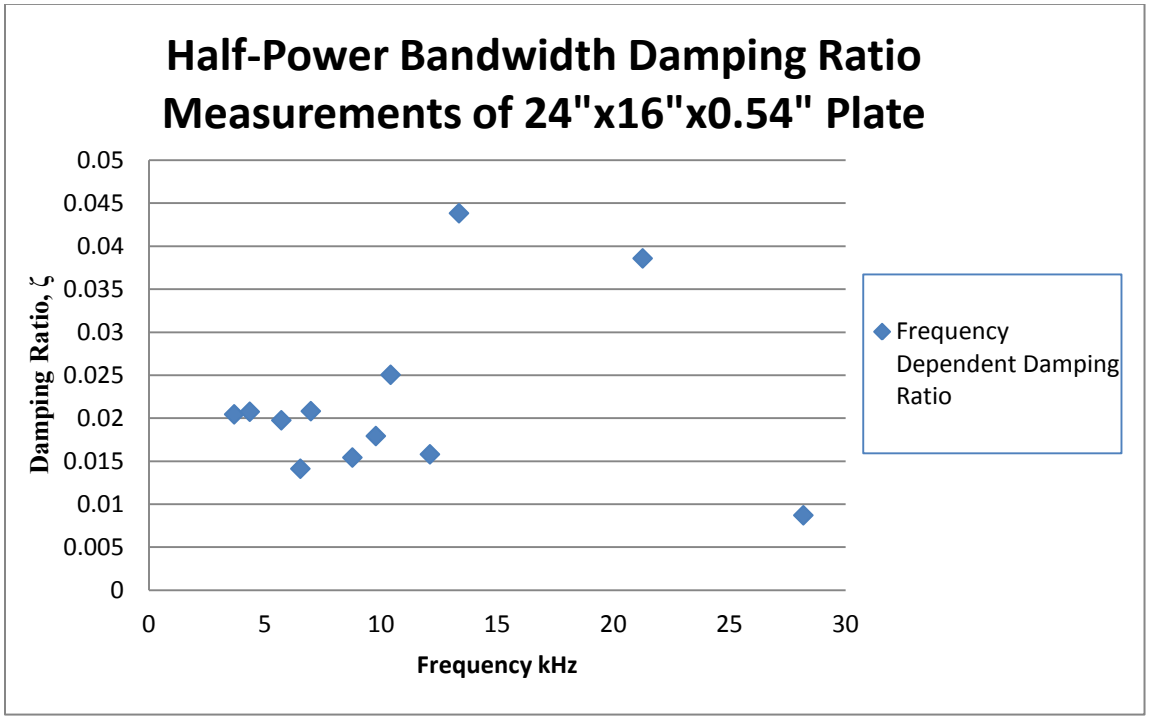

Figure 11. Estimated damping ratios, found using Half-Power Bandwidth Method. Plate clamped within testing structure.

From the values sampled during testing, an averaged value of the material damping ratio was approximated. It was also noted that acceleration response measurements within certain frequency ranges might be questionable due to some peculiarities that were noted during subsequent data processing. The graph below in Figure 12 shows acceleration data for the various fiberglass composite plate samples that were tested throughout the span of this research. The test data plotted in the graph corresponds to six separate tests, performed on multiple plates of various dimensions. The tests performed also utilized various transducer and plate mounting configurations. Looking at Figure 12, one can

note the significantly large acceleration response values measured within the frequency bands of 11kHz - 18kHz as well as 18kHz - 21kHz for all tests with the exception of the "ply-drop response" test, which used a different accelerometer when compared to the other tests.

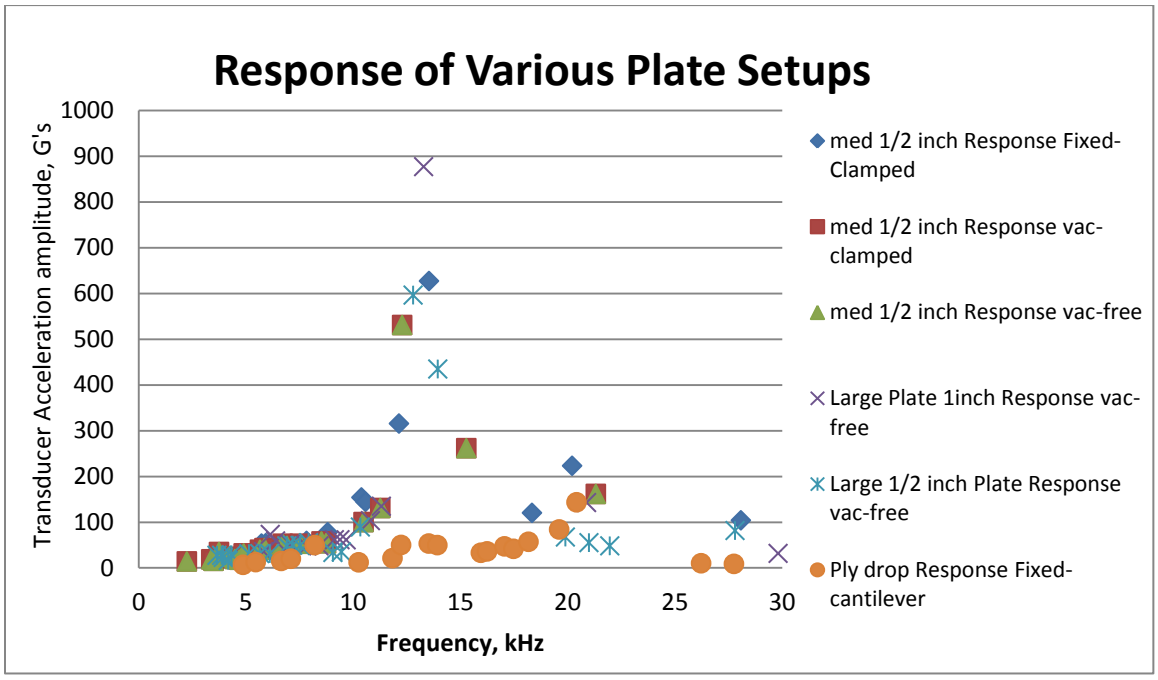

Figure 12. Superimposed results of all tests performed to date. Data represents test using various plate geometries and boundary conditions

Within both of these frequency spectrums extremely large resonant acceleration responses were measured, when compared to all other frequency ranges. Again, these extremely large acceleration values were acquired from measurements taken from multiple plate geometries, with various imposed plate boundary conditions and various transducer mounting apparata. One might question the likelihood of 3 different plates, of varying thicknesses and overall geometries, subjected to multiple forms of restraint and

transducer application conditions, all exhibiting significant resonant responses along distinctly similar frequency bands.

To this point it has been assumed that some common point (possibly the transducer or accelerometer) within the testing set-up experiences resonant response to harmonic excitations within these two frequency bandwidths. The data collected within these regions has subsequently been deemed questionable, and was not utilized in the calculation of averaged viscous damping ratios. Instead, the span of usable data was truncated at 11kHz and averaged damping ratio values were calculated from data within the 0 to 11kHz range. Using this method the averaged viscous damping ratio for the 24”x16”x0.54” plate was calculated to be 0.0244. This damping ratio value will be utilized in the analyses outlined throughout the rest of this document.

Frictional Contact Modeling Assumptions and Estimation of Frictional Properties

In order to model the frictional contact, and the resulting heat generation which occurs along the various flaw sites within the plate, a frictional model had to be assumed and implemented within the FE model code. For the purposes of this research, estimations of vibration induced frictional energy dissipation are approximated using the Coulomb Friction model, a classical quasi-static friction model which only takes velocity-force relationships into consideration. Research has shown however that frictional heat generation relationships typically not only depend on velocity and force, but instead also depend on the rate of change of velocity; research also shows that friction is typically also displacement dependent for interactions between elastic bodies. Such

displacement dependency often leads to hysteretic behavior. An in-depth analysis of this topic is outside the scope of this paper, however, some degree of hysteresis would be expected within the periodic behaviours of flaw frictional slip interactions.

Utilizing the Coulomb model of friction leads to ignoring the effects of relative accelerations between the contacting elements. Frictional contact interactions may be more properly accounted for using other friction models, such as the LuGre friction model, or the Leuven friction model, an integrated friction model proposed by Swevers et al [8]. For the purposes of this analysis however, the Coulomb friction model will be used, as this is the default friction model provided by ANSYS, and also because the frictional constants used in conjunction with this model are readily found within various scientific research articles. Properly utilizing the more elaborate friction models might require that numerous tribological parameters along the delaminations be quantitatively measured which is outside of the scope of this research.

Reliance on the Coulomb friction model for the analyses of this research requires that the analyses be properly configured so that the time discretized periodic contact interactions at the flaws are accurately approximated. Not properly implemented, the Coulomb friction model might not accurately predict frictional contact states for the small relative displacement, high frequency periodic motions occurring along the contacting flaw regions. Depending on the Coulomb friction model to produce a reasonable estimate of frictional heating requires an adequate discretization of the time domain throughout the span of analysis; because the Coulomb model assumes a static relationship of force-velocity across each discretized time increment, a reduction in time increment will allow for the states of frictional contact along the flaws to be more properly represented through

time. Certain hysteretic behaviours of the high frequency periodic contact interactions might not be properly predicted, but the overall accuracy of the model is assumed to be adequate.

Estimation of Frictional Coefficients and Properties

With a friction model chosen, the necessary frictional parameters were approximated after researching various scholarly articles exploring tribological effects associated fiber/glass epoxy composites. Difficulty was encountered in tracking down information directly investigating the frictional properties between epoxy/glass and epoxy/glass interfaces. Some research investigating frictional contact between epoxy/glass composites containing graphite powder or rubber additives and roughened steel surfaces has shown [9] that various additives and their concentrations can have an appreciable effect on the frictional properties, especially at lower relative velocities. The dynamic coefficient of friction of composites doped with a lower concentration of graphite powder (2.5% by weight) was estimated by Kishore [9] to be anywhere from 0.37 to 0.45, while composites doped with rubber powders varied between 0.49 and 0.85. Research investigating the frictional properties within graphite fiber/epoxy composite delaminations, performed by Schön [11], suggests values of dynamic friction coefficients between around 0.2 and 0.54. The values proposed in the latter research is likely more representative of our model, rather than that of the research involving the powder impregnated matrix materials. The results of the studies suggest that the estimations of μ_k may also depend on applied normal force, duration of wear, and relative velocity. The

Coulomb friction model describes the dynamic friction states as either static friction μ_s or dynamic friction μ_k according to the following formula

$$\mu = \begin{cases} \mu_s & if\ \tau \leq \mu_s \sigma_N \\ \mu_k + (\mu_s - \mu_k) e^{-(DC) v_{rel}} & if\ \tau > \mu_s \sigma_N \end{cases} \qquad \text{Equation 16}$$

Where: $\mu_s \sigma_N = \tau_{crit}$

where τ represents the tangential frictional force, F_N represents normal force, and DC is a decay constant which determines that rate at which the friction μ transitions from μ_s to μ_k with respect to relative velocity v_{rel}. As can be seen in the above formula, the state of contact would be expected to transition between sticking μ_s, frictional sliding μ_k, or no contact. The coefficient of friction chosen will dictate the manner with which frictional heat generation occurs, and is also expected to affect total area over which relative sliding or sticking (and thus frictional generation) occurs.

The updated material properties assumed for the models, now including the empirically derived viscous damping ration ζ, and the investigated dynamic coefficient of friction μ_k are listed below in Table 2. With estimations of these system properties made, more accurate FE analyses of the modeled plate may be performed.

Table 2. Extended Material Property Set Employed within FEA Model

Material Property		**Units**
ρ	1876	kg/m^3
ν	0.34	Poisson's Ratio
E_x	19.6	GPa
E_y	19.6	GPa
E_z	8.8	Gpa
G_{xy}	6.4	GPa
G_{yz}	4.1	GPa
G_{xz}	4.1	GPa
ζ	0.0244	Damping Ratio
μ_k	0.37	Coefficient of Kinetic Friction
μ_{static}	0.4	Coefficient of Static Friction

DEFINING THE BOUNDARY CONDITIONS OF THE MODELED PLATE SYSTEM

Implementation of Realistic Boundary Conditions within Finite Element Models to Approximate Physical Clamping Conditions

After empirical damping ratio testing had been performed on the 24”x16”x0.54” plate, boundary conditions similar to those recorded during the testing procedures were implemented into the ANSYS finite element model code. During the half-power bandwidth testing, the areas over which the composite plate was clamped by adjustable vise grips of the test fixture were measured. The two shorter edges of the 24”x16” plate surfaces were clamped with the vices where only a small portion of the plate edges were actually clamped by the gripping pads of the vices. Care was taken in defining and imposing the clamping conditions between the plate and the testing structure in order to facilitate proper modeling of the clamping conditions used in empirical tests.

Measurements taken during testing showed that only 6”x2” areas along the sample’s faces (centered about the edge-length, at either side of the plate) were contacted by the clamps. In order to approximate the boundary conditions imposed during empirical testing, within the FE model, zero-displacement boundary conditions were imposed at nodes occurring along the clamping regions (similar to the conditions used during empirical test procedures). Translations in all three principle coordinate directions were restricted to zero at the nodes occurring at both the top and bottom of the plate at the clamping interfaces. The clamped areas (shown on one side of the plate) are shown in the Figure 13 below.

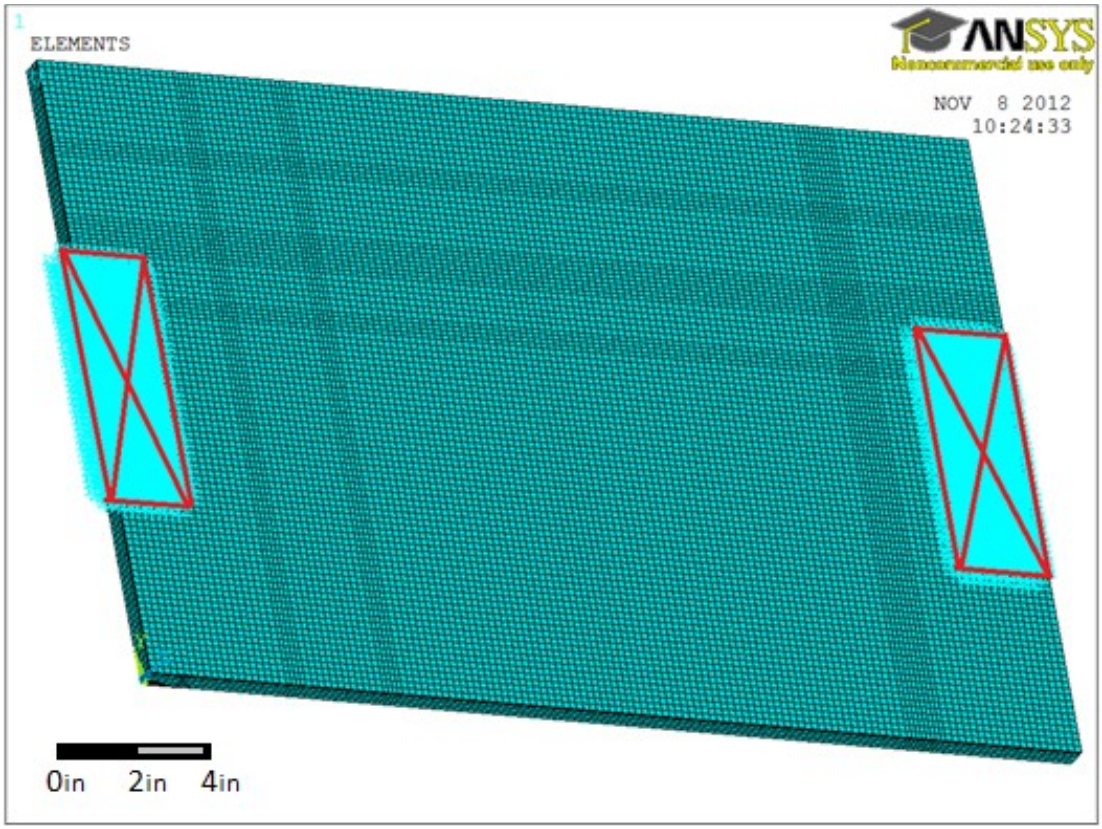

Figure 13. Meshed plate with applied zero-translation boundary conditions (at both surfaces of the plate)

These basic boundary conditions were utilized throughout the majority of testing for the 24”x16”x0.54” plate, and were also implemented within each ANSYS FE analysis of the full plate model.

Implementation of Static Pre-Load Forces

As was briefly mentioned in the section outlining the methods used in implementing the half-power bandwidth method to test for damping ratios, considerable pre-load force was applied to the composite plate, during empirical testing procedures. The pre-load was applied as a static force load which was imparted through the high-

frequency force transducer system. The main purpose of applying a pre-load was to ensure continual contact between the high-frequency transducer system and the plate. Decoupling of the high-frequency transducer system and the plate typically results in periodic impact between the two structures; such impact tends to introduce short-lived transient response phenomena along the impact regions. This periodic hammering effect introduces un-predictable variability within empirical testing, and may greatly skew the results of an analysis aiming to identify the local responses along a flaw region. For the purposes of the empirical tests carried out through this research a static pre-load force of 200lbs was applied to the plate through the high-frequency transducer system. This pre-load, in conjunction with a compliant buffer material being introduced between the frequency transducer and the plate, was fairly effective at mitigating decoupling within the transducer/plate system, though some instances of decoupling were still noted. The location at which the both the pre-load and harmonic excitation forces were applied is show in Figure 14 below.

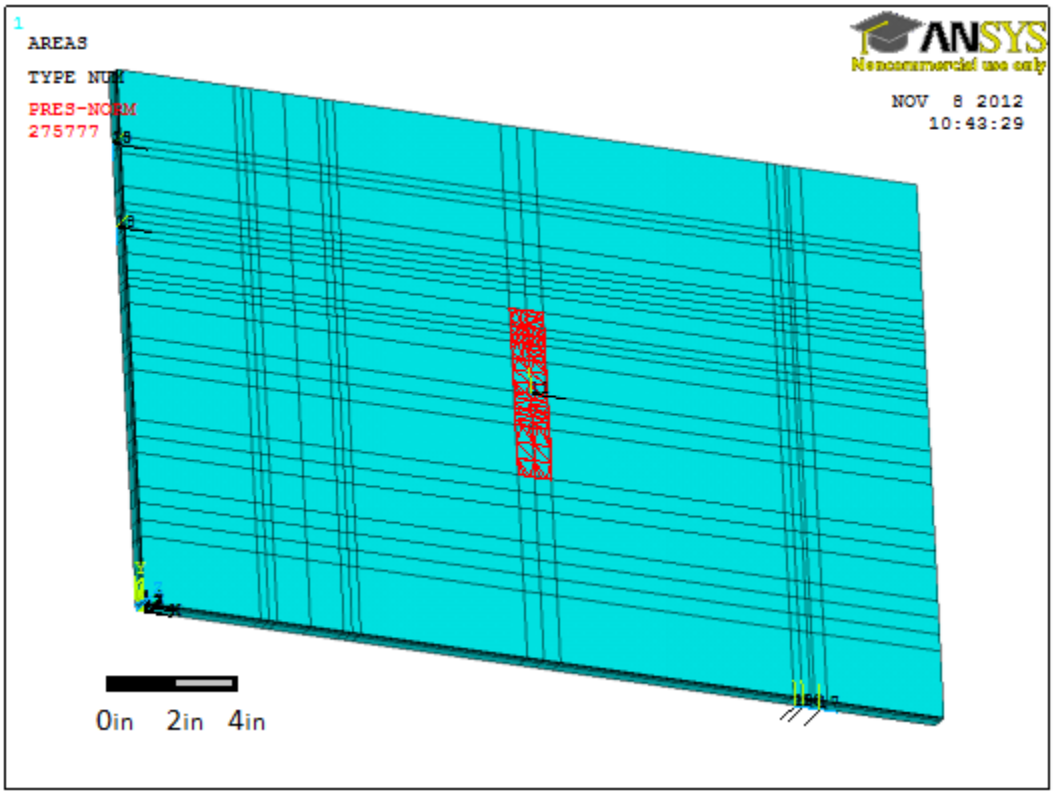

Figure 14. Solid body model of the plate, with the transducer pad interface displayed in red.

The loads were assumed to occur as uniform distributed loads (denoted by the red area in the figure above), acting over the entire contact surface between the aluminum pad (and compliant buffer material) of the transducer and the top of the plate. As has been stated, region over which the load is applied is assumed to be perfectly coupled to the transducer pad, which is an over-simplification of the system.

The application of the static pre-load unto the plate does play some effect on the plate's vibrational response. In the case of the system analyzed in this research, the static pre-loading of the structure may be accurately approximated within a linear structural analysis; application of the 200lb pre-load however, does deform the structure enough to slightly affect the modal and harmonic responses excited in the plate model during modal

and harmonic analyses. Furthermore, deformation caused by the applied pre-load, causes the previously co-planar flaw surfaces of each delamination to separate; this separation occurs over the majority of each flaw surface. This behaviour was noted in previous research completed for this particular project, though involving ply-drop samples with through thickness delaminations [12,13]. The induced separation is so significant in fact, that typically only a small portion of the flaw areas experience any contact at all. Even during harmonic excitation of the plate over the majority of the 600-30,000Hz frequency band the majority of the Contact/Target elements within the model experience no contact (and in turn experience no frictional contact). A simplified schematic, depicting a cross-sectional area view of the pre-stressed plate, including an embedded delamination is shown in Figure 15 below:

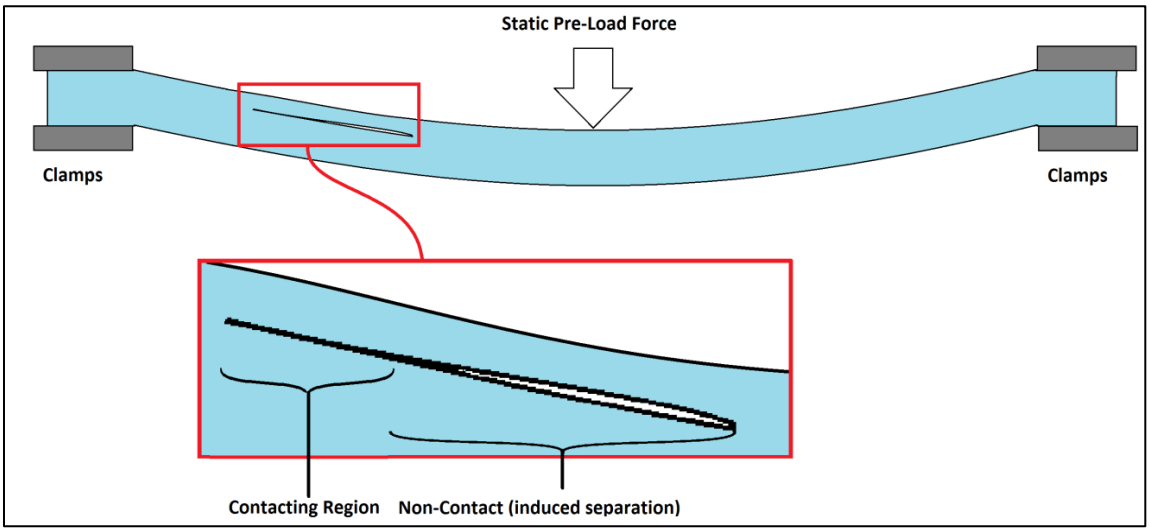

Figure 15. Gap is induced along fully-embedded delaminations due to static pre-loading of the plate.

An example of the effect that application of static pre-loading has on the plate is illustrated in the figure above; while originally coplanar, the majority of flaw region areas

become separated under the effects of pre-loading. This separation of flaw surfaces tends to reduce contact across the majority of the flaw areas for most harmonic excitation frequencies; the portions of the flaws closest to the high frequency transducer are the areas which regularly experience contact.

PREDICTING MODAL RESPONSE OF THE PLATE VIA ANSYS MODAL ANALYSES

In an attempt to characterize the vibrational response of the plate, ANSYS's modal analysis solvers were used to calculate the modal frequencies of the FE model. Mode shape (eigenvector) information was also recorded for each modal frequency, which was then later used to validate the FEA results with empirical testing results. The modal analysis of the plate model provides a basis on which harmonic response analyses, and consecutively transient sub-model analyses, were carried out. An explanation as to how modal analyses were implemented is outlined next.

ANSYS Produced Mode Shape Data

Modal frequency analyses were performed using the ANSYS finite element models to identify the modal frequencies of the 24"x16"x 0.54" plate. The modal analysis was performed over a frequency bandwidth of 600Hz-30kHz in an attempt to identify all modes within the desired testing bandwidth. During the analysis, both eigenvalue (modal frequency) and eigenvector (mode shape data) data were recorded for each calculated mode. The material properties used throughout the modal analysis were similar to those listed in Table 2.

Because Modal and Harmonic analyses within ANSYS are static analyses types, which can't accurately predict the effects of the dynamic (though steady state harmonic) contact surface interactions which would be expected to occur within the harmonically excited plate, these analysis types may offer only a general approximation steady-state

(harmonic) response of the plate. Under certain assumptions such analyses may give reasonably accurate approximations of modal responses; these analyses were carried out based on the assumption that the nine flaws are all of relatively small size, when compared to the overall size of the plate. The assumption of relatively small flaw sizes assumes that their influence on the global modal and harmonic responses of the plate will be minimal.

In order to account for damping within the modal analyses, ANSYS's *QR damped solver* algorithms were utilized. This solver allows for estimation of eigenvalues in models with unsymmetrical global stiffness matrices. Elements such as contact elements under the influence of friction (which are present in this model) generate nonsymmetrical element stiffness matrices. The solver is only applicable to models where only a small portion of elements contribute nonsymmetrical element stiffness matrices. As was discussed in the following section, the models analyzed throughout this research include only a relatively small number of contacting elements, thus implementation of the QR damped solver in estimating modal frequencies for the model is assumed to be appropriate[14].

After Modal analyses were performed over the designated frequency bandwidth, the mode shapes excited within the modeled plate were analyzed via ANSYS post-processing. The relative mode shape displacements along the top surface of the 24"x16"x0.54" plate were also recorded in matrix form. ANSYS APDL code was used to gather the relative z-displacement (normal to the larger plate surfaces) data which included both harmonic displacement magnitude, and relative phase angles for each node along the entire top surface of the plate model, for a total of 14,200 nodes. The x- and y-

coordinate values of each sampled node were also saved. This process carried out to retrieve mode-shape information along the top plate surface for every modal frequency (eigenvalue) solved for within the defined frequency bandwidth.

Since the FE element mesh was created as a rectangular "mapped" mesh, displaying the mode-shape information along the top surface in matrix form was easily facilitated. The mode shape data matrices were written to .txt file format using APDL post-processing code. The purpose for saving the mode-shape data in matrix form within .txt file format was to allow for the data to be easily read and accessed through various software packages. With mode-shape information sampled and saved across the entire top surface of the plate, the matrices can be retrieved and plotted through programs such as MATLAB® or Microsoft Excel®, and the mode shapes along the entire top surface (at each node) can be visualized as shown in Figure 16 below. The mode-shape information represents only the relative mode-shape displacement magnitudes at each point across the surface, the relative phase angle information corresponding to the mode-shape data however, is not represented in the plot.

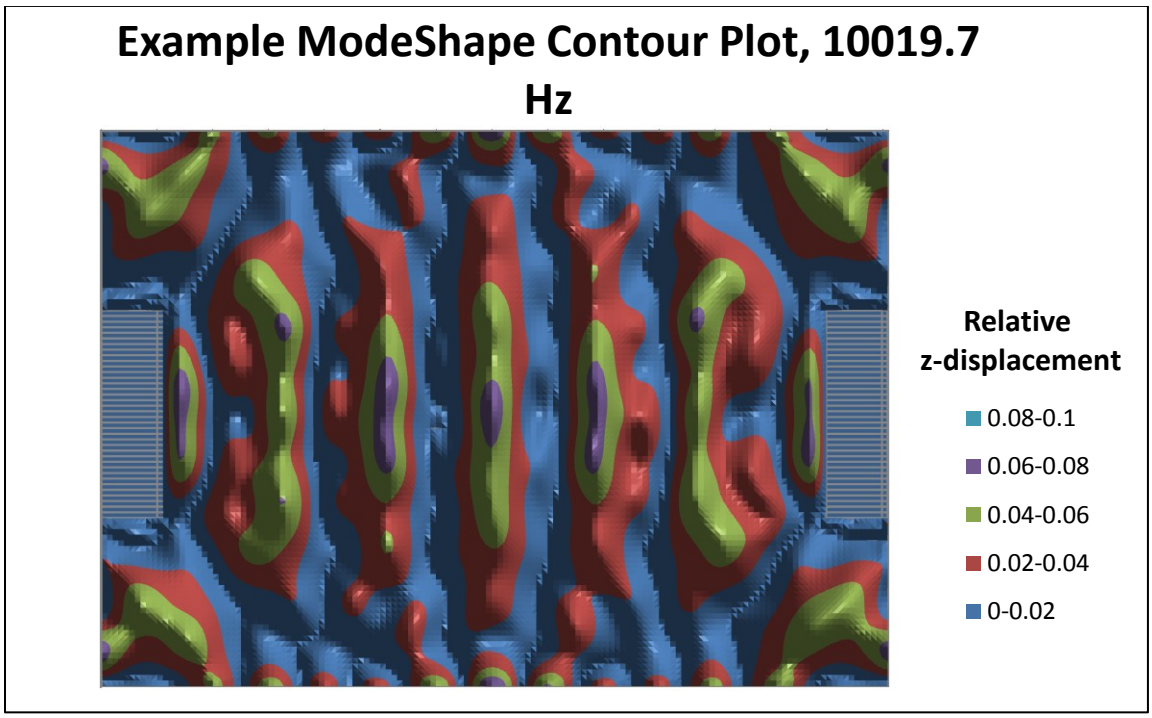

Figure 16. Example of Surface Contour plot displaying relative z-displacements along the top surface of the 24”x16”x0.54” plate. Note the zero displacement values which occur at the supporting clamps.

As seen in the plot legend above, the range of z-displacement magnitude spans from zero to one. ANYS allows for modal eigenvector results to either be normalized to the model’s mass matrix or to unity; for the purposes of this research, the eigenvectors calculated in these analyses were normalized to unity.

Attempt to Verify Mode Shapes Predictions Through Empirical Testing

After mode shape data was collected from ANSYS, empirical tests were performed in an attempt to verify whether predicted mode shapes were representative of resonant harmonic responses of the manufactured plate, during empirical testing. Two separate testing methods were employed in an effort to sample and record mode-shape

information for the manufactured plate. The first method involved dispersing colored sand over the top (horizontal) surface of the plate, with the goal of displacing the sand under the effects of the plate's harmonic response. The second method involved direct measurement of the harmonic acceleration response at various points on the plate via accelerometer instrumentation measurements.

Currently the most extensively employed testing method (with regards to the testing of this particular plate throughout our research) is the sand method, due to the relatively short testing time required. Accurately and reliably testing for mode shape data using the accelerometer method involves placing accelerometers at various points along the plate in an attempt to identify the relative accelerations at various points of the mode shapes excited within the plate. In order to acquire enough data resolution to confidently verify two dimensional mode shape pattern information (measuring only the scalar value of acceleration magnitude) either an approach implementing a large quantity of accelerometers strategically placed at various points along the plate surface, or an approach using fewer accelerometers which must be applied, detached and then reapplied, repeatedly for each frequency test, could be used. Both of these approaches however suffer from the drawback of the system's mass (and mass distribution) being affected by the instrumentation. Each accelerometer also requires instrumentation wiring connections, which may adversely affect the response and equivalent structural damping of the system. Perhaps with only one or few accelerometers being applied, the effects on the modal frequency and harmonic responses would be minimal; however application of numerous accelerometers would surely add some ambiguity to the results. Using this method, accelerometers could either be place along a linear path along the surface of the

plate to track mode-shapes in a domain of single dimension. Likewise, a small grid of accelerometer points could be used to track acceleration data across two dimensional sections. Either way, the resolution at which accelerometers may be placed along a sampling region is prohibitive both in spacing requirements and available accelerometer quantities. In the case that such a method is utilized, selectively placing only a few accelerometers (so as not to disturb the structures natural frequencies) would require strategic placing and re-placing of accelerometers for a single frequency test, which tends to make this method onerously tedious and time consuming. One benefit that is realized using accelerometers is in the sensitivity and quality of measurement. The quality of the measurement is improved in the sense that both acceleration and relative phase angles may be quantitatively ascertained, and with great precision; such information is not available using the much faster, area sampling, sand method.

As was mentioned, the sand method was nearly exclusively used during this research. Utilizing the sand test involves placing sand atop the horizontally level plate surface, and distributing it fairly evenly across the entire surface. When the harmonic transducer is used to excite the plate, and if the vibration response is great enough, oscillation at various points of the plate will tend to force sand grains away from mode shape anti-nodes and into the lower energy nodal regions, where the sand will then tend to settle. During such tests accelerometers were used in an attempt to identify resonant frequencies. Multiple accelerometers (at least two) were used throughout each trial of testing to mitigate the chances accidently “missing” a resonant frequency response due to a single accelerometer being inadvertently positioned along a modal node path or point.

The signals produced by the accelerometer instrumentation were processed through a digital oscilloscope. The harmonic frequency being applied to the plate at the transducer site was varied over the testing bandwidth of 5000Hz to 24,000Hz, the span of this bandwidth being chosen in account of past testing experiences with regards to the sensitivities of the frequency transducer system. Once a large structural response was identified at the accelerometer points, that frequency was dwelled upon for some time to determine if the overall plate response was great enough to cause the (somewhat) uniformly distributed sand to flow into the mode shape patterns. During these testing procedures it was quickly realized that the plate's resonant responses to the harmonic transducer excitations typically weren't great enough to cause the sand to bounce and flow away from the mode shape nodal locations. Only a few discernible sand patterns were adequately defined so that a positive identification of mode shape pattern could be ascertained. Another difficulty was realized during testing in the form of sand patterns well defined over the entirety of the plate surface, even for the most prominent resonant responses. This irregularity is believed to be attributed to non-ideal clamping conditions, but should be more thoroughly investigated during future testing procedures.

Running the test over a large frequency bandwidth, spanning from 5,000Hz to 24,000Hz, numerous mode shape patterns were positively identifiable. The results of these sand patterns were then correlated with ANSYS FEA predicted mode-shape patters. The more well-defined sand pattern mode-shape frequencies that were identified are displayed here in Table 3.

Table 3. Mode Shape Correlation Data

Harmonic Test Excitation Frequency, Hz	ANSYS Predicted Modal Frequency, Hz	Percent Difference
6485	6863	5.66%
11700	12648	7.79%
15250	15638	2.51%
20200	20785	2.85%

Visuals depicting the mode-shape sand patterns that were positively identified are displayed in conjunction with the ANSYS predicted mode-shapes in Figure 17 through Figure 24 below. In total, four complementary pairs of figures are shown, each pair corresponding to mode-shapes representing the frequencies outlined in each row of the table above.

Testing Frequency=6,485Hz **Predicted Modal Frequency=6,863Hz**

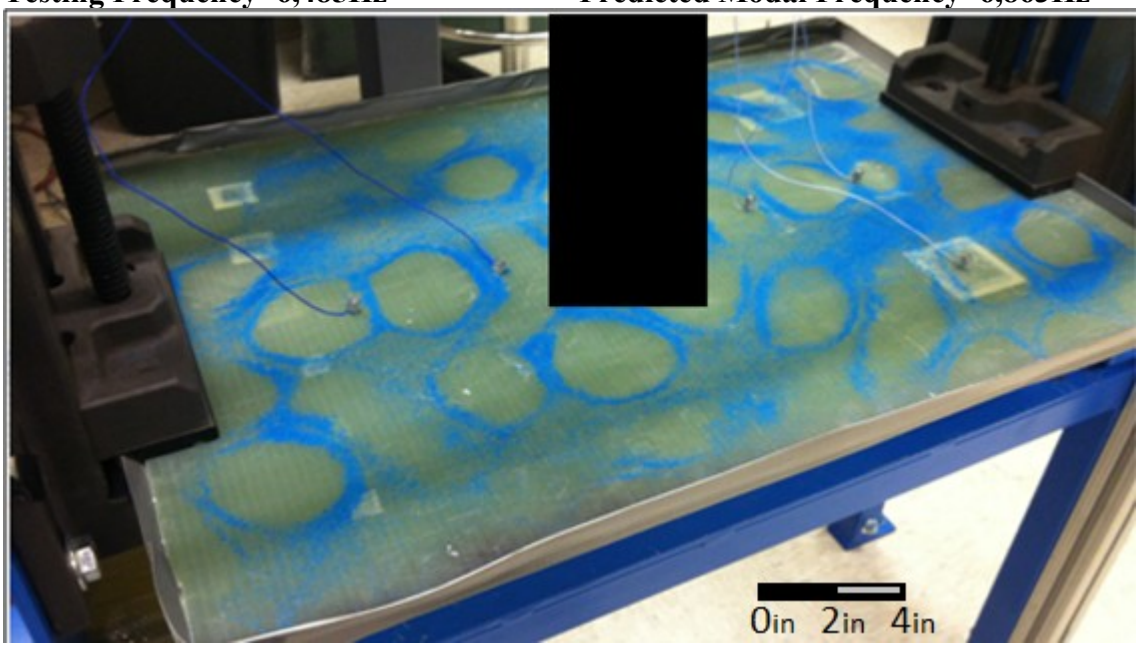

Figure 17. Mode-shape sand pattern at 6,485Hz.

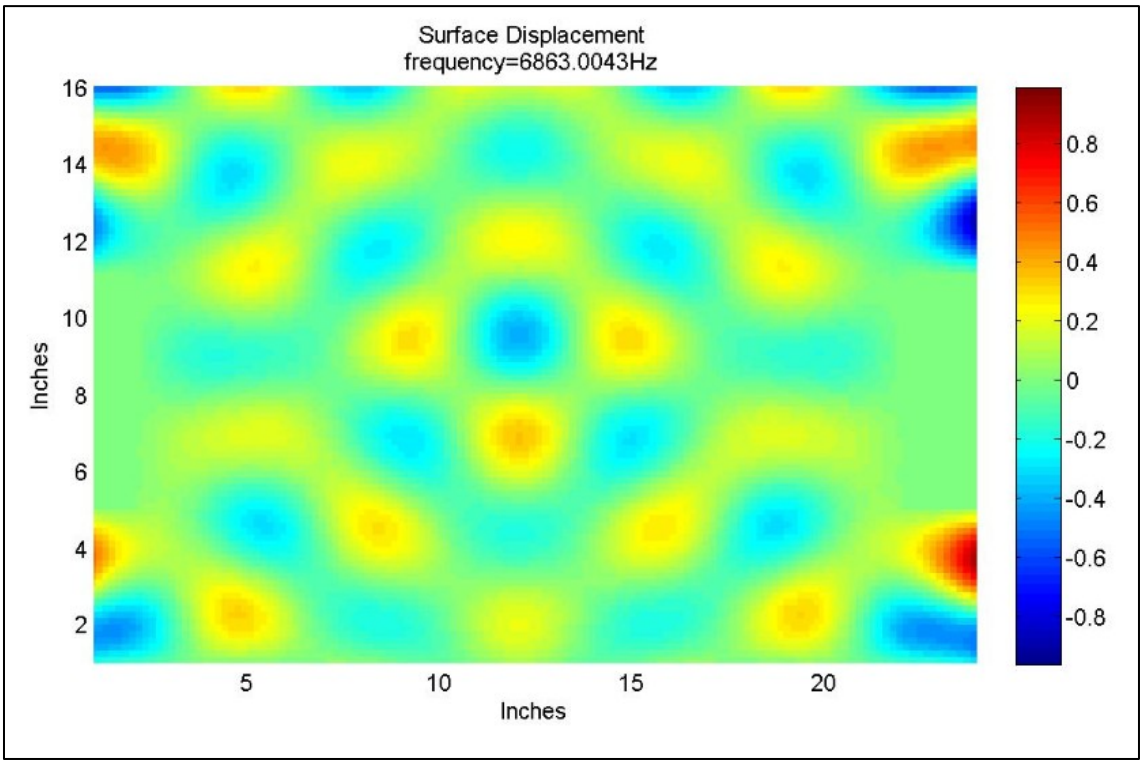

Figure 18. ANSYS predicted mode-shape at 6,863Hz.

Testing Frequency=11,700Hz **Predicted Modal Frequency=12,648Hz**

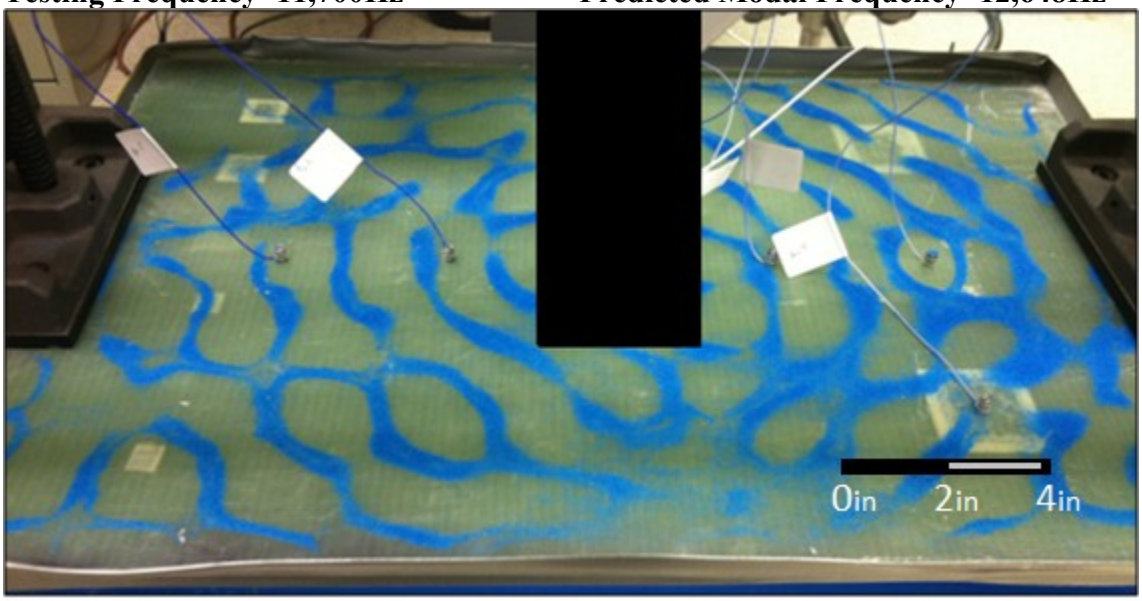

Figure 19. Mode-shape sand pattern at 11700Hz.

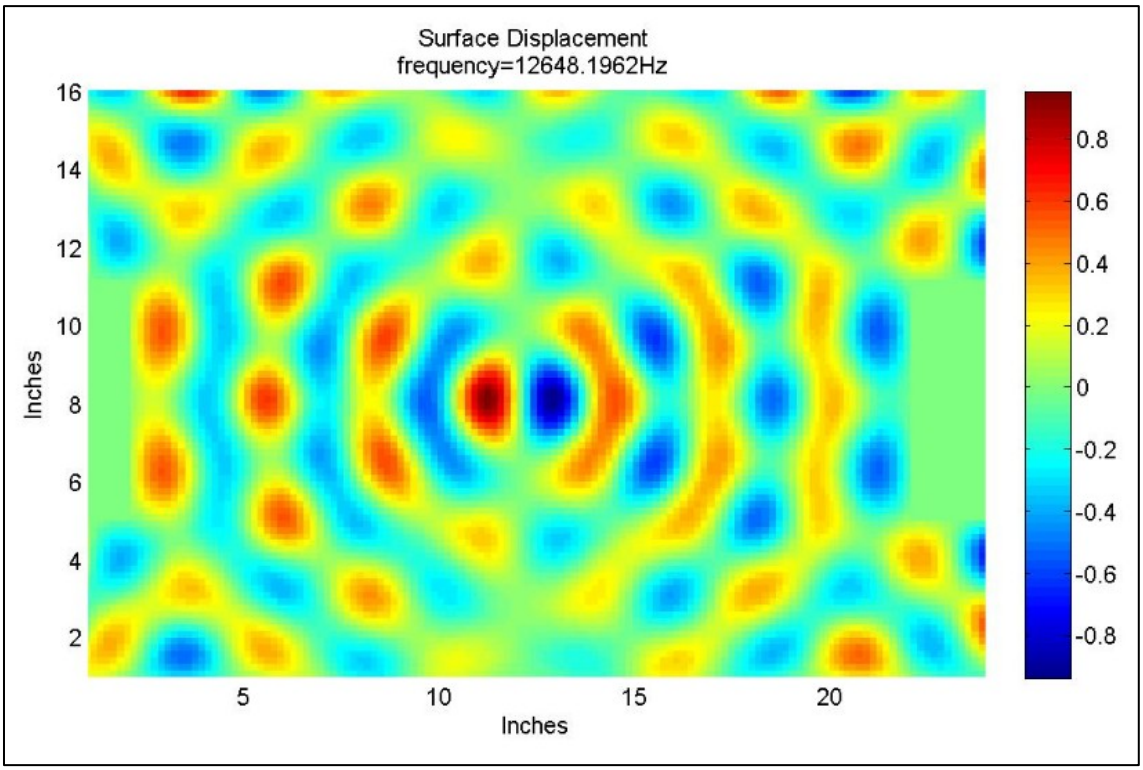

Figure 20. ANSYS predicted mode-shape at 12,648Hz.

Testing Frequency=15,250Hz **Predicted Modal Frequency=15,638Hz**

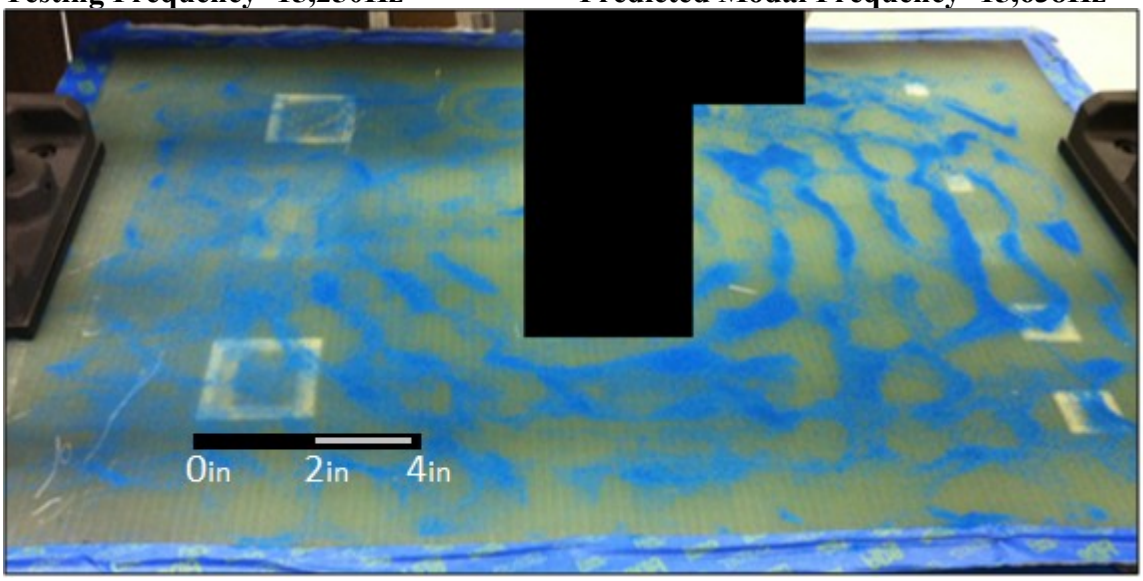

Figure 21. Mode-shape sand pattern at 15,250Hz.

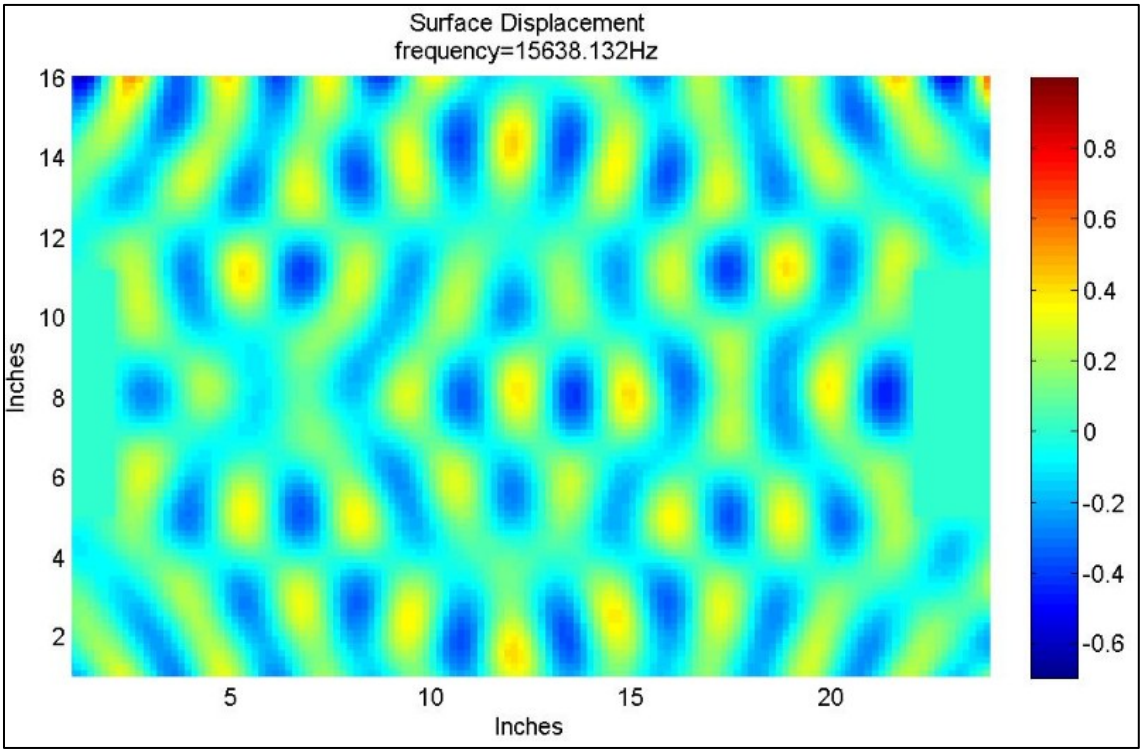

Figure 22. ANSYS predicted mode-shape at 15,638Hz.

Testing Frequency=20,200 Predicted Modal Frequency=20,785Hz

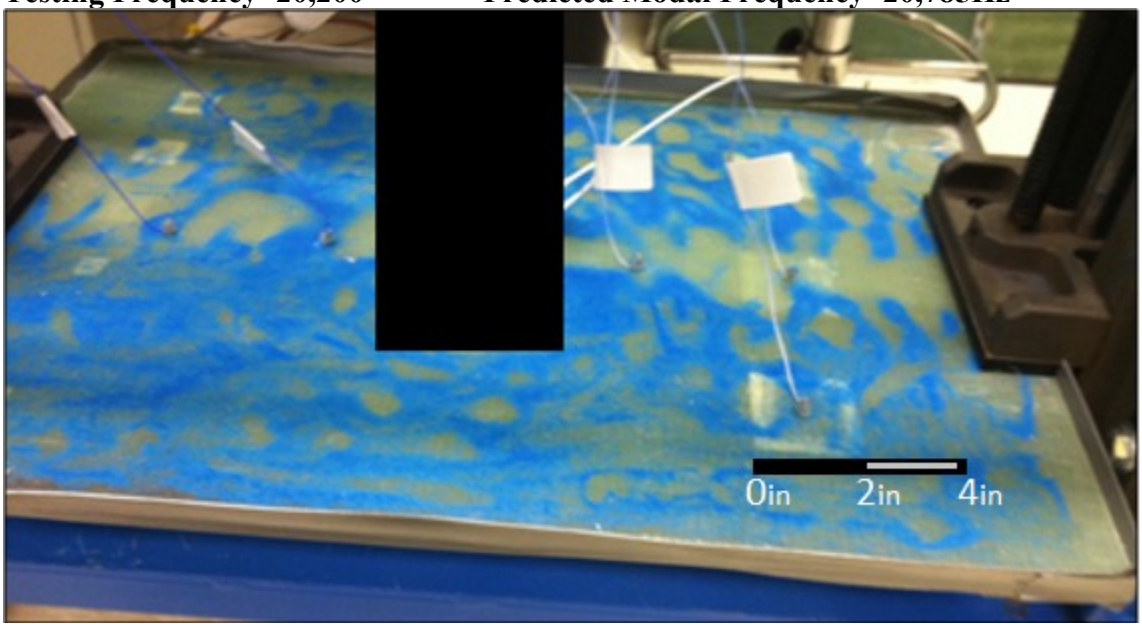

Figure 23. Mode-shape sand pattern at 20,200Hz.

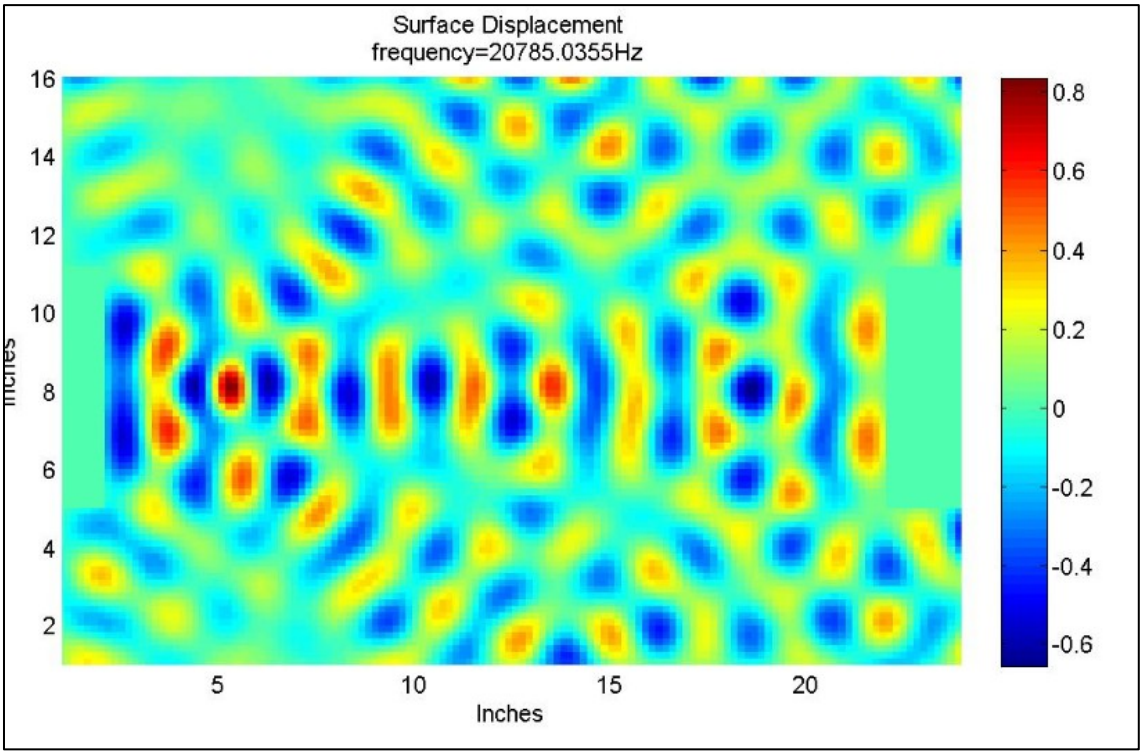

Figure 24. ANSYS predicted mode-shape at 20,785Hz.

It was quickly noted that the lower frequency mode-shapes were much easier to identify than higher frequency modes, due in part to tendency of pattern complexity increasing with frequency.

An unanticipated result was experienced during sand testing, in that mode-shape patterns directly near the vicinity of the rectangular, aluminum transducer pad tended to exhibit unexpected and inconsistent patterns (with regard to the mode-shape patterns ANSYS had predicted at those frequencies). It is also important to note (and is likely corollary to the previous statement) that during testing it was also noted that de-coupling between the high-frequency transducer fixture and the plate often occurred. During empirical tests, this de-coupling phenomenon is often times readily identified through auditory cues, but is also nearly always identifiable within instrumentation signal data, sampled at the transducer site. An example of transducer/plate de-coupling, captured within the oscilloscope data, is displayed in Figure 25 below.

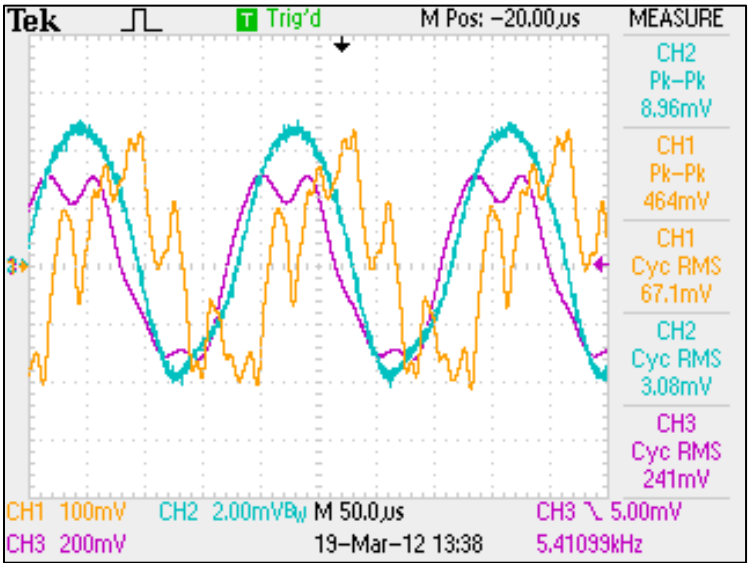

Figure 25. Oscilloscope readout of accelerometer and load-cell signals displaying de-coupling behaviour (YELLOW=Load cell reading, MAGENTA=Accelerometer at transducer, CYAN= Accelerometer at flaw site location)

The instrumentation signals in the figure above are exemplary of decoupling behavior within the transducer/plate system. The sensitivity factor of each sensor has not been applied to the signal data in order to convert to the proper engineering units, but the purpose of the example is still served. Two of the three signals (yellow and magenta) were sampled in the proximity of the frequency transducer application site. The yellow signal, representing the dynamic loading force definitely doesn't represent simple harmonic behaviour, but is in fact periodic. The acceleration signal (Magenta) also offers cues that decoupling is occurring, albeit to a lesser extent. From the oscilloscope readout, one can also note the acceleration signals periodicity.

The eccentric waveforms are believed to be the result of decoupling between the plate and transducer, which causes hammering-typed impacts between various points of the transducer pad and the plate. This impacting behaviour is expected to produce some form of mode-shape super-position. This complex impact interaction had further complicated the process of achieving positive mode-shape sand pattern identifications. Proper selection of the shape of the contact pad (between the transducer and the plate) would almost certainly help to mitigate some of these negative effects during future testing. These predictions of modal frequencies and mode-shape data were performed as a preliminary step to performing subsequent analyses.

HARMONIC RESPONSE OF THE MODELED PLATE

Using ANSYS to Analyze the Harmonic Responses of the Modeled Plate

The harmonic responses of the 24”x16”x 0.54 “plate with boundary conditions and loading similar to those implemented during the damping ratio testing procedures (half-power bandwidth method) were estimated via ANSYS harmonic response analyses. Harmonic response analysis is a technique used to determine the steady-state response of a linear structure to loads that vary sinusoidally (harmonically) with time. The technique calculates the steady-state forced vibrations of the structure, while transient responses (which would be expected to occur at the beginning of excitation, or possibly periodically due to flaw surface chatter) are not accounted for. Assumption of steady-state response presumes that the plate has remained under the influence of the harmonic loading long enough for transient response phenomena to have damped away completely. The premise is to calculate the structure's response at several frequencies and obtain a graph of some response quantity (usually displacement) versus frequency. "Peak" or “resonant” responses at select points along the model can then be identified. The results of these analyses are often used to predict and mitigate resonant responses at operating frequencies, and are often used to reduce fatigue and unwanted interference within structural systems. For the purposes of this research, the results will ultimately be utilized in defining cut-boundary conditions which will be implemented within transient analysis sub-modeling procedures, which will later be discussed in more detail.

Another basic assumption of these analyses, which is important to note, is that any sinusoidal harmonic loads applied to the structure at a particular frequency sub-step, act at the same frequency. That is, multiple loads of varying magnitude, phase angle and direction can be applied to the structure at various points of the model, but all loads applied to the model are assumed to act at a single frequency. For the purposes of this research, only a single monofrequency excitation is applied to the model during each harmonic analysis sub-step.

It is important to note that during empirical testing procedures, application of harmonic loads through the high-frequency force transducer resulted in loads of varying force magnitude being applied with regards to frequency. Application of loads within the FEA models however, assume that a harmonic loading force of constant amplitude is applied regardless of applied frequency. This constant, frequency independent loading value was used in lieu of the lack of empirical frequency dependent loading histories, which could possibly be sampled during an empirical frequency sweep analysis. At the time that these predictive FE analyses were performed, no such empirical testing or data acquisition had been performed on the representative manufactured plate.

The harmonic excitation load applied to the center of the model by the high-frequency load transducer was defined as being 111.2N (about 25 $lb_{f.}$). During empirical testing, a static pre-load of 888.96N (200lb_f) was applied at the center of the plate through the frequency force transducer system. This value was also implemented as a static pre-load value for the ANSYS FE harmonic analysis by performing a linear pre-stressed harmonic analysis. The effects due to pre-stressing, such as alteration of geometries, were accounted for in the harmonic analysis by first completing a static

structural analysis on the modeled plate, and then by passing that information along to a full harmonic analysis.

A preliminary harmonic analysis was carried out over a frequency bandwidth from 800Hz to 30,000Hz in increments of 50Hz in order to investigate response at various points of interest along the plate models. During this analysis, nodal displacement results were sampled at the point of transducer application (accelerometer location), as well as at the center points of each of the nine flaws (along the top surface of the plate). Displacement results in the z-direction (normal to the larger plate surface) for the accelerometer and the center larger flaw (flaw #2) are plotted in Figure 26through Figure 29. The red and green data curves represent the harmonic displacement response at the transducer accelerometer point and at the mid-point of flaw #2, respectively.

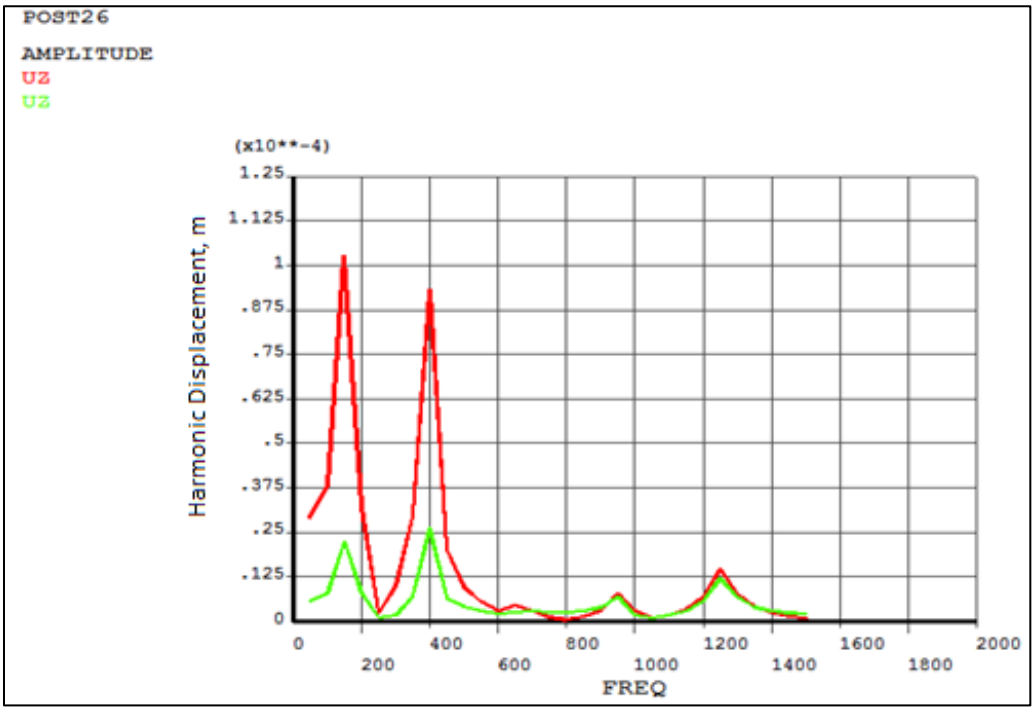

Figure 26. Harmonic data subset 1 of 4, Damping ratio = 0.0244, Damping test boundary conditions

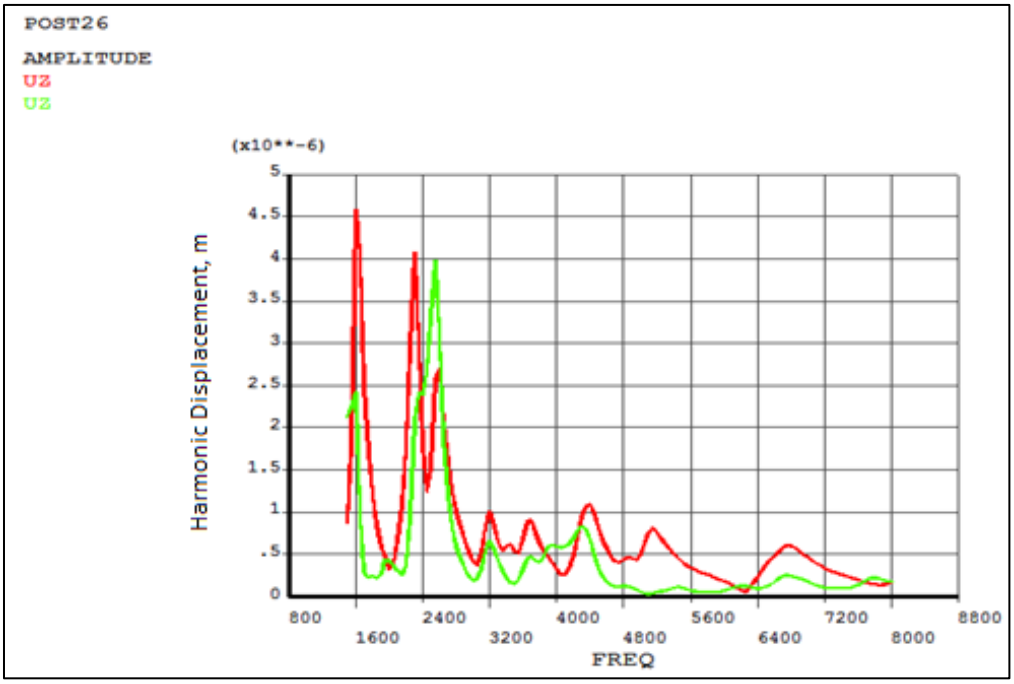

Figure 27. Harmonic data subset 2 of 4, Damping ratio = 0.0244, Damping test boundary conditions

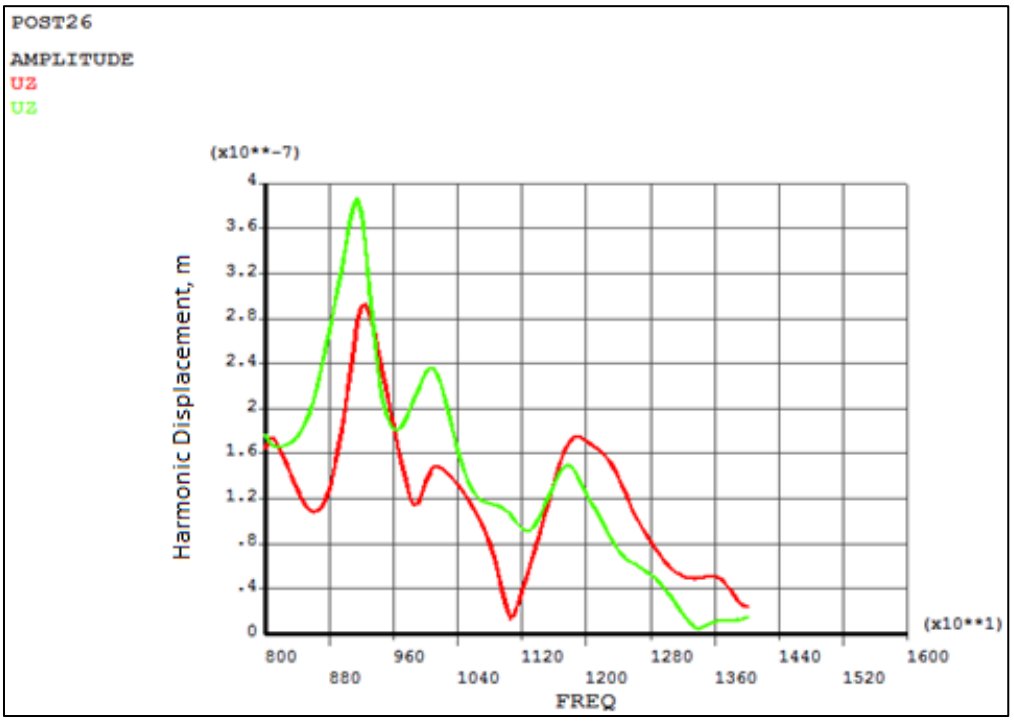

Figure 28. Harmonic data subset 3 of 4, Damping ratio = 0.0244, Damping test boundary conditions

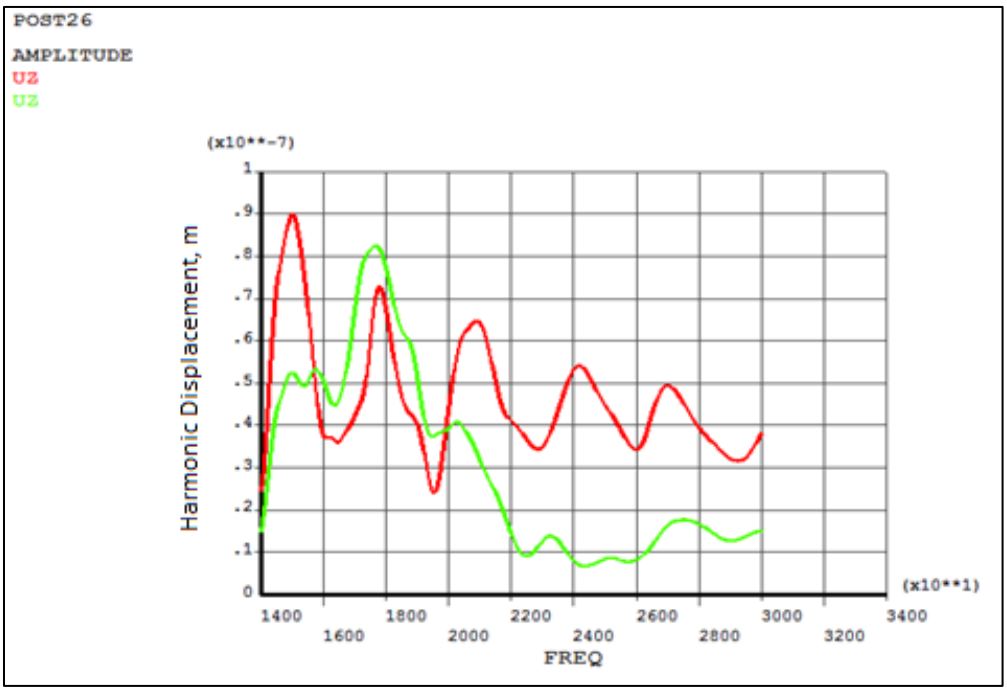

Figure 29. Harmonic data subset 4 of 4, Damping ratio = 0.0244, Damping test boundary conditions

Results of this form are analogous to the type of data that is likely to be sampled during the majority of field testing using accelerometer sampling; short of using a scanning laser vibrometer system, acceleration responses will likely only be sampled at relatively few locations.

Analyzing the harmonic responses sampled at the two points in the figures above, it is immediately identifiable that the response at the delamination center is greater than the response of the transducer accelerometer point at some frequencies, as might be expected. This phenomena lends credence to the idea that maximum heat generation along a delamination surface may not necessarily occur at a resonant peak (as measured and identified at the applied transducer or accelerometer points), but may instead occur at some frequency value which is perhaps offset from resonant peaks. In fact, if resonant

frequencies can be positively identified, the likelihood of vibrothermographic detection of unidentified flaws, might possibly be increased if the excitation frequency is varied around such resonant points, as opposed to dwelling only at the resonant peak frequency. Introduction of high amplitude, off-resonant travelling waves could possibly increase the chances of thermographic flaw detection. In the event that system resonance is positively identified, it is likely that not all flaw points will correspondingly occur at modal anti-node locations, thus, at resonance, imposed boundary conditions and transducer placement are critical.

The Harmonic displacement response of the plate under a harmonic load of 25lbs at 17,900 Hz is shown below in Figure 30.

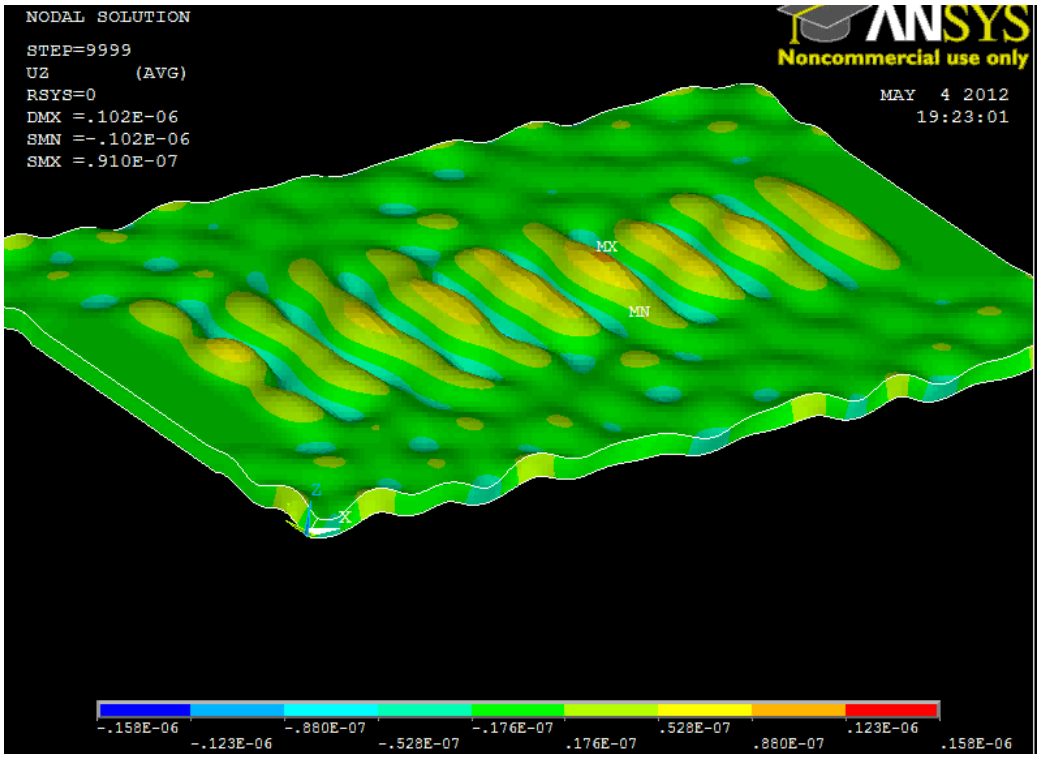

Figure 30. Harmonic Response of pre-stressed plate under 25lb load at 17,900Hz. Using a harmonic analysis allows nodal harmonic displacements to be solved for any node within the model.

Relying on Harmonic response data, or any finite element analysis data for that matter, to give adequate information and foresight into any physical system's response, requires that certain aspects of that system (such as boundary conditions) be known a priori, and also that they be well defined. This information typically is not well defined for any particular structure, especially outside of controlled laboratory settings. Furthermore, the interactions due to imposed boundary conditions within a physical structure are difficult to accurately model. Using finite element analyses in an attempt to properly quantify the response of a physical system, while the system's boundary conditions are not well known, may well prove to be unreliable.

UTILIZING NODAL HARMONIC RESPONSES TO DERIVE FRICTIONAL HEAT GENERATION VIA CUT-BOUNDARY SUB-MODELING PROCEDURES

Creation of Sub-Models for use in Transient Structural Sub-Model Analyses

In the previous section, harmonic analyses were used to approximate the steady-state harmonic vibrational responses at each point (node) within the FE modeled plate. Using this information, transient cut-boundary sub-model analyses were carried out upon individual sub-models, each including a single delamination flaw. During the harmonic analyses, nodal displacement information (translations in all three Cartesian coordinates, along with phase angles) was saved for every node occurring along defined cut-boundary regions. ANSYS APDL code was utilized to pass this information into transient structural analyses, to be implemented as boundary conditions along each delamination sub-model cut-boundary. The steady state harmonic displacement boundary conditions,, $\tilde{U}_i$, imposed at each boundary node are represented by the following equation:

$$\tilde{U}_i^k(t) = A_i^k cos(2\pi f t - \phi_i^k) \qquad \text{Equation 17}$$

Where: *A= harmonic displacement amplitude, meters*

ϕ= phase angle (with respect to applied harmonic force) , radians

f= harmonic excitation frequency, Hz

and where: *k= node number*

i= x,y,z coordinate directions

These time dependent, harmonic, translational displacements are imparted to each and every defined cut-boundary node within the respective transient structural sub-modeling

analysis, in effect forcing sub-model boundary conditions to mimic the responses that would be seen at those nodes under a steady-state harmonic excitation of the plate. An example of a meshed delamination sub-model is shown in Figure 31 below.

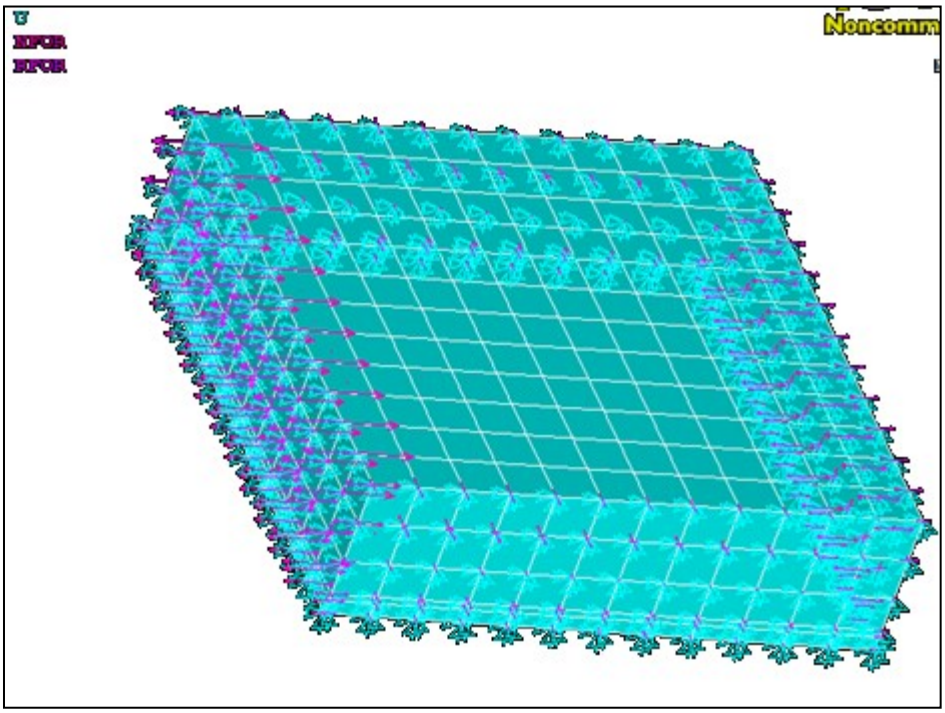

Figure 31. Single delamination sub-model. Time varying Harmonic displacements are imposed along the four outer surfaces (cut-boundary) of the sub-model.

Imposed nodal displacement conditions are displayed as vectors (denoted by purple arrows) originating at each cut-boundary node. This illustration shows only vectors in the horizontal (x-y coordinate) plane directions, though displacement conditions are enforced in all three principle coordinate directions.

The primary goal of implementing this particular method is to reduce the computational time required to analyze flaw surface contact interactions within the model. Rather than calculating the dynamic responses at every point within the plate,

here only the responses at and immediately surrounding the delamination are considered. Reliance on this method is predicated by the assumption that the flaws are of relatively small size when compared the dimensions of the total plate system, and that the periodic responses elicited at and around those flaw do not significantly affect the overall response of the system . The validity of this assumption has yet to be adequately tested, and is left for future work. Validations of this assumption could be explored both empirically and through FE simulation. Empirical harmonic displacement results between plates with singular embedded flaws of various size could be tested against a control sample, which includes no delamination flaws, and the response characteristics of the plate systems could be compared. Furthermore, finite element analyses comparing the results of harmonic response analyses to those of transient structural analyses incorporating models of singular, properly refined, could also be analyzed and compared, in order to determine the effects of delaminations on overall system response. The computational run-times of such methods, however, would likely be un-manageable.

Performing such full-model transient analyses over a broad frequency range to produce an adequately sized set of data would quickly become infeasible, simply due to the significant computational cost of each individual frequency iteration. Running a full transient structural finite element analysis for a properly meshed model, with multiple de-laminations, would require an unacceptable amount of time using ANSYS's implicit solvers, even for a single iteration.

On the other hand, the methods used in this research, allow for a sufficiently large amount of data to be produced. With the procedures currently being employed, frictional heat generation response data for all nine delaminations over frequency sweep

analyses carried out at every 200Hz within a 800-30,000Hz bandwidth can be solved for within around 28 days. This computational run-time is quite long, but is likely an order of magnitude shorter than the time that would be required for a frequency sweep transient analysis to be performed for a properly meshed full-sized plate model. The sub-modeling routine used here is the core method which allows for such a comprehensive frequency sweep analysis to be successfully completed within a reasonable amount of time

One of the other very important aspects of the methods outlined here is that they allow for extreme mesh refinements along each of the delamination surfaces, which otherwise wouldn't be easily facilitated (for full sized plate models) within a full-scale model, given the computational and ANSYS licensing capabilities available for this research. The Meshes applied to the delamination sub-models were refined in order to accurately model and predict periodic flaw face interactions. Through past research concerning heat generation along delaminations within FE modeled ply-drop samples [13], it was determined that heat generation along flaw surfaces is in-fact dependent on contact/target element mesh refinement. Mesh solution convergence was not necessarily verified in that body of research however, which was attributed to the coarsely meshed models' failure to reach harmonic steady-state response. The analyses investigated and carried out in this research however benefit from their reliance on steady-state harmonic analysis. Because the sub-model boundary conditions implemented here represent steady-state harmonic responses, mesh solution convergence is not subject to coarse-model run-times, and achievement of steady state-response within the sub-models can be more easily monitored.

Refinement of Sub-Model Geometries

Since harmonic nodal displacement data is sampled at select nodes along defined sub-model cut-boundaries within the coarse model (harmonic analysis), the nodal mesh at the cut-boundaries within both the full-model and sub-model must be identical (with respect to coordinates and node numbering). ANSYS software does support cut-boundary nodal interpolations with its CBDOF command, which can be used in cases where sub-model and coarse-model meshing do not exactly match. This method, however, is not available in conjunction with harmonic response analysis results. Thus, the cut-boundary nodal meshes must be matched between the "coarse" harmonic analysis model, and each "refined" transient sub-model.

In order to facilitate considerable mesh refinement along the delamination surfaces (and contact elements along those surfaces), buffer zones were introduced into the models. Introduction of these buffer regions within the model allow for ANSYS to automatically transition from very dense element meshes to fairly coarse mesh. Also, By adding these buffer regions between the delamination surfaces and the cut-boundary nodes, ANSYS is able to maintain exterior cut-boundary node numberings and locations. Not being able to use ANSYS's CBDOF function (cut-boundary degree-of freedom interpolation function), the nodal numbering between "coarse" and "refined" models must be preserved in order to pass along sub-model boundary conditions (for the code used anyway). Very complex APDL code could indeed be used to create a user-defined nodal degree-of-freedom interpolation routine, but this wasn't explored. An example of

the mesh transitioning method used to refine sub-model mesh is shown in Figure 32 below.

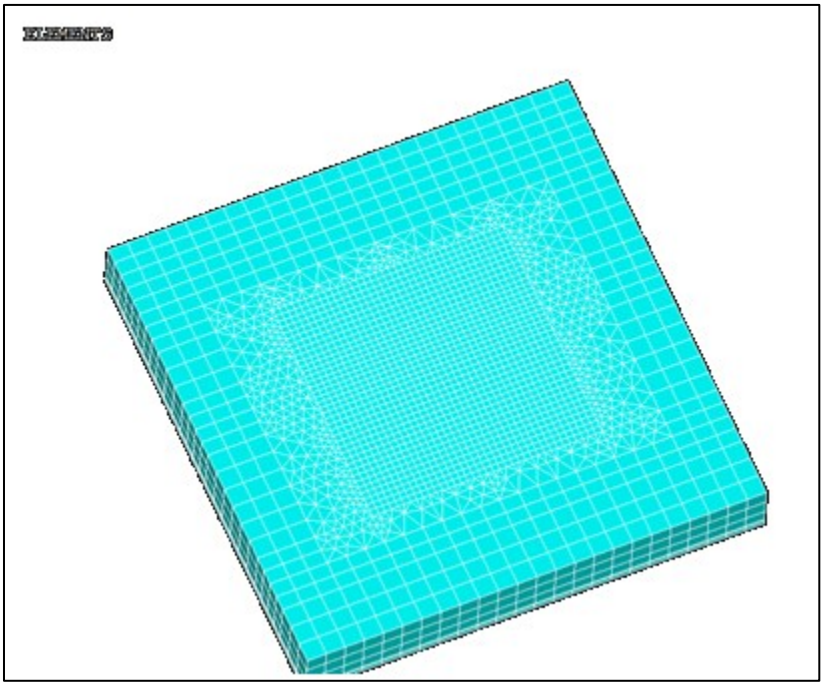

Figure 32. Example of mesh transitioning techniques used to transition from cut-boundary node meshing to highly refined contact element meshing. The sub-model shown is representative of each of the delamination sub-models utilized in the following analyses.

As can be seen in the figure above, the elements surrounding the area of delamination (embedded within the sub-model) are highly refined, while the outer cut-boundary nodes still retain their original coordinates and numbering.

An example of a delamination surface pair, surrounded by the cut-boundary sub-model nodes is shown in Figure 33 below. The nodes, shown as dots, will be subjected to time-varying harmonic displacement conditions (taken from harmonic analysis information) during sub-model transient analyses. The green colored contact elements depict one of the meshed delamination surfaces of an embedded flaw.

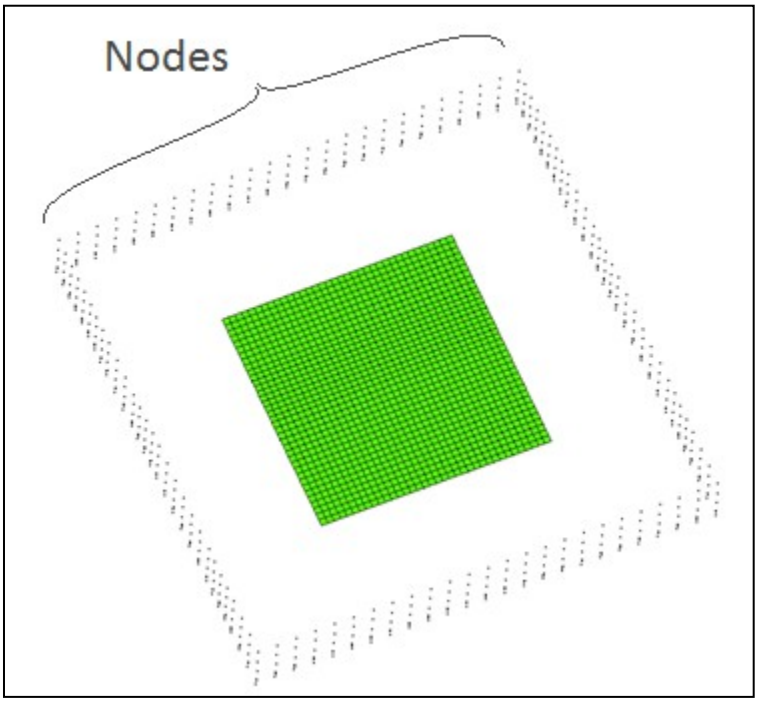

Figure 33. Depiction of a highly-refined, fully-embedded, meshed delamination surface pair, and the cut-boundary nodes associated with the delaminate sub-model.

This mesh refinement technique was applied to all 9 flaw delamination sub-models within the FE model.

Post-Processing Sub-Model Transient Analysis Results To Determine Frictional Heat Dissipation Rates

Analyzing frictional heat dissipation data in ANSYS requires reading in information for each contact element (or target element) that occurs along the delamination in question. ANSYS is able to derive an approximated value of frictional heat energy dissipation due to sliding, by identifying the stress states and reaction forces at frictional points of contact between Contact/Target element pairs, and the amount of relative sliding distance that occurs between these contact/target element pairs at each

time increment (sub-step). Frictional heat dissipation between the ANSYS "conta173" and "targe170"contact elements is given by the nodal result output of FDDIS. Calculation of the FDDIS value is provided by ANSYS as:

$$FDDIS = \frac{(\text{contact friction stress}) * (\text{sliding distance of substep})}{(\text{time increment of substep})} \qquad \text{Equation 18}$$

Where: relative the relative sliding term is non-zero only in instances when contact between a Contact/Target element pair is considered to be within a state of sliding contact.

Calculation of the FDDIS value results in an estimation of the rate of frictional dissipation energy, with units of Nm/(s m^2) or W/m^2.

These values of frictional heat dissipation rate are sampled at each node along a delamination, and the average area specific heat generation along each contact element (containing four nodes) is calculated. With the area specific heat generations calculated, the total heat generation along the entire delamination is analyzed.

Discussion of the methods with which the averaged heat generation along the delamination surfaces was calculated will now be explained. As was noted earlier in this document, localization of heat generating areas is a common occurrence for the pre-stressed plate discussed in this research, due to the magnitude of the separation distances induced between the delamination surfaces by pre-loading. The result of this separation is that heat generation and contact only occur over a relatively small portion of the flaws. Furthermore, many of the elements which to experience frictional contact, may not necessarily experience relative sliding, or produce any frictional heat generation if those elements are considered as "sticking". According to the Coulomb friction model, which

was utilized during these analyses, two contacting surfaces can support shear stresses between the element interfaces. When the equivalent shear stress experienced between contacting elements is less than the critical frictional shear stress (τ_{crit}), no motion occurs, this inhibited motion is termed as sticking. In other words, when contact pressures cause the critical frictional shear stress between two elements to be greater than the shear stresses induced between two contacting elements, then sticking occurs.

The Coulomb friction model implemented within ANSYS [15] defines the critical shear stress, τ_{crit} , and the interface shear stress, τ, as:

$$\tau_{crit} = \mu P + b \qquad \text{Equation 19}$$

$$\|\tau\| \leq \tau_{crit} \qquad \text{Equation 20}$$

where: τ_{crit} = *limit frictional stress*

$||\tau||$ = $\sqrt{\tau_1{}^2 + \tau_2{}^2}$

μ = *coefficient of friction for isotropic friction*

P = *contact normal pressure*

b = *contact cohesion*

The coefficient of friction, μ_{static} , used within this model was set as 0.4, while the contact cohesion coefficient, b, was not utilized, and was left as zero. The selection of frictional coefficient values was discussed in previous chapters.

In order to approximate the steady-state heat generation along each flaw, the frictional heat energy dissipation rates of each flaw element were observed over the sub-model run-times. Heat dissipations along each element were sampled and recorded for every incremental time sub-step throughout the total run-time of each transient analysis.

Not all of this heat generation information is valid however. Even within these transient sub-model analyses, which utilize steady-state harmonic loadings along the sub-model boundaries, short lived transient phenomena are often experienced. These transient responses result in skewed estimations of "steady-state" heat generations along the flaws. Appropriate initial conditions are difficult to apply to the refined nodal meshes of the sub-models, due to alteration of node numberings. The lack of appropriate initial conditions within these sub-models leads is the culprit of producing the transient sub-model system responses.

Preliminary sub-model analyses performed over multiple frequency values revealed that sub-model responses typically reached approximately steady state harmonic conditions at around 6 harmonic oscillations periods. Therefore, a run time equivalent to 6 harmonic oscillation periods was chosen for the transient analyses of each 2"x2" delamination sub-model. The main reason for choosing a short analysis run-time of 6 oscillation periods, rather than defining some arbitrarily large runtime value, was to effectively limit the computational run-times for each analysis. Even the relatively small sub-models of the 2"x2" delaminations are computationally expensive within full transient analysis. In fact, analyses performed for 6 oscillation periods for a properly refined sub-model (mesh refinement solution convergence will be discussed later) requires nearly 3 hours of computational run-time. The smaller sub-models of the medium (1"x1") and small sized (0.5"x0.5") delaminations require much shorter computation time, due to lower node and element counts. Extended transient analysis times of 10 oscillation periods were therefore used for the small and medium flaw sub-models.

With the run-times of each sub-model analyses defined, the method by which averaged frictional heat generation rates are calculated was established. Heat generation data (FDDIS) was compiled from the transient-structural sub-model analyses. After performing each sub-model analysis using either the six oscillation period runtimes (or ten oscillation periods for smaller delaminations), the results of the recorded FDDIS data were selectively chosen from only the very last (approaching steady-state) oscillation. This method aimed to ensure that transient phenomena, such as non-steady state frictional stresses, and contact interactions did not affect predictions of averaged steady-state frictional heat dissipations.

In order to illustrate the localization of contact statuses (an indicator of where frictional heat generation occurs along the flaw surfaces), a surface plot displaying the status of contact along a meshed delamination (refined 2”x2” center flaw) is shown in Figure 34 below. The red regions of the plot ,representing contact status equal to three, denote sticking; the blue regions (contact status equal to one) denote non-contact; the green regions (status equal to two) represent regions which are undergoing frictional contact (frictional sliding); all other regions represent some transition between those points.

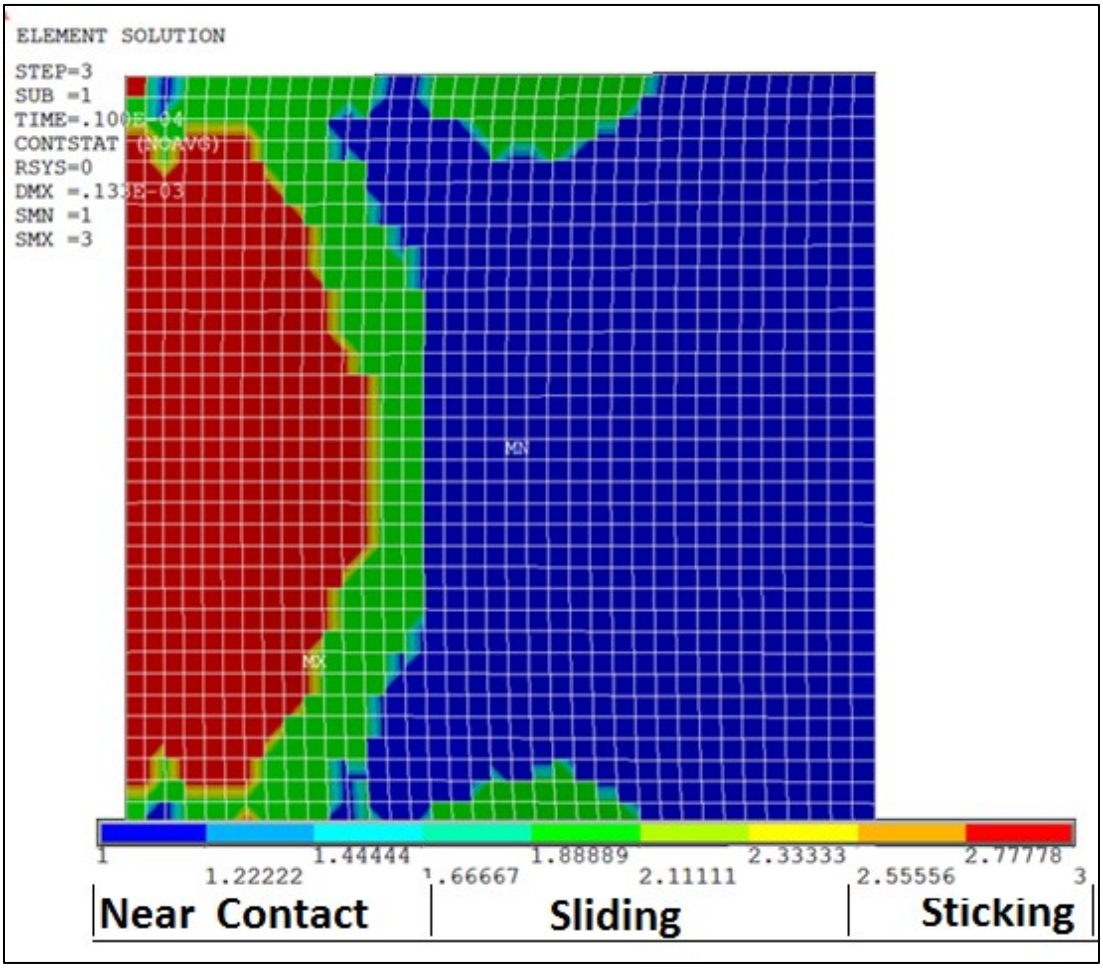

Figure 34. Surface plot of contact status along the Contact/Target element pairs. The areas in which the status transitions from red (3) to green (2) represent frictional sliding (and possible heat generation).

It is apparent from the illustration above, that the results show strong localization of frictional heat dissipation. Only a small portion of the flaw surface is undergoing sliding frictional contact at this point of the oscillation period. When looking at these relationships over time, one observes the frictional "sticking" and "slipping regions migrating about surface, and evolving in a cyclical manner. Once steady-state response has been achieved within the sub-model, the surface interactions between the two

adjacent flaw surfaces of each delamination do indeed behave periodically, as would be expected.

Estimation of the total generating surface area (collective area of heat contributing contact/target elements) was performed via ANSYS APDL code post-processing by sampling the average frictional heat generation which occurs along each individual contact element through one harmonic cycle. Under the assumption that the sub-model had reached harmonic steady state, with respect to structural response, only the last cycle of the analysis was sampled. Clearly, each element does not experience frictional heat generation on a continual basis, but instead, the dynamic frictional contact interactions such as the contact status, contact pressures and relative velocities periodically transitioning within each harmonic cycle.

The frictional heat dissipation along each contact element was then sampled at each sub-step of the final harmonic cycle. From this time history data, the average generation value of each element was calculated. The averaged area specific dissipation rate (frictional heat generation in W/m^2) was then evaluated with a logic loop, in order to determine whether the time-averaged generation rate was significant or not. For the purposes of differentiating between "generating" and "non-generating" elements, a cutoff criterion of 1 W/m^2 was chosen. If an individual element pair's averaged generation was indeed greater than the cutoff value, then the generation value at that element was recorded, and the surface area of the now confirmed "generating" element was also recorded in units of meters squared. This procedure was carried out for every Contact/Target element pair within the sub-model. After all of the elements had been sampled, and their area specific generation rates and contributing areas had been

evaluated, the averaged element generation was calculated. The total generation experienced at each element pair was found by first multiplying each individual "generating" element's area specific heat generation value by its surface area, in order to obtain the total heat generation rate in units of Watts. The total estimated frictional heat generation of the collective group of heat contributing or "generating" elements was finally calculated by adding the generation rates of all "generating" elements and dividing the totaled value by the collective area produced by those elements. The final area specific frictional heat generation, given in units of Watts/meter^2, was then calculated. The Average Total Heat Generation calculated along the flaw surface was found with the following equation:

$$Average\ Total\ Heat\ Generation = \frac{Average\ Heat\ Gen}{unit\ area} \times Contributing\ Area \qquad \text{Equation 21}$$

It should be noted, that at various frequencies, it was discovered that lower frequency modal excitations were not quite completely damped out, even at the conclusion of six oscillation periods. An example of the transience present within the displacement response at the center of the center of flaw number 2 can be seen in the harmonic z-displacement time-history curve (sampled at the top of the plate centered about the delamination) below in Figure 35. The transient behaviour illustrated here leads to difficulty in verifying solution convergence with respect to mesh refinement.

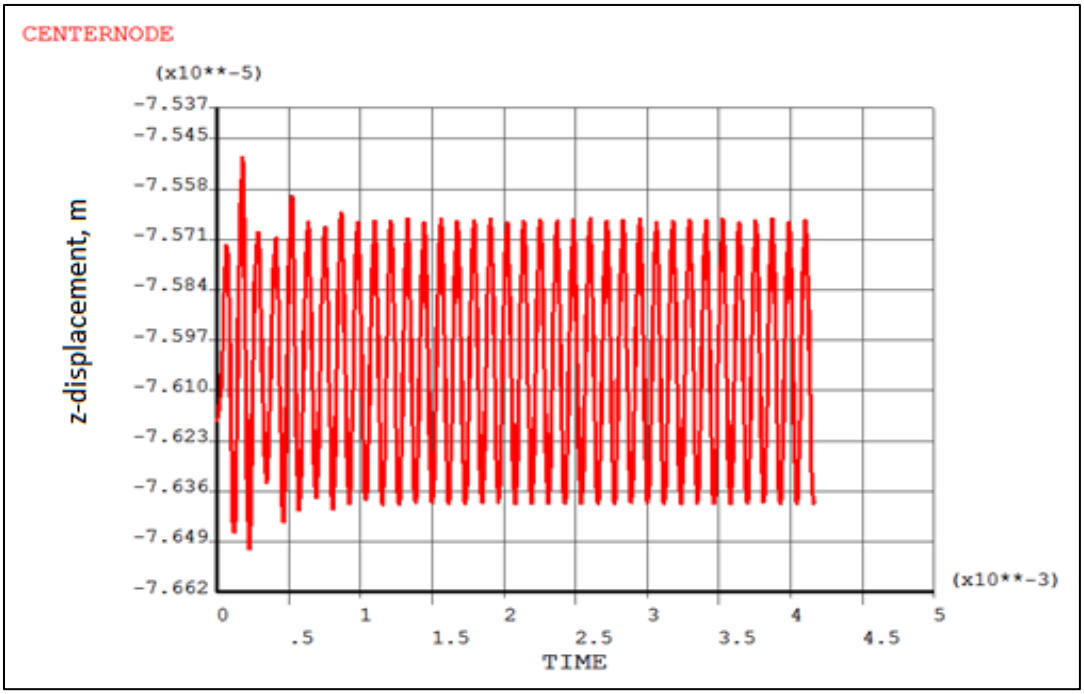

Figure 35. Sampled z-displacement of a node along top center of sub-model. Nearly 6 oscillations are required for the node to begin to approximate steady-state harmonic displacement.

Failure of the sub-model to reach steady-state response may alleviated by allowing the analyses to run for longer model analysis times, allowing for transient responses to be damp out. Extension of analysis run-time would result in even longer computational-times for each sub-model analysis however, which is further compounded by the multiple number of times each analysis is ran throughout frequency sweep routines

Mesh Solution Convergence for Frictional Heat Dissipation

In order to accurately and efficiently perform sub-modeling routines for individual delaminations, mesh refinement solution convergence tests were performed prior to running frequency sweep analyses. After the sub-modeling routine was properly defined to ensure harmonic-steady state response of the model, a mesh convergence test

was carried out at the harmonic driving frequency of 8650Hz. This frequency was chosen arbitrarily as a starting point for the mesh-dependent solution convergence analysis. For the purposes of this analysis, the center 2"x2" delamination sub-model was used. Since the solution of heat generation is the focus of this research, the averaged frictional heat generation rate was analyzed within this solution convergence test. A secondary convergence criterion, for the area over which heat generation occurs, was also chosen, since the generating area is also variable with mesh refinement.

The averaged frictional heat generation was calculated in a manner which ignores non-generating elements. As reported in previous portions of this research [12,13] the regions over which frictional heat generation occur are typically highly localized, primarily due to the effects of static pre-loading of the plate. Again, ANSYS APDL code was utilized to sample and record the frictional heat dissipation occurring at each node of the contact/target elements of the 2"x2" delamination sub-model. From these values, the averaged generation occurring along each element was calculated. In order to account for frequency dependent localization of heating, frictional heat dissipation contributions from elements producing less than 1 Watt/meter^2 were ignored. This method was employed in an attempt to get a more realistic representation of the averaged heat generation occurring over only the "contributing" elements along each delamination. Using this approach, the APDL code routine excludes surface elements which produce little to no heat from calculation. In this manner the total combined area of "contributing" elements (heat gen $\geq$ 1Watt/meter^2) was also estimated.

Sub-model mesh refinement was initialized by starting with a sub-model including an "un-refined" 2"x2" delamination surface covered by 144 Contact/Target

element pairs (12 divisions per surface edge). This initial coarsely meshed sub-model provided a baseline value for subsequent iterations of the mesh refinement analysis. Each consecutive mesh refinement utilized a multiple of the initial 12 element divisions per delamination edge (e.g. 12^2 =144 elements, $(2*12)^2$=576 elements, $(3*12)^2$=1296 elements, etc…..). The results of each individual mesh refinement routine are shown in data tables, Table 4 and Table 5, below.

Table 4. Element Mesh Refinement Convergence Data, Heat Generation, SET 1

No. of Contact Elements	Contact Element Edge Length, (m)	Avg. Frictional Heat Dissipation, (W/m2)	Percent Change Between Values
144	0.004478	3.2573	--
576	0.002239	6.2327	91.35%
1296	0.001493	7.4126	18.9%
2304	0.00112	7.6153	2.66%
Driving Frequency, (Hz)		**8650**	

Table 5. Element Mesh Refinement Convergence Data, Heat Contributing Area, SET 1

No. of Contact Elements	Contact Element Edge Length, (m)	Total Contributing Area, (m2)	Percent Change Between Values
144	0.004478	2.1505E-4	--
576	0.002239	6.4964E-4	202.09%
1296	0.001493	7.0091E-4	7.89%
2304	0.00112	7.0909E-04	1.17%
Driving Frequency, (Hz)		**8650**	

Plotting these mesh convergence relationships via Excel® one can see the converging trends of both the frictional heat dissipation, and the collective area over which generation occurs. The solution convergence plots for averaged area specific frictional heat dissipation rates and the contributing areas of the 2"x2" center delamination for an excitation frequency of 8650Hz are shown in Figure 36 below.

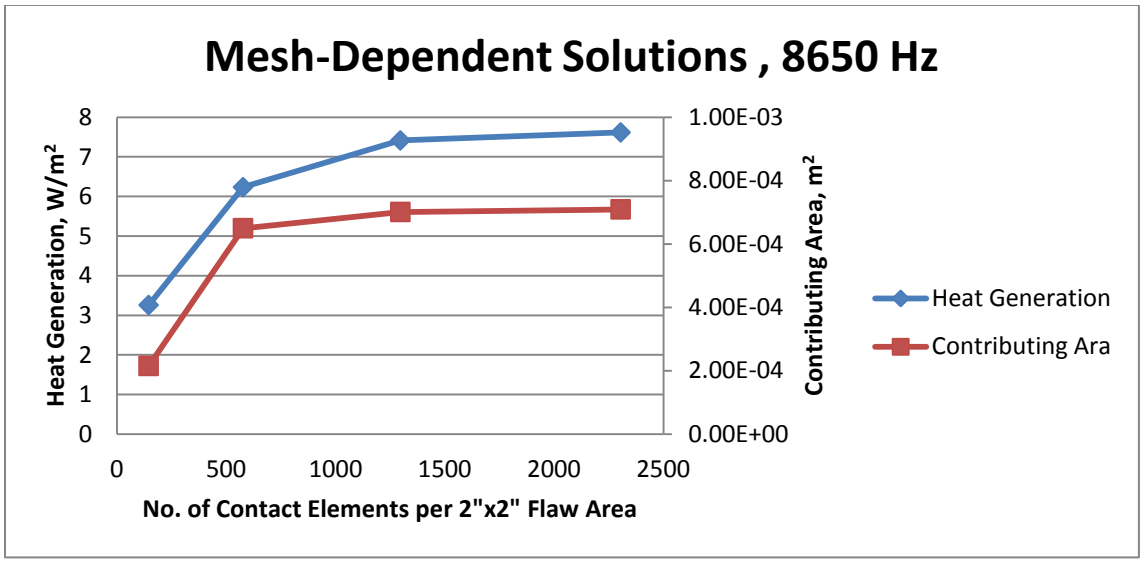

Figure 36. Mesh refinement solution convergence plot for averaged area specific frictional heat dissipation and "Heat Contributing Area"

From the plots above, one can see that for this excitation frequency, solution convergence is indeed achieved through mesh refinement. In order to produce reasonably accurate results (with regards to refinement solution convergence) nearly 1296 elements should be used along each delamination area face. Unfortunately such mesh refinement significantly increases the solution run-time for such analyses. Performing such an analysis (at a single excitation frequency for only 6 oscillation periods) for this 2"x2" delamination sub- requires over 3 hours of solution runtime while using a 2.53GHz 2-core processor PC. Thus, performing a well resolved frequency sweep analysis of a single delamination sub-model over such equipment requires substantial run-time.

Mesh dependent solution convergence analysis was performed at a single frequency during the test described above. In an attempt to further validate the sub-modeling methods used, convergence tests were performed at two additional frequencies within the defined frequency bandwidth at 17600Hz and 27600 Hz, both of which were arbitrarily chosen. Solution results for the frequency 17600Hz show a trend of relatively poor convergence, as seen in the plot below (Figure 37). The data corresponding to these graphs are reserved within the appendix to this document.

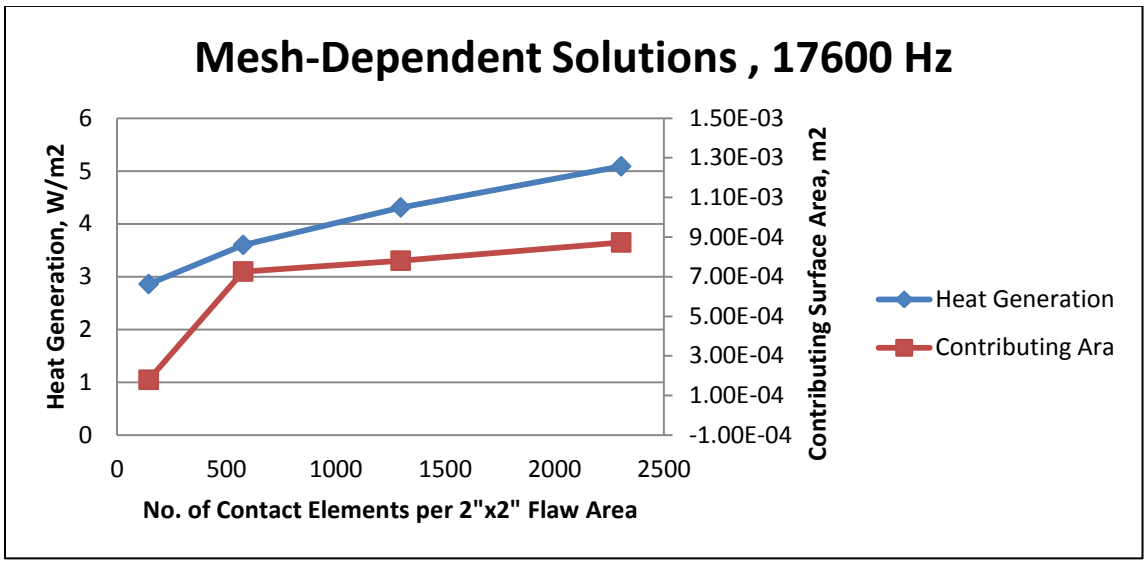

Figure 37. Mesh refinement solution convergence plot for averaged area specific frictional heat dissipation and "Heat Contributing Area"

And finally at a frequency of 27,600Hz, we again find fairly good mesh convergence with respect to both heat generation data and contributing area data, as shown in Figure 38. The data corresponding to these graphs are also reserved within the appendix to this document.

Upon analyzing the convergence trends at these two additional frequencies, 17,600 and 27,600 Hz, it is discovered that mesh dependent solution convergence may not be fully realized completely for all frequencies within the bandwidth. Observing the trends of the mesh dependent solution results of the test carried out for frequency equal to 17,600Hz, it may be inferred that the solution might not converge with further refinement. This lack of mesh convergence is almost certainly attributable to transient responses still being present in the sub- model at the end of the analyses.

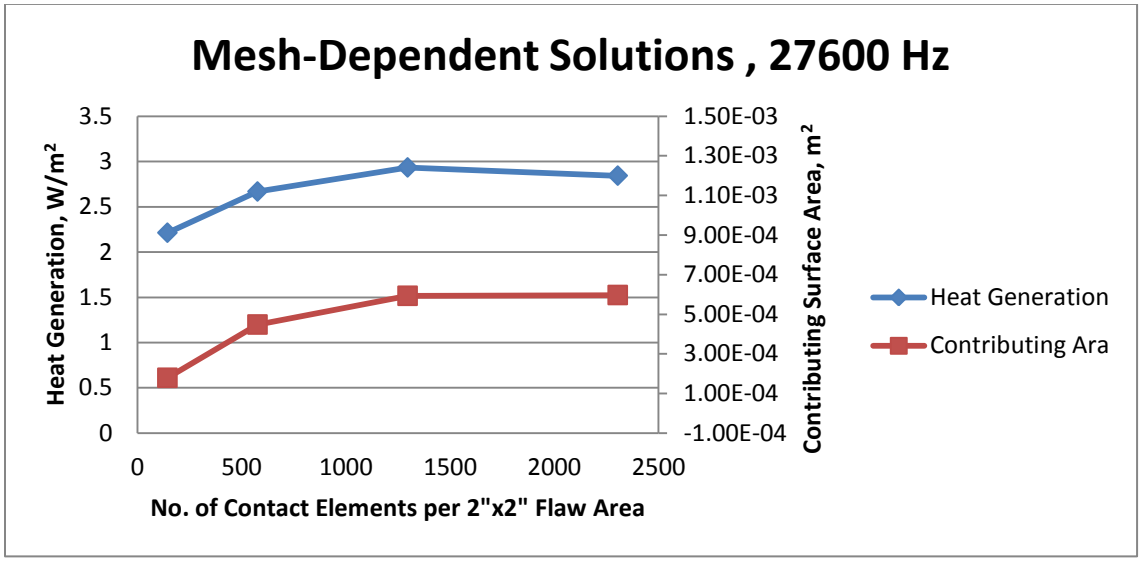

Figure 38. Mesh refinement solution convergence plot for averaged area specific frictional heat dissipation and "Heat Contributing Area"

Though great care has been taken in an effort to reduce these effects, such transient phenomena are very difficult to eliminate at certain frequencies. Short of running each sub-model analysis out for many more oscillation periods, which could result impractical run-times however, there seems to be no readily available solution.

It seems that even though the solutions at some frequencies may be corrupted by transient responses, the data could still provide a general estimation of the heat generation which would be expected to occur along the delaminations. These FE models are, after all, simplified representations of a continuous physical structure. Prediction of surface interactions between the delamination surfaces can therefore only be reliably approximated to a certain degree.

Collection of Heat Generation Rates Through
Frequency Sweeps of Each Flaw

The procedures outlined above were carried out across the entire frequency bandwidth of 800-30,000Hz at every 200Hz increment for each of the nine sub-model analyses. The results of these findings were tabulated and exported into Microsoft Excel® for further processing and plotting. A plot showing the frequency dependent total averaged heat generation along the center 2"x2" delamination (flaw #2) across the frequency sweep bandwidth is shown in Figure 39 below. The values for total averaged heat generation, in units of Watts, were found by multiplying the values fount for areas specific generation by the total contributing surface area for each data set.

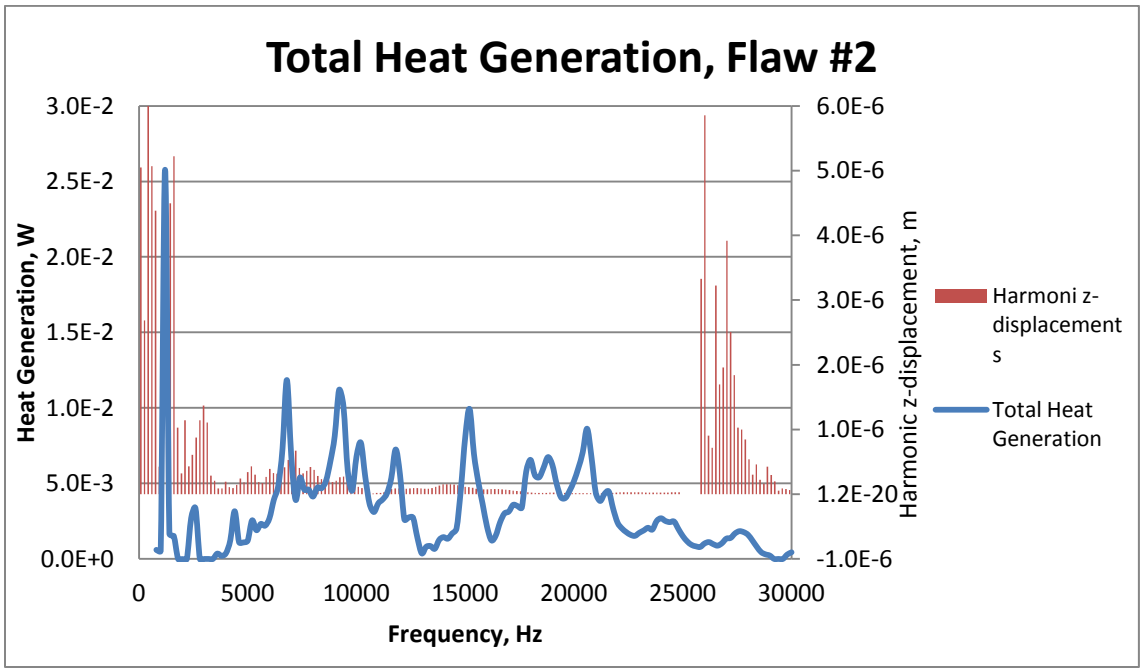

Figure 39. Plot of Total Heat Generation Rate data Recorded throughout Sub-Model Frequency Sweep Analysis.

The secondary axis on the right-hand-side of the plot above also shows harmonic displacement data sampled at top surface of the delamination sub-model, centered at the middle of the flaw. This harmonic displacement data was analyzed in conjunction with the heat generation data in an attempt to correlate a relationship between the two data trends. Correlation of these results have been deemed inconclusive. Though peak total generation values sometimes coincide with peak harmonic z-displacements, the correlation appears to be quite weak.

Additional Information such as the average area specific heat generations and average contributing areas were also plotted within Excel®. Examples of these plots are shown in Figure 40 and Figure 41 below.

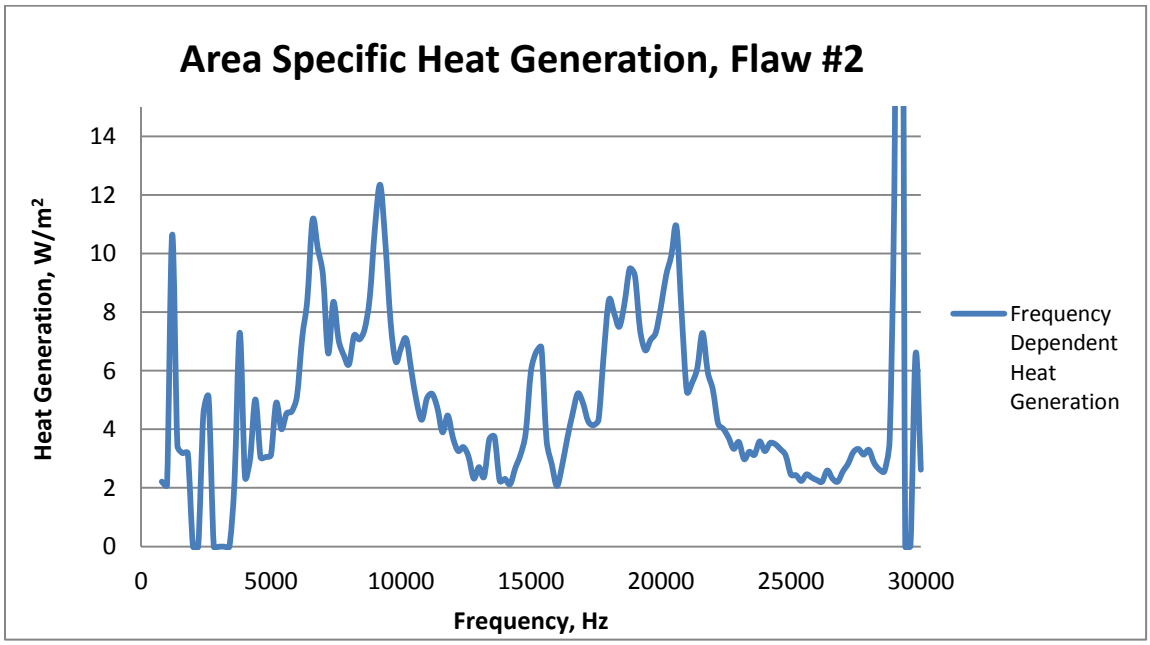

Figure 40. Frequency sweep data for area specific heat generation of Flaw#2.

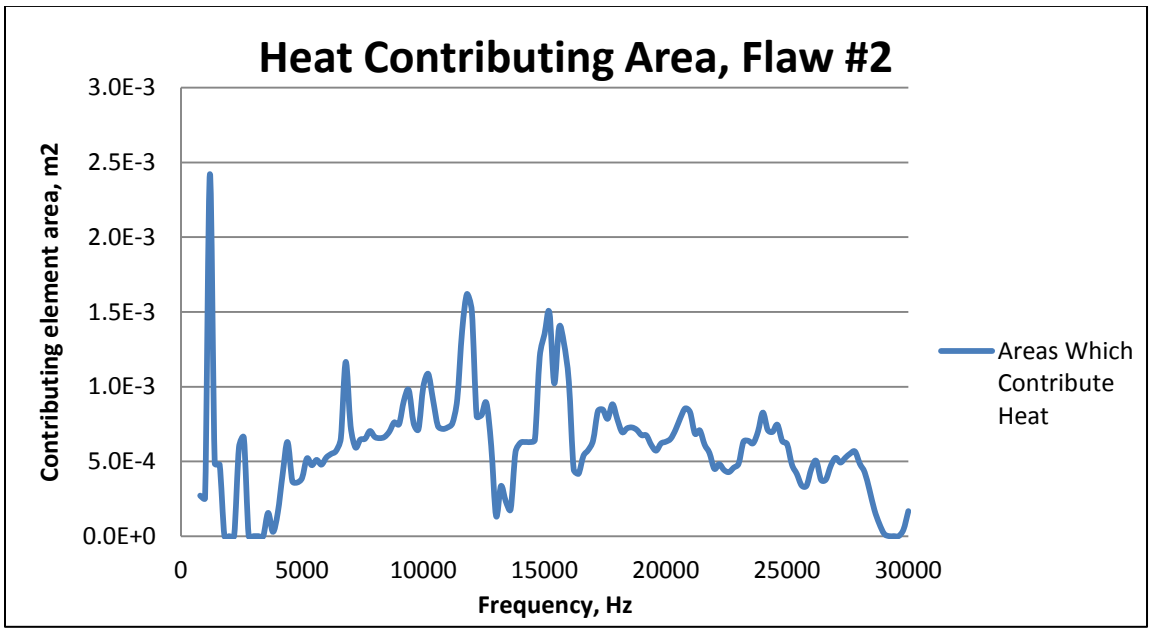

Figure 41. Frequency sweep data for heat "contributing" surface area for Flaw#2.

The results for Flaw#2 have been discussed and displayed here; the results for each of the other nine flaws were analyzed, but are omitted here, and instead are reserved within the appendix to this document.

ESTIMATING THERMAL DETECTION TIMES CORRESPONDING TO ANSYS PREDICTED HEAT GENERATIONS

Up to this point, discussions of the analyses solving for heat generations, and contributing areas, corresponding to each flaw have been discussed. One of the ultimate goals of this research however, was to create a prediction model, aimed at predicting whether certain flaws would be detectable under IR thermographic sampling.

A rather novel approach to predicting thermal detection times was implemented and refined during this research. Rather than running a multi-physics FE analysis to calculate the heat diffusion through each sub-model, which would add considerable time to an already cumbersome analysis, a method of predictive data curve-fitting was used to estimate detection times. This method was introduced earlier in this research project by D. Platt, but had formerly faced difficulties in achieving acceptable data curve-fit quality. The ultimate goal was to develop a function that would indicate how long it would take to detect a change in surface temperature caused by a sufficiently large variety of heat generating flaws. This method has undergone further study and will be discussed in the next section.

This body of research is based on utilizing an infra-red thermal detection camera to detect heat signatures during empirical vibrothermographic testing. Using the camera, the operator must be able differentiate generative heat sources from instrumentation and environmental noise in order to properly detect an embedded flaw. The IR camera detection system used required that a temperature gradient of 0.5 Kelvin between flaw heat signatures and the surrounding ambient plate material be discernible, in order to

reliably differentiate between noise and heat diffusing from areas of generating frictional heat. Furthermore, the data filtering algorithms used to process the IR camera data required that the temperature gain occur over at least a 100 pixel (10x10sqaure) area of the IR camera image.

Creation of Detection Time Data Sets

ANSYS FEA software was again utilized, this time to perform thermal diffusion analyses in an attempt to estimate the times required to detect heat signatures along the various flaws of the 24”x16”x0.54” plate. Rather than performing thermal diffusion analyses for all nine flaw sub-models, with one analysis for each of the frequency-dependent specific heat generation and contributing area combinations estimated during the previous transient structural analyses, another generic parametric model was created. This model was designed to incorporate a single, fully-embedded, planar, circular flaw. The analysis was performed by creating a model with particular flaw characteristics, designed according to a selected combination of flaw parameters. The flaw parameters used to define the model geometry and loads were as follows: area specific flaw heat generation (W/m^2), flaw size (projected surface area, m^2), flaw depth (percentage of plate thickness from top surface, m), and camera distance (distance from focal point of IR camera to plate surface, m). The analysis was performed by permuting through each possible flaw parameter combination during model creating and then solving for the required thermal detection times.

The parameter sets used were defined according to the flaw geometries that were present in the 24”x16”x0.54” model analyzed in the previous sections of this report. The selected parameter sets allow for a well resolved data set which fully encompasses any resultant parameter set that might have been estimated by the transient sub-model heat generation analyses carried out in the previous sections. In other words, from the results of the vibro-thermal structural analyses, we can extract the area-specific frictional heat generation rates, and the total contributing surface area data, for any of the nine flaws within the plate model, choose a camera distance, and that particular parameter combination will fall somewhere within the prescribed parameter set. If sufficient thermal detection time data can be produced from a thermal model parameter-permutation analysis, and an adequate data curve-fit (predictive-curve-fit equation) can be produced, then the time-to-detect for any given parameter combination (any possible combination for the plate model) may be predicted to some level of certainty. The flaw parameters employed throughout the analysis are displayed for reference in

Table 6 below. Running through all possible permutations of the parameter sets, a data set of 900 thermal detection time data points was created.

Table 6. Parameter Sets Used in Producing Thermal Finite Element Data.

Thermal Model Parameter Sets										
Generation, W/m^2	**1**	**10**	**20**	**30**	**40**	**50**	**60**	**70**	**80**	**90**
Flaw Size, m^2 ($x10^4$)	1.29	4.01	6.74	9.46	12.2	14.9	17.6	20.4	23.1	25.8
Depth, %	0.1	0.15	0.4							
Camera Distance, m	0.6096	1.2192	1.8288							

The material properties implemented within the thermal models were provided by Resodyn Corporation, and are representative of epoxy/glass composite samples manufactured for this project by both Resodyn and the MSU composites group. The coefficients of thermal conductivity, k, employed in the models, are given as orthotropic material properties as outlined in Table 7 below.

Table 7. Thermal Model Material Properties

Material Properties Employed within Thermal Analyses		
Mass Density	1867	Kg/m^3
Specific Heat capacity	879	J/kgmK
Thermal Conductivity, k_x	0.44	W/mK
Thermal Conductivity, k_y	0.44	W/mK
Thermal Conductivity, k_z	0.35	W/mK

During the thermal analyses, the heat generating regions were represented as circular flaw areas, which experience uniform heat generation across the entire flaw surface. The purpose for implementing circular flaws and circular detection regions was to eliminate the effects of complex flaw geometries. As can be seen in the solid body and Finite Element models shown in Figure 42 (a) & (b) below, a series of concentric circles, which represent the flaw geometry (embedded within the model), and the various IR detection points are incorporated into the model. The addition of circular detection rings within the solid model facilitates nodal mesh refinement along these detection regions within the meshed Finite Element model.

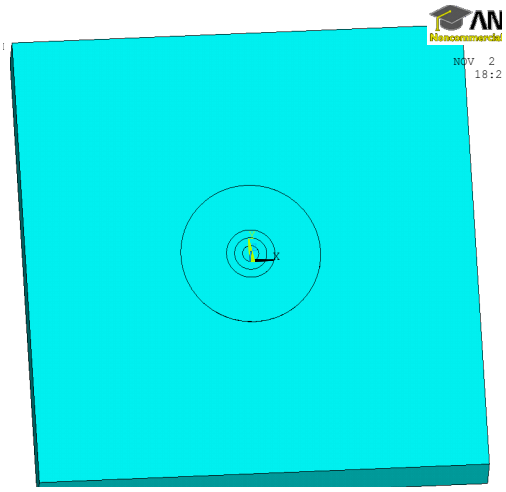

(a.) Solid-body model displaying multipe thermal detection rings

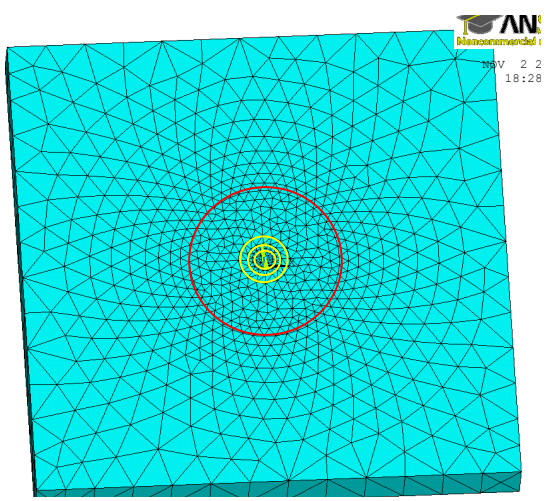

(b.) Meshed finite element model.

Figure 42. Example of the model used during thermal detection analyses.

In the illustrations above, the circular regions representing the thermal detection rings are shown highlighted in yellow within the meshed FE model, the circular flaw geometry is also shown highlighted in red. The size of the circular area representing the flaw geometry (highlighted in red) was varied according the parameter flaw size. The sizes of the three rings representing the detection regions (highlighted in yellow) weren't varied from model to model, but remained constant. These concentric yellow rings are equivalent in size to a 100pixel detection area, each corresponding to a prescribed distance between the IR camera and the sample. The inner yellow ring corresponds to the shortest camera distance used during the analysis; three camera distances (2ft, 4ft, and 6ft) were assumed during the analysis. The circular detection regions were introduced in order to selectively place detection nodes at points along each circumference. During each thermal analysis, the temperatures at each detection node are sampled and compared to the detection criteria specified for the analysis (0.5K temperature increase). Once

every single node along a detection ring reaches the 0.5K increase in temperature, then the criteria is deemed as satisfied for that ring, and the elapsed analysis time (detection time) is recorded. If every node along the detection area has not experience a 0.5K rise in temperature, then the criteria was deemed as un-satisfied, and the flaw parameter set was considered to experience a "failure to detect".

During the initial conceptualization and design of these models, a square 10x10 pixel detection area was prescribed. However, later during the thermal analyses of these models, certain difficulties with regards to the satisfaction of detection criteria were realized. For smaller flaws occurring fairly close to the surface, fairly large temperature rises would occur within localized regions due to the relatively low thermal conductivities and diffusivity of the material. The magnitudes of the temperatures along these heat signatures were surely great enough to enable detection, but the implementation of rectangular thermal detection areas often times resulted in a good majority of the detection nodes satisfying the detection temperature criteria, while relatively few did not. The temperature contour plot in Figure 43 below shows a representative example of this behaviour.

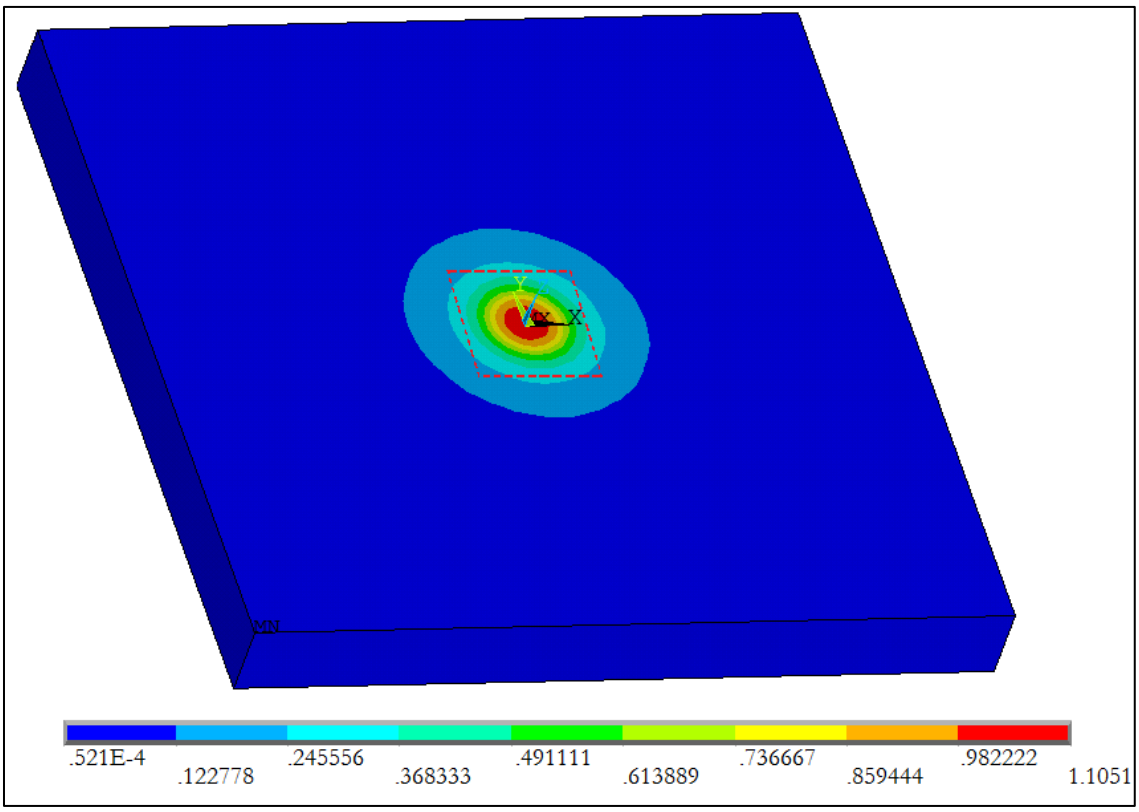

Figure 43. Rectangular thermal detection regions often result in detection failure due to a relatively small number of nodes not meeting detection criteria.

The dotted red line represents a rectangular detection area. If the temperature contour plot in this example represented a steady state thermal response, then a "failure to detect" would be assumed. In instances similar to this one, where "detection" is achieved at all nodes except at a few (at the detection area corners), a somewhat ambiguous situation is encountered. Has the flaw been detected, or not? In order to reduce the likely-hood of these situations, circular detection rings were implemented.

In order to expedite the process of determining detection times for every parameter combination, static-thermal analyses were performed prior to transient analyses. If thermal detection was achieved at any of the detection rings during static analysis, then a transient analysis was subsequently initiated. The "time-to-detect" was

calculated from these transient thermal analyses. During the transient analysis steps, the heat diffusion through the plate was analyzed for a maximum of 30 minutes of simulation time. The thermal detection criteria was intermittently checked at a specified sampling period for each of the detection rings which had fulfilled the detection criteria within the preliminary static analysis. Once the criteria had been met for each ring, or 30 minutes of analysis time had elapsed (whichever occurred first), the transient analysis was aborted and the next model parameter combination was analyzed. In cases where detection wasn't achieved for either the static or transient analyses, the thermal detection time was recorded as a -1 or a -5 respectively. Post-processing of the time-detection data then allowed for these "un-detected " parameter combinations to be identified and selectively omitted from the finalized data set; this final was subsequently used for curve-fitting procedures

With detection times for all 900 permutations of the possible parameter combinations identified, the thermal response of the flaw heat dissipations within the plate were adequately characterized. Using the thermal detection time information included within this data-set (which is specific to 0.54in thick plates used for this research), a curve-fit approximation equation was derived

Development of Thermal-Detection-Time Predictive Curve-Fit Equation

The goal of compiling a comprehensive set of thermal detection time data was to produce a function of the form

$$T = f(H, d, s, A) \qquad \text{Equation 22}$$

where T denotes the time required to detect the flaw, H is the flaw's heat generation rate, d is the depth at which the flaw occurs (distance from the top surface of the plate), s is the projected surface area of the flaw, and C is the distance between then camera and the top surface of the plate. The predictive function was created by producing a curve-fit approximation of the comprehensive thermal detection time data set discussed in the previous section. In order to accomplish this task, an appropriate design of experiment (DOE) software package was utilized.

The software package Design-Expert®v8, by STAT-EASE Inc., was chosen for the task. The program's "Response Surface Method" curve-fitting algorithms were used in order to produce curve-fit approximation of the thermal detection time data. The majority of the data points within the raw data set were used in creating the curve-fit, however, some "trouble" data-points tended to cause great difficulty in achieving an appropriate curve-fit over the entirety of the data set. Creation of the 4D (four parameter dimensions) response surface fit therefore required that the raw data be strategically reduced in a fashion which omits data points which fall on the fringe of data approaching "un detectability". Design-Expert's linear constraint abilities were implemented in order to eliminate this problem data (approaching failure to detect) corresponding to small flaw sizes and low heat generation values. The linear constraint used within the curve-fitting

procedure, produced with the aid of the Design-Expert®v8 multi-linear constraint utility, is displayed in Equation 23 below.

Constraint

Location of Data $0.003496 \leq 0.0002 * A - 0.022 * B + 6.000 * C$ Equation 23

Where the variable A equals heat generation, B is the flaw depth and C is the flaw size. This particular constraint equation eliminates problem data the corner of the experiment's factorial subspace which asymptotically approaches un-detectability (detection time greater than 30 minutes).

With the design of experiment sub-space refined, the curve-fitting analysis was continued. In order to produce a good fitting, manageable, predictive curve-fit equation for the response surface fit, a cubic polynomial function was used with Design-Expert's built in "user-defined" response surface method design algorithms. The software's automatic "backward" model reduction method was ultimately employed in order to reduce the final equation form by eliminating any non-significant polynomial terms from the equation.

In an attempt to produce a satisfactory curve-fit of the data, a multitude of function power transformations were explored. An inverse square-root power transformation seemed to yield the best results for matching the trend of the data. Accordingly, the final curve-fit equation results were constructed using the inverse square root transformation. The basic form of the power transformation used is as follows,

$$y' = \frac{1}{\sqrt{y - k}} \qquad \text{Equation 24}$$

where y' is the transformed solution output, y is representative of the solution for time-to-detect (thermal detection time predicted by the curve-fit equation) and k is a constant offset. The constant offset was not necessary, and was set to zero since no negative values occur in the system response data set (detection times always greater than zero). This final predictive curve fit equation was produced utilizing the inverse square-root power transformation:

$$\frac{1}{\sqrt{Time\ to\ Detect}} = -0.094456 + 8.37492 \times 10^{-3}\mathbf{A} + 0.24035\mathbf{B} + 79.57879\mathbf{C} - 2.14261 \times 10^{-3}\mathbf{D} - 0.017478\mathbf{AB} - 0.59053\mathbf{AC} - 5.10621 \times 10^{-5}\mathbf{A}^2 - 0.39462\mathbf{B}^2 - 38931.11618\mathbf{C}^2 - 0.025202\mathbf{ACD} + 1.01500 \times 10^{-5}\mathbf{A}^2\mathbf{B} + 3.09704 \times 10^{-3}\mathbf{A}^2\mathbf{C} + 0.022865\mathbf{AB}^2 + 48.52688\ \mathbf{AC}^2 + 5.30598 * \mathbf{B}^2\mathbf{C} + 271.67074\mathbf{C}^2\mathbf{D} + 1.77928 \times 10^{-7}\mathbf{A}^3 + 6.82117 \times 10^{6} * \mathbf{C}^3$$

Equation 25

Where: *A= Specific Heat generation*

B= Depth

C= Flaw Size

D= Camera Distance

Taking the inverse square of both sides, the thermal detection time ("Time to Detect") for any parameter combination withing the defined sub-space can be reasonable approximated via eq. Equation 26.

$$Time\ to\ Detect = [-0.094456 + 8.37492 \times 10^{-3}\mathbf{A} + 0.24035\mathbf{B} + 79.57879\mathbf{C} - 2.14261 \times 10^{-3}\mathbf{D} - 0.017478\mathbf{AB} - 0.59053\mathbf{AC} - 5.10621 \times 10^{-5}\mathbf{A}^2 - 0.39462\mathbf{B}^2 - 38931.11618\mathbf{C}^2 - 0.025202\mathbf{ACD} +$$

$$1.01500 \times 10^{-5}\mathbf{A}^2\mathbf{B} + 3.09704 \times 10^{-3}\mathbf{A}^2\mathbf{C} + 0.022865\mathbf{A}\mathbf{B}^2 + 48.52688\,\mathbf{A}\mathbf{C}^2 + 5.30598 * \mathbf{B}^2\mathbf{C} + 271.67074\mathbf{C}^2\mathbf{D} + 1.77928 \times 10^{-7}\mathbf{A}^3 + 6.82117 \times 10^{6} * \mathbf{C}^3]^{-2}$$

Equation 26

It should be noted that during the curve-fitting procedures employed during this analysis, model hierarchy was not maintained, primarily in an effort to minimize the overall size of the final resulting equation (Equation 26).

A representation of the 4D surface fit (2 parameters are held constant to produce the 3D plot) is shown in Figure 44 below.

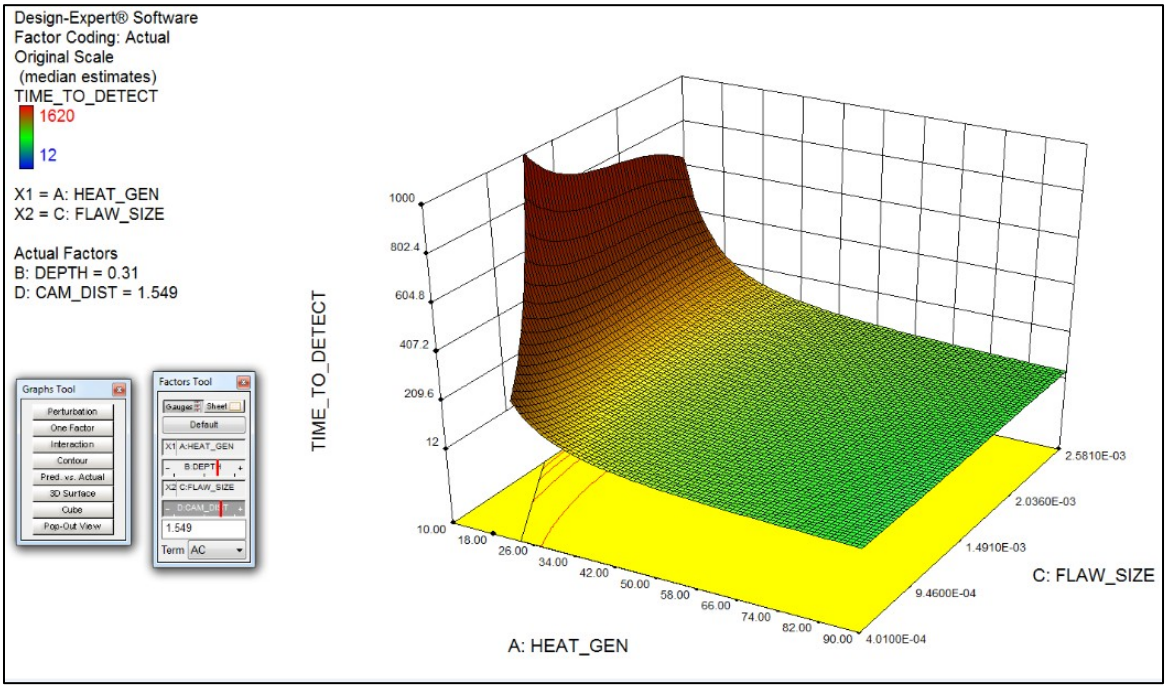

Figure 44. 3D surface plot representation of detection time response for given parameter combinations, Flaw Depth and Camera Distance are held constant. The left-most (troublesome) portion of data has been purposely ignored using linear constraints.

Design-Expert's built in model-quality analysis options were used to investigate the quality of the curve-fit with regards to the input detection time data. The studentized plot of "Actual" and "Predicted" detection time values is shown in Figure 45 below.

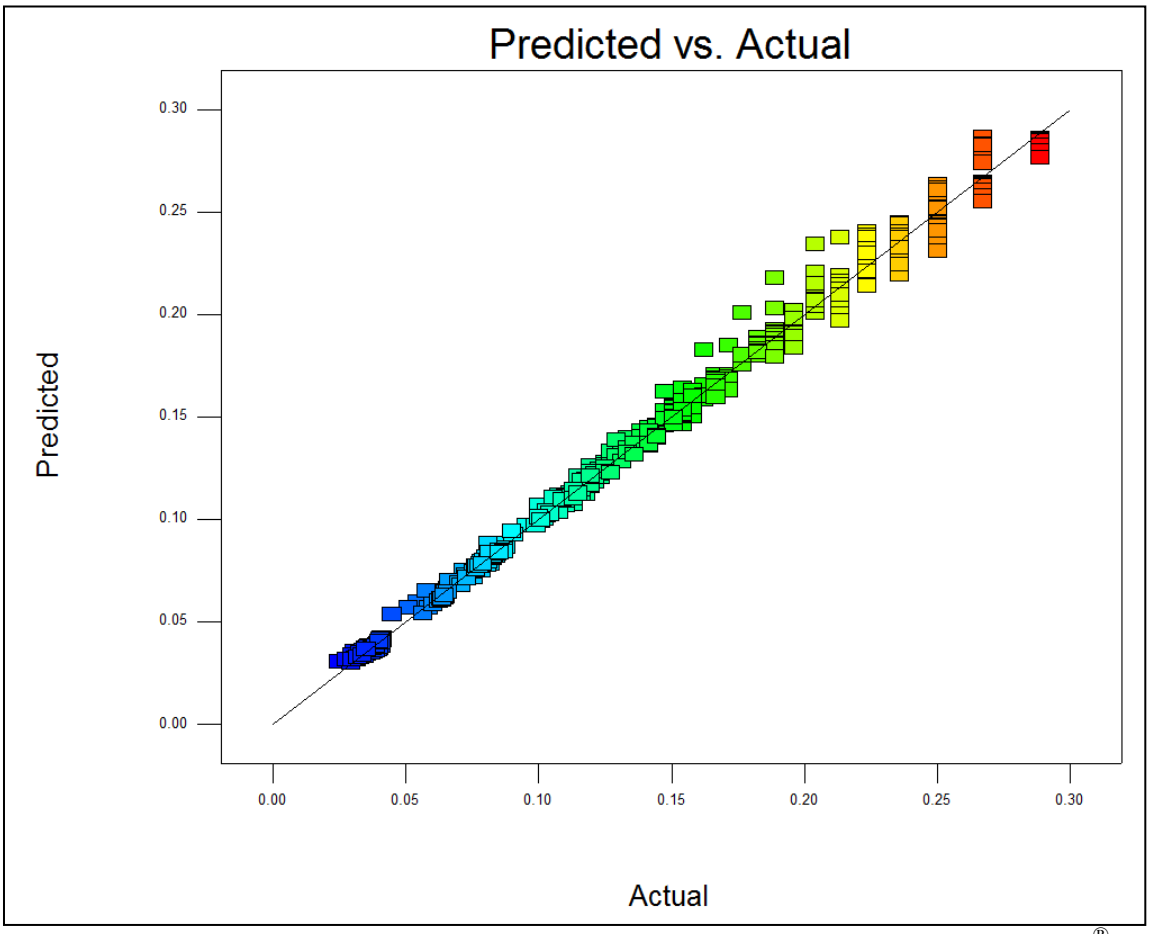

Figure 45. Quality analysis of the linear regression model produced in Design-Expert®v8, comparisons are between curve-fit predicted values and actual FE data thermal detection time values.

Ultimately the resulting curve-fit equation (Equation 26) was imported into MATLAB® and Microsoft Excel® in order to further analyze the quality of the fit with regards to the thermal detection time data set. In these procedures, each data point within the thermal detection time data (which was used in producing the curve-fit equation) was

compared with the value predicted by the curve-fit equation (and the parameter set corresponding to that particular data point). The quality of approximation for each data point within the thermal detection time data set was rated according to the percent error between the FE produced thermal detection time data (true value, T), and the curve-fit equation produced predictive data (experimental value, E) according to:

$$\%Error = \left|\frac{T-E}{T}\right| * 100 \qquad \text{Equation 27}$$

For the purposes of determining the thermal detectability through the approximation of predicted detection times, a percent error value of less than 10% was considered adequate, while values less than 20% were considered to be marginal. Using these criteria, it has been demonstrated that the produced curve-fit equation exhibits good quality of fit over the majority of the FEA produced thermal detection time data set.

Predicting Thermal Detection Times Corresponding to Flaw Sub-Model Heat Generation Data

As was mentioned at the outset of this document, one of the ultimate goals of this body of research is to produce an algorithm routine which can accurately assess the detectability of heat signatures produced (due to frictional heat dissipations) within the designed plate. The development of an equation to predict detection times of the flaws within the plate was outlined in the previous section. Using this predictive equation in conjunction with frictional heat dissipation data, derived from the transient sub-model analysis procedures outlined in chapter 7, predictions of thermal "detectability" for each flaw were made throughout the defined frequency set. The assessment of detectability was made according to whether or not the parameter combination (heat contributing area, and area

specific generation rate, and flaw depth) produced within a flaw for a given frequency, would produce a value of detection time which is less than some user-defined time period. These predictions were performed using the aforementioned parameters in conjunction with the detection time predictive equation. For the purposes of estimations explored here, a camera distance of 2 feet was utilized. The detection times produced for each of the frequency dependent parameter combinations for all nine flaws were analyzed. The results for estimated detection times corresponding to Flaw number #2 are shown as an example in Figure 46 below.

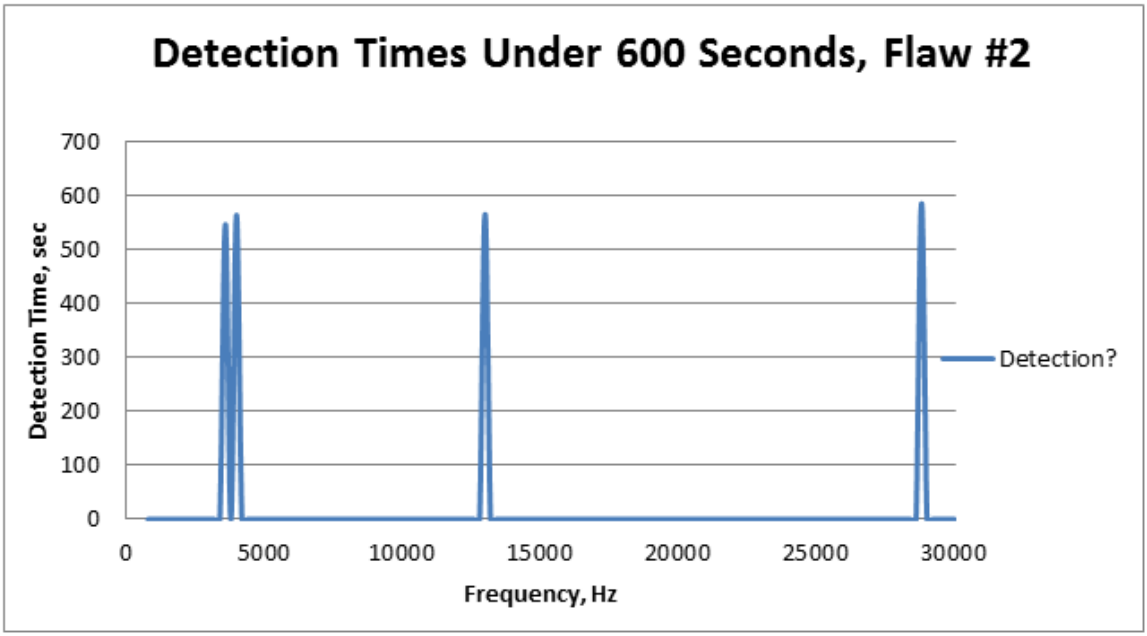

Figure 46. Detection time estimations for each of the frequency dependent flaw parameter combinations of Flaw #2

The final step to the development of this routine was to verify the validity of its results through comparisons with empirical data

ANALYSIS OF THERMAL DIFFUSION MODEL PARAMETERS

Parameter Combinations and Their Effects on Detectability

The parameter permutation solutions discussed above provides a relatively high-resolution data set with which to characterize the thermal detection time responses for arbitrary flaw parameter combinations which may occur within the plate. During the analyses, however, numerous parameter combinations failed to achieve the temperature rise detection criteria of 0.15K. Observing the FE predicted thermal detection time data, one can clearly discern that failure to achieve detection, or "Failure to Detect", commonly occurs at parameter combinations employing both low heat generation rates, and small flaw areas. In-fact, all parameter combinations which included the minimum heat generation rate value (for this analysis 1 Watt/meter^2) failed to achieve detection. A subset (about one third of the total) of this thermal detection time data is displayed in Appendix B. The data subsets shown correspond to the three smallest values of flaw size used in the parameter permutation analysis.

Using STAT-EASE Design-Expert v.8®'s parameter perturbation analysis, the effects that individual parameters have on the thermal detection time response can be analyzed. For the response surface design, a perturbation plot shows how the response changes as each factor moves from a chosen reference point, with all other factors held constant at a reference value. The plots shown in Figure 47 through Figure 50 are examples of such perturbation analysis outputs. Within the parameter sets used, the parameters of "camera distance" and "flaw depth" appear to have weak effects on the likelihood of detection across the majority of the data set. An exception to this occurs at

parameter combinations incorporating both extremely small flaw sizes and heat generation rates.

It should be noted that this type of perturbation analysis offers insight on the parameter dependent systems response only at a single point within the model (at the particular parameter combination chosen). In order to gain a more comprehensive understanding of the relationships between individual parameters and system response, multiple perturbation analyses can be carried out at various regions of the parameter sub-space. Since it was expected that parameter combinations including both large camera distance, and large depth from the surface would result in the most difficulties in achieving thermal detection, the focus of the following analysis was performed holding these parameters constant at their maximum values,(camera distance and flaw depth equal six feet, and 40% thickness respectively). After limiting the analysis to this particular model subspace (Figure 44 closely represents the response behaviours within this model sub-space), the effects of parameter perturbations were investigated for various combinations of Flaw Size and Heat Generation Rate.

The behaviours at the edges of the parameter domains for both Heat Generation and Flaw size (recall Camera distance, and depth have been fixed) were first investigated. Looking at the model region incorporating smaller values for both Heat Generation and Flaw size, perturbation analysis demonstrated that Thermal Detection Time (system response) is most significantly affected by the system parameters Heat Generation (Parameter A), and Flaw Size (Parameter C) as shown in Figure 47 below. At this portion of the model space, the depth of the flaw begins to have a more significant effect as well.

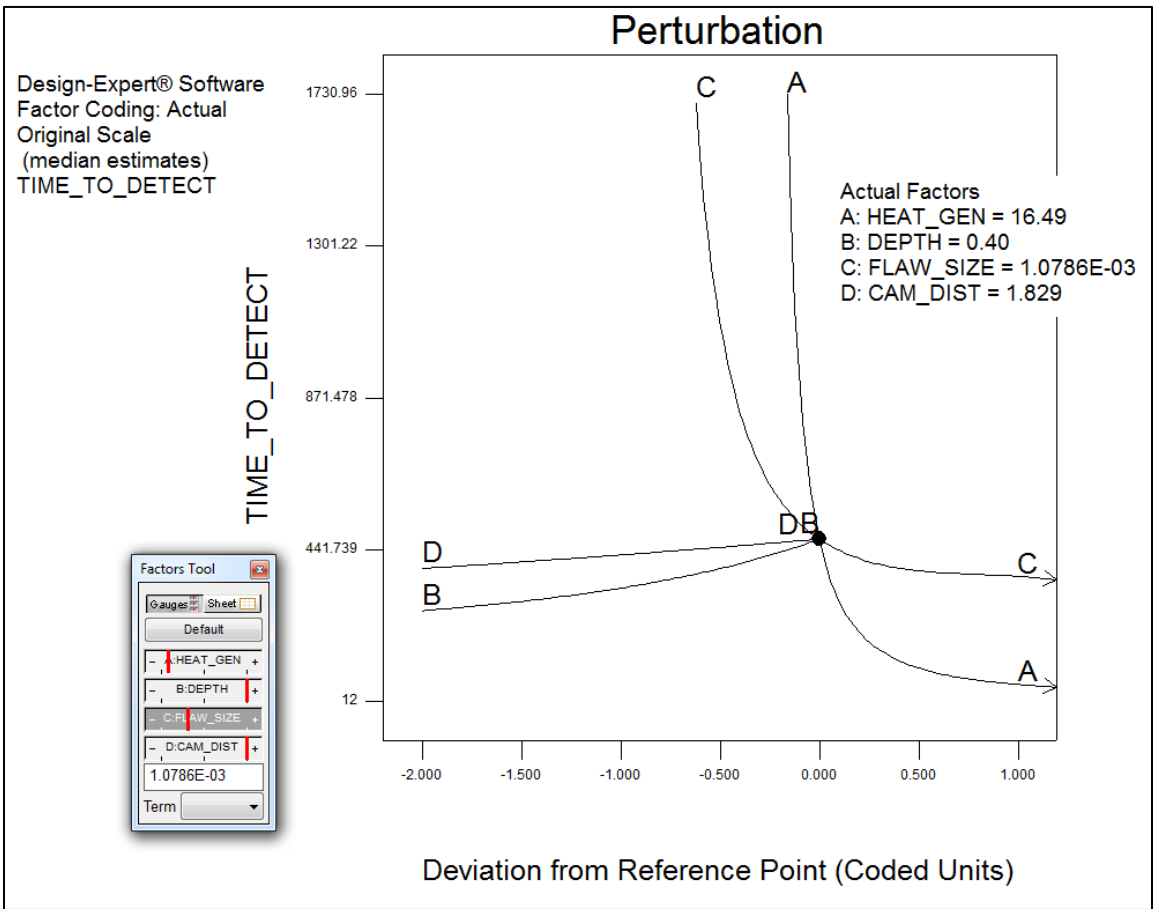

Figure 47. Parameter Perturbation Analysis at regions of low heat generation and small flaw sizes.

Next, the effects at the region of the model incorporating maximum Flaw Size (all parameters at maximum, except Heat Generation) were investigated, as shown in Figure 48. Again the Thermal Detection Time response is dominated by the parameters of Heat Generation and Flaw Size, though more so by the Heat Generation Rate.

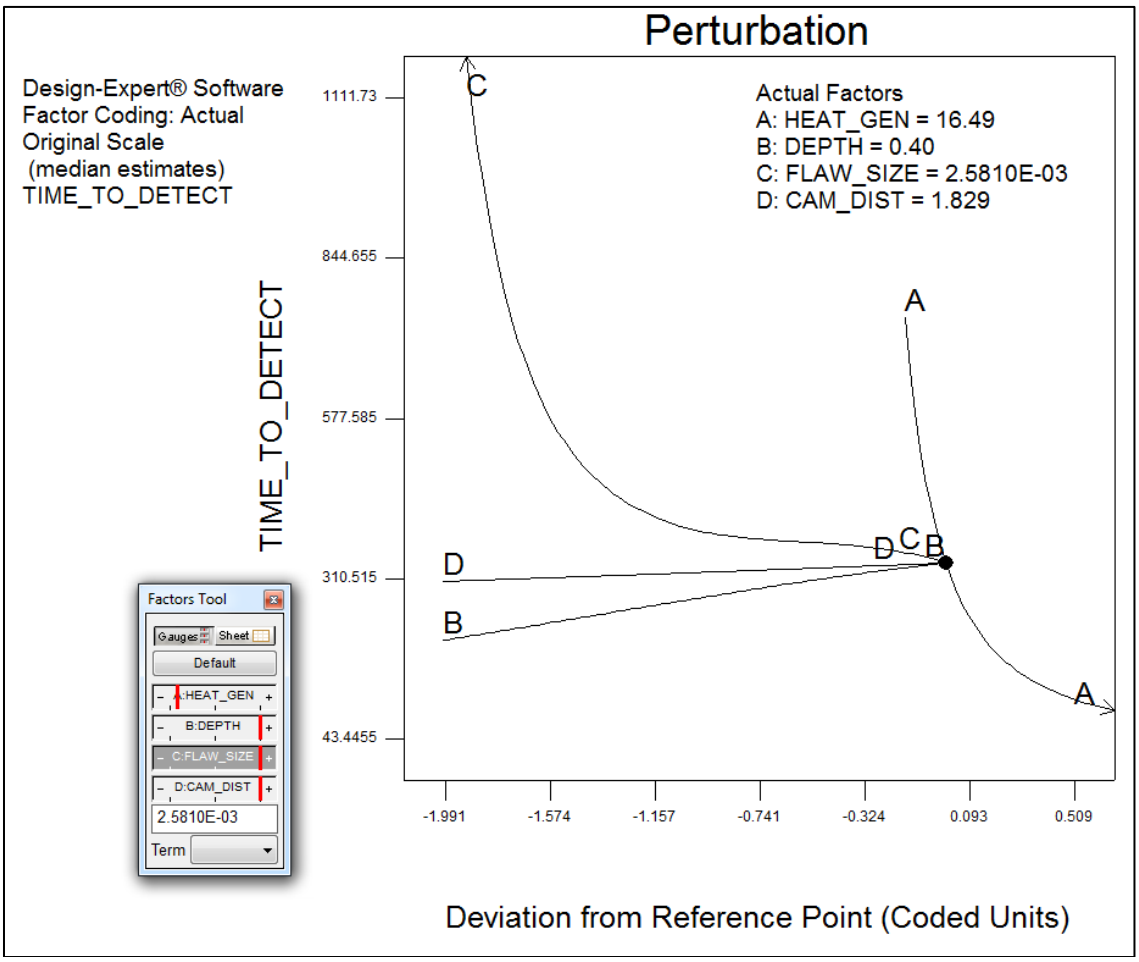

Figure 48. Parameter Perturbation Analysis at region of low heat generation and maximum flaw size.

An analysis surrounding parameter combinations incorporating large Heat Generations and Flaw Sizes was also carried out, as shown in Figure 49 below.

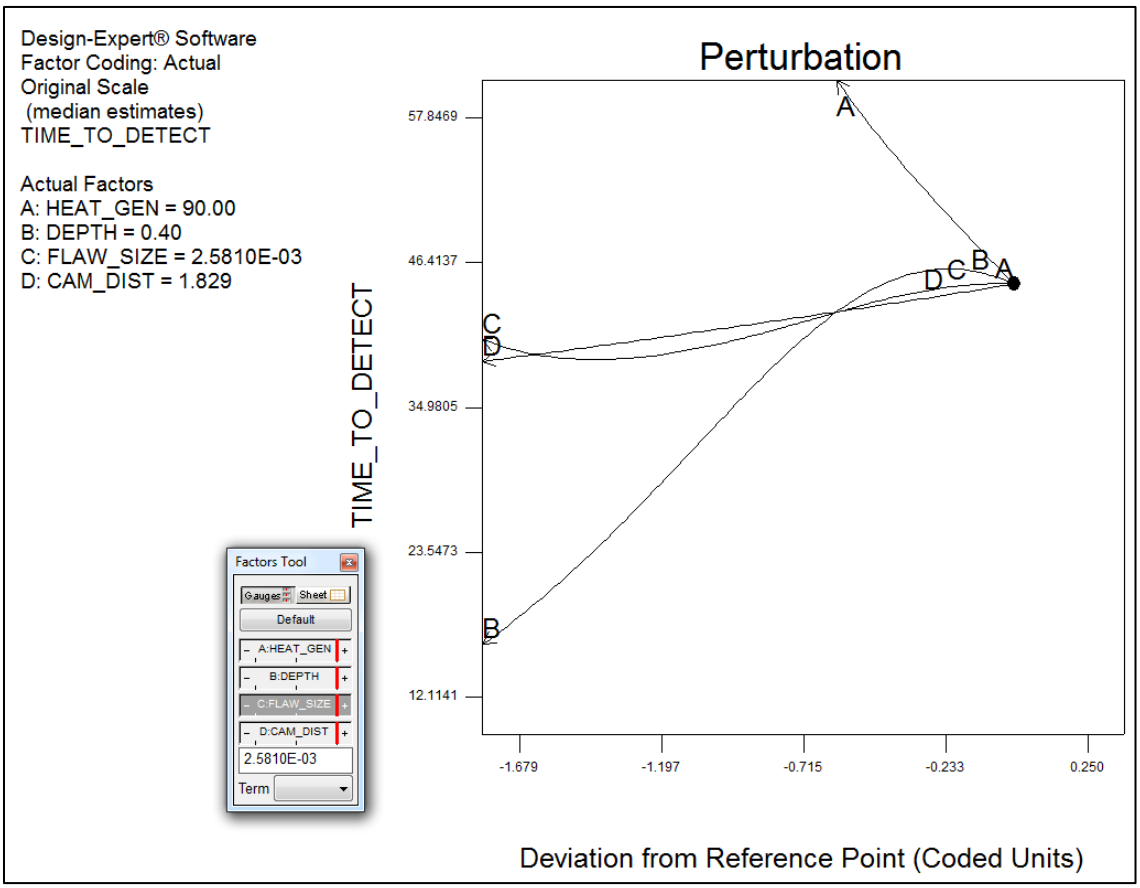

Figure 49. Perturbation analysis at region of model incorporating maximum parameter values.

And finally at the midpoint of the design sub-space, we again see that the Heat Generation Rate is the main driver, though the Detection Time response's sensitivity to Flaw Depth becomes more apparent within these last two figures (Figure 49 & Figure 50). This seems to be a common behavior for most regions under the influence of larger heat generation and flaw size values.

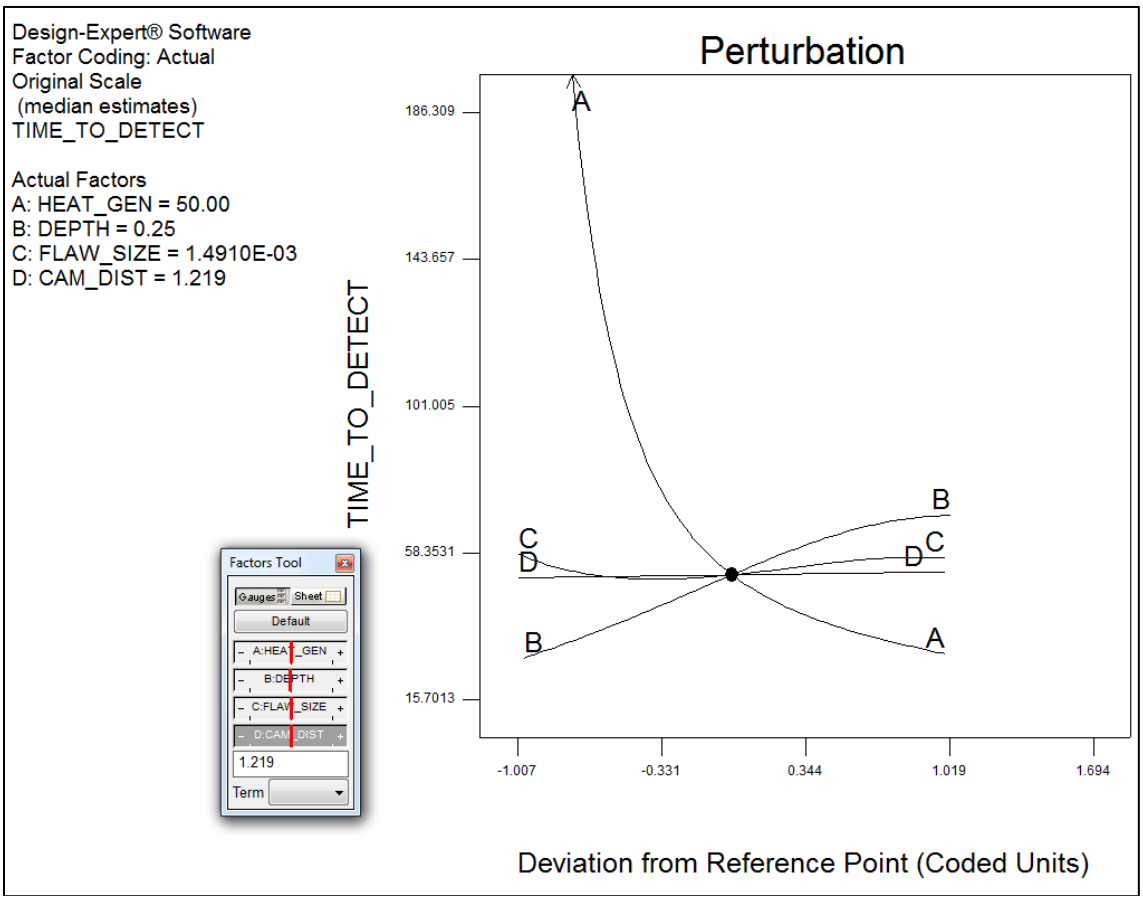

Figure 50. Effects of parameter perturbations at region at center of model space.

From each of the examples above, it is clear that the Heat Generation term definitely has a large impact on the time required to detect a flaw, and hence the likelihood of detection. Since empirical vibrothermographic testing will only occur over a finite span of time, the thermal detectability is highly sensitive to the heat generation value. It is evident, and unfortunate, that the single parameter that is under the direct control of the technician, the camera distance, has a minimal effect on detection time and likelihood of detection across most of the model space.

Thermal Diffusivity and its Effects on Flaw Detectability

Another interest of this research is whether differences in thermal diffusivity (due to variations in thermal conductivities between materials) significantly affect the detectability of flaws. For this purpose, multiple Parameter Permutated data sets, corresponding to models implementing various thermal conductivities, k, were created and analyzed. The test parameter combinations used during within each of these models were identical to those used during the original permutation analysis discussed earlier; the parameter sets are listed in Table 6 above. The material properties used in the models were identical to the values outlined in Table 7, with the exception of the orthotropic thermal conductivity coefficients, which were strategically varied during each analysis. The coefficients of thermal conductivity implemented within the model were altered in order to investigate the properties' effects on thermal detection time. Two additional cases, each using multiples of the original conductivity values were analyzed. The first alternative case utilized thermal conductivity coefficients that were one-half the original values (from Table 7) used, and the second alternative case utilized values that were twice that of the originals, the values of the coefficients are outlined in Table 8 below.

Table 8. Alternative Thermal Conductivity Coefficients for Thermal Diffusion Analyses

Variations of Thermal Conductivities			
Orthotropic Thermal Conductivity	Original	Decreased	Increased
k_x (W/mK)	0.44	.22	.88
k_y (W/mK)	0.44	.22	.88
k_z (W/mK)	0.35	.175	.70

After running parameter permutation analyses for both of the alternative cases, their results were compared to the results of the original analysis. The relationships between thermal conductivity and detection time appear to be fairly complex. A reduced thermal conductivity does not necessarily result in a definite reduction (or increase) in thermal detection time across the board. As has been demonstrated earlier, the parameter domain is fairly expansive. If data for only select portions of the parameter set combination are sample and analyzed, then certain trends within the detection time response can be discerned. The detection time data for these alternative cases were analyzed by first limiting observations to parameter sets which incorporate large generation areas (Flaw Size parameter) and which exclude lower heat generation values (Generation Rate $< 20W/m^2$). The detection time data, for the various parameter combinations, was analyzed in Excel® using conditional formatting. Examples of the data analysis are shown in Table 9 and Table 10 below. The detection time data corresponding to the original model (original thermal conductivity values, is reserved in Table 18 of Appendix B).

Table 9. Detection Times for Model using Decreased Thermal Conductivity Values

	Flaw Size, m^2=	0.002581	Generation Rate, W/m^2								
Cam Dist, m	**Depth**	**1**	**10**	**20**	**30**	**40**	**50**	**60**	**70**	**80**	**90**
0.6096	**0.1**	9999	102	46	32	24	20	18	16	14	14
	0.15	9999	130	64	46	36	32	28	26	24	22
	0.4	9999	282	154	116	96	84	76	70	64	60
	Flaw Size, m^2=	0.002581	Generation Rate, W/m^2								
Cam Dist, m	**Depth**	**1**	**10**	**20**	**30**	**40**	**50**	**60**	**70**	**80**	**90**
1.2192	**0.1**	9999	110	54	38	30	26	22	20	18	18
	0.15	9999	130	64	46	36	32	28	26	24	22
	0.4	9999	288	160	120	100	88	80	74	70	66
	Flaw Size, m^2=	0.002581	Generation Rate, W/m^2								
Cam Dist, m	**Depth**	**1**	**10**	**20**	**30**	**40**	**50**	**60**	**70**	**80**	**90**
1.8288	**0.1**	9999	110	54	38	30	26	22	20	18	18
	0.15	9999	130	64	46	36	32	28	26	24	22
	0.4	9999	290	160	122	102	90	80	74	70	66

Where: ## denotes an increase in detection time

denotes a decrease in detection time

denotes "Failure-to-Detect"

(no background color) denotes no change in detection time

Table 10. Detection Times for Model using Increased Thermal Conductivity Values

	Flaw Size, m^2=	0.002581	Generation Rate, W/m^2									
Cam Dist, m	**Depth**	**1**	**10**	**20**	**30**	**40**	**50**	**60**	**70**	**80**	**90**
0.6096	**0.1**	9999	178	60	34	24	20	16	14	12	10
0	**0.15**	9999	200	70	42	30	24	20	18	16	14
0	**0.4**	9999	286	124	82	64	52	46	40	36	34
	Flaw Size, m^2=	0.002581	Generation Rate, W/m^2									
Cam Dist, m	**Depth**	**1**	**10**	**20**	**30**	**40**	**50**	**60**	**70**	**80**	**90**
1.2192	**0.1**	9999	184	62	36	26	20	18	16	14	12
0	**0.15**	9999	200	70	42	30	24	20	18	16	14
0	**0.4**	9999	290	126	84	64	54	46	42	38	36
	Flaw Size, m^2=	0.002581	Generation Rate, W/m^2									
Cam Dist, m	**Depth**	**1**	**10**	**20**	**30**	**40**	**50**	**60**	**70**	**80**	**90**
1.8288	**0.1**	9999	186	62	36	26	20	18	16	14	12
0	**0.15**	9999	204	70	42	30	24	20	18	16	14
0	**0.4**	9999	296	126	84	66	54	48	42	38	36

Preliminary analysis shows a fairly definitive trend with regards to changes in detection time, between the different models. Decrease of the orthotropic thermal conductivity coefficients nearly always (for the majority of the parameter combinations being analyzed) leads to an increase in thermal detection time. Similarly, an increase in the conductivities tends to lead to a decrease in required detection times, though the trend is less pronounced in this instance. Keep in mind that these observed trends correspond only to parameter combinations incorporating large generation areas and lager heat generation values.

Regions of the parameter domains which incorporate small Flaw Size, and/or Low Generation rates seem to trend in a manner which is opposite to the observations made above (which again, were for larger Flaw Sizes and greater Heat Generations). These

regions tend to show decreased detection times for lower thermal conductivities, and increased detection times for higher thermal conductivities.

It must be again noted that the thermal detection time within these analyses are based upon certain detection criteria being achieved. The criteria set forth in the previous chapter (thermal detection area nodes must achieve an increase in temperature of at least 0.15K) was utilized for the alternative model analyses also. It is expected that for analyses using materials with fairly high thermal conductivities, the detection criteria implemented here might not give good estimations of whether a flaw's thermal signatures are captured by the IR camera. The reason being is that if a material's thermal conductivities are large enough to allow heat energy to diffuse through the material structure to a point where heat concentrations (immediately surrounding a flaw) can't be discerned, and rather a very large area of the structure heats up, then pin-pointing the origin of the heat source (flaw) might prove difficult. The current detection routine employed within the FE models however, would still predict the thermal detection of such flaw conditions, so long as the criteria had been satisfied. With this in mind, such a detection routine should be limited to use with materials of relatively low thermal conductivities.

ATTEMPTS TO VALIDATE THE FE MODELLING APPROACH THROUGH CORRELATION WITH EMPIRICAL DATA

Collection of Empirical Vibrothermographic Frequency-Sweep Data

Empirical Vibrothermographic frequency sweep tests were performed by Resodyn Corporation at the request of the MSU, in hopes of validating FE modeling procedures discussed in the previous section of this document. During these tests, the surface temperatures surrounding Flaws #2 and #3 were simultaneously measured with the IR thermographic camera system. The frequency-sweep testing procedure which was implemented spanned a frequency bandwidth of 10kHz to 30kHz, with sampling performed at every 100Hz increment. At each frequency, the high-frequency transducer was allowed to excite the plate for a period of 90seconds. At the end of the 90 second excitation period, the temperatures along the plate surface surrounding the flaws were sampled and recorded. This procedure was repeated for each frequency increment within the defined bandwidth. Once plate surface temperature data was recorded at each step within the entire bandwidth, the maximum surface temperatures occurring above each of the two tested flaws for each frequency were determined using various filtering algorithms. The frequency-histories of the maximum temperature gains for both flaws (#2 and #3) are displayed in Figure 51 below.

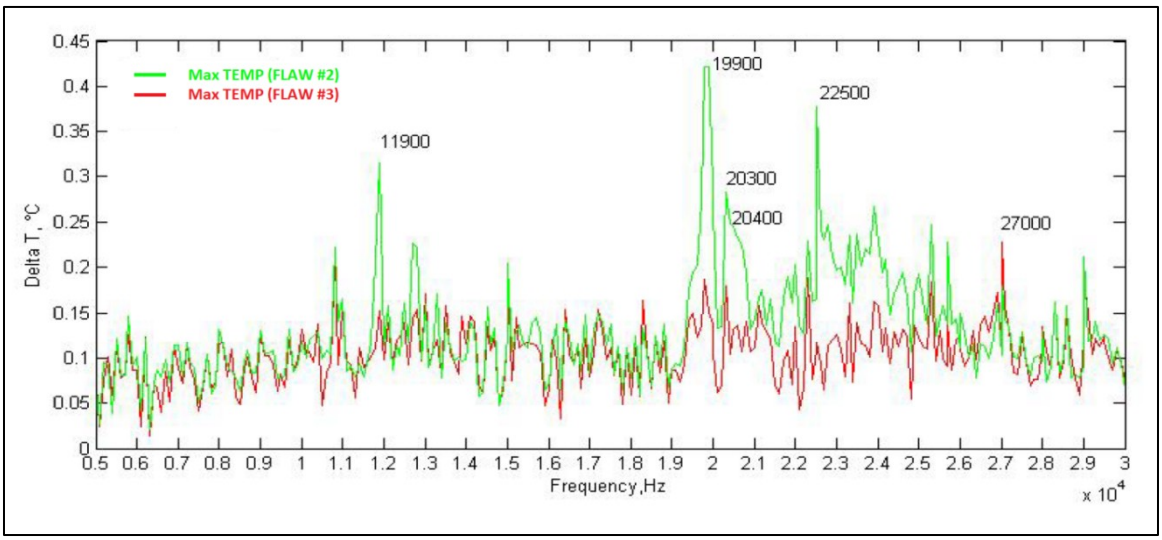

Figure 51. Maximum temperature gain frequency-histories for Flaw #2 and Flaw #3, determined during empirical testing. Courtesy of Resodyn Corporation.

From the data shown in Figure 51 , various temperature rise "peak" frequencies are immediately identifiable (these frequency values are called out within the plot). The data shows that the Flaw #2 exhibits numerous points within the frequency bandwidth at which thermal detection is realized (with regards the detection criteria discussed in this document). Observation of the Flaw #3 temperature rise data shows lower temperature response across the entire span of data, with the exception of a relatively prominent temperature peak occurring at 27,000Hz.

Comparison of Empirical and Predictive Detection Time Data

Qualitative comparisons were made between the empirical data presented above and the detection time predictions provided through the FE modeling/curve-fitting routines. The goal of the analysis was to correlate the frequencies at which thermal detection under the prescribed excitation time period of 90 seconds occur, with the

frequencies at which peak (definitely detectable) temperature rises occur within the empirical data set. This comparison was performed primarily by super-imposing the plotted predictive detection time results over the empirical test data plots. Examples of the superimposed plots are shown in Figure 52 & Figure 53. The secondary axis at the right hand side of each of the plots represents the time required for thermal detection for the "Detection Time" data of each graph.

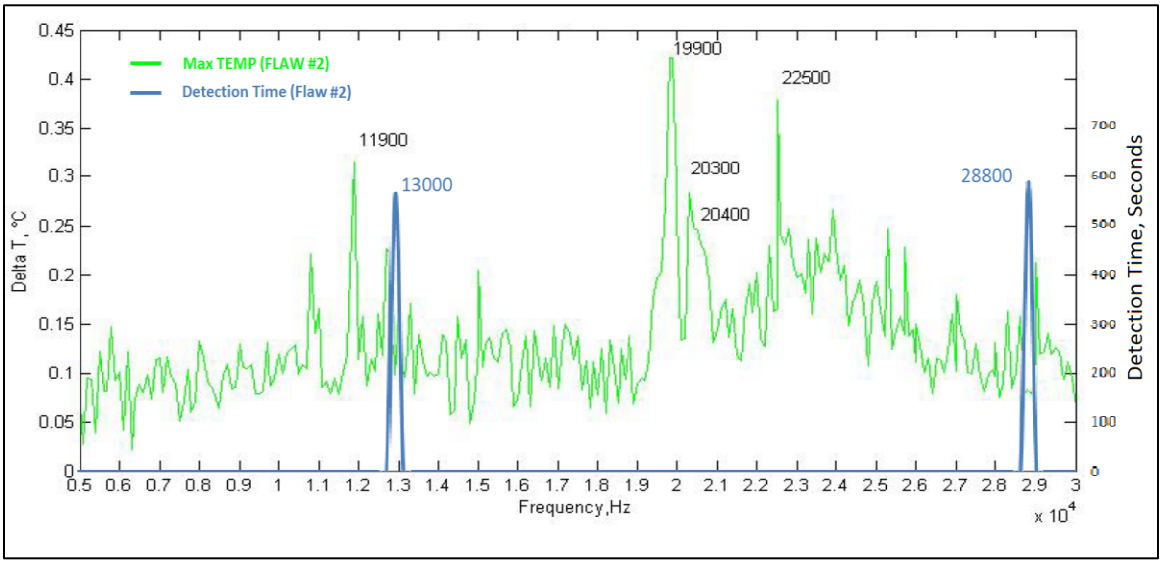

Figure 52. Comparison of frequencies at which temperature rise peaks and thermal detection time data occurs for Flaw #2. Detection time data corresponds to the secondary plot axis on the right hand side. Empirical maximum temperature data courtesy of Resodyn Corporation.

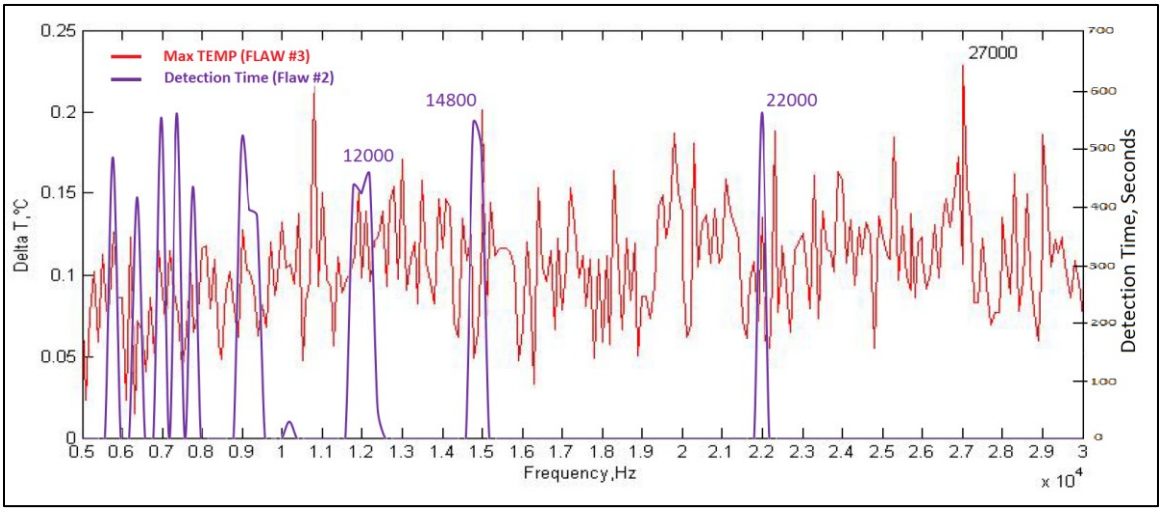

Figure 53. Comparison of frequencies at which temperature rise peaks and thermal detection time data occurs for Flaw #3. Detection time data corresponds to the secondary plot axis on the right hand side. Empirical maximum temperature data courtesy of Resodyn Corporation.

In Figure 52 it appears that the predictions of flaw detectability (non-zero detection time values) might possibly accurately predict a couple of the temperature rise peaks within the empirical data (albeit relatively small peaks). The quantity of data points is relatively small though, it would be premature to say the correlation is strong. The overlay of results for Flaw #3 is a bit more questionable, in the sense that the peaks appear to be nearly within the range of the average response (there are no exceptionally prominent response peaks.

An issue that must be addressed is the FE model approach's failure to predict the majority of detectable readings shown within the empirical data plots. As was discussed previously, significant differences between the manufactured plate design and the FE simulated models exist. The construction of flaws within the manufactured plate relied on inclusions of polyurethane film slip pairs. It's assumed that responses around the flaws of the manufactured plate aren't accurately represented within the FE analyses.

Correlation between the thermal detection prediction data and the empirical thermal detection data is decidedly inconclusive at best.

During preliminary vibrothermography testing procedures involving the manufactured plate, it was noted that heat signatures typically occurred predominantly around the border regions of each flaw. In fact, during many of the testing trial, the outlines of the flaws were clearly defined within the thermal IR data readings. An example of this heat localization is illustrated in the IR camera image capture within Figure 54.

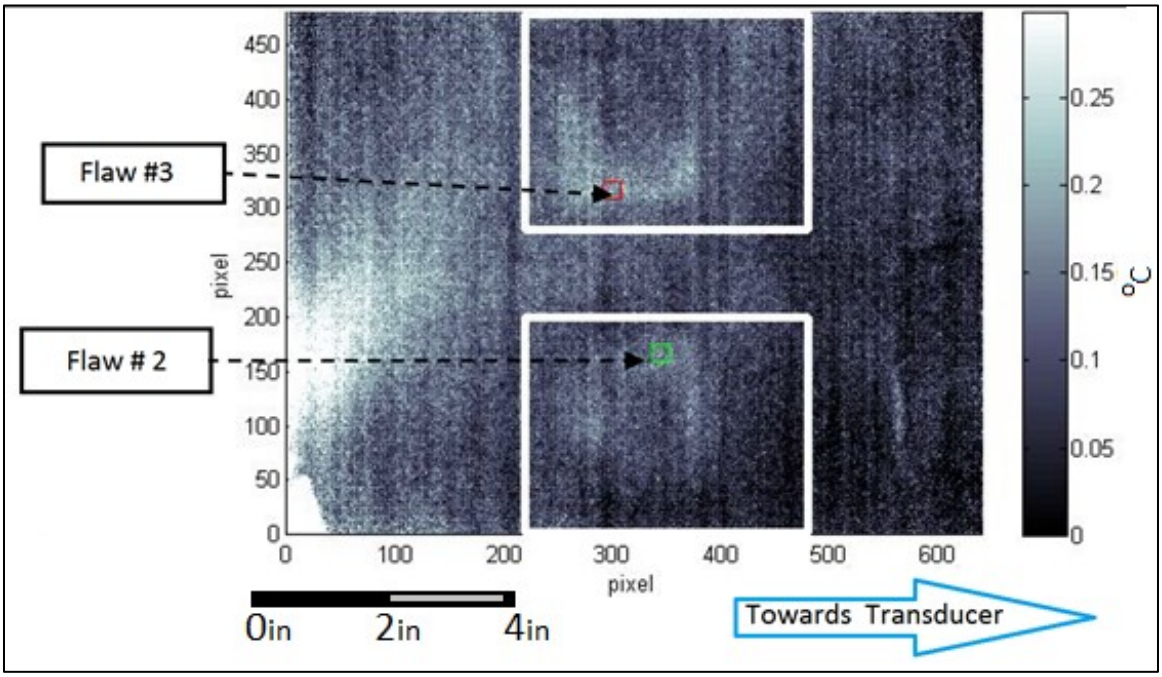

Figure 54. Infra-red thermographic image of Flaws #2 & #3, the outlines of the flaws can be discerned within the image.

The fact that heating occurs primarily around the boarders of each flaw, suggests that the film/tape inclusion flaws significantly affect the contact interactions along the flaw surfaces. FE analyses predicted that the majority of flaw surface shouldn't

experience any contact at all, let alone heat generation. Recall that according to the FE analysis results, static pre-loading of the plate structure forces the majority of flaw surfaces to become separated. This concept was investigated both within this document and in previous publications concerning this research [12, 13]; validation of highly localized contact was demonstrated by the FE results discussed within the publication.

PROCESS OUTLINE

Though positive model validation for frequency dependent frictional heat generations has yet to be confirmed, the procedures and methods outlined throughout this document provide a comprehensive strategy for modeling fully embedded flaws under frictional vibro-thermal response. It needs to be re-iterated that the procedures used here are dependent on the assumption that flaws are relatively small. A short discussion of how this process may be applied to arbitrary structures is discussed below, followed by a bulleted outline of the process.

Implementation of Method on Arbitrary Structures

Using FE modeling in an attempt to predict the detectability of flaws during vibrothermographic testing of a structure (or any type of response for that matter) is *highly dependent* upon the assumptions made in the modeling of the particular structure or system. With regards to the modeling algorithms outlined in this paper, the accuracy and reliability of the predictions for friction induced thermal response are predicated on an intimate knowledge of flaw area geometries and locations. The responses are also dependent on the assumptions made regarding boundary and loading conditions. At the current state, implementation of the methods outlined in this paper onto some arbitrary structure, with the goal of determining vibrothermographic response, would be pre-mature. The method is applicable only to structures which include damage regions where flaw characteristics and system conditions are known a priori. Thus it might initially seem that the process couldn't possibly be of any use in predicting vibro-thermal

responses within an arbitrary structure. On the contrary, there are perhaps particular situations in which these methods may be used characterize the vibro-thermal responses along regions of damage within arbitrary structures, and perhaps benefit the development of a routine to assess probability of detection for various types of flaws. For Instance, one of the ultimate extensions of this method could be in the analysis of certain groups of structures which experience *very* particular, commonly occurring forms of damage.

If a particular mode of failure which commonly occurs within a family of structures, can be exhaustively examined and accurately characterized (e.g. when this particular type of failure occurs, it commonly occurs at a particular region of the structure, and the extent of the damage is commonly bounded within a known region), then the preceding algorithms might be used to determine which frequencies (if any) can reliably produce detectible frictional-thermal responses such flaw sites. If the responses at those damage regions can be accurately and reliably characterized over a wide range of frequencies, and for a large array of additional testing parameters (perhaps transducer force, distance between flaw and transducer, etc.), then perhaps a reliable Vibrothermographic flaw detection testing routine for could be designed for that family of structures. Refinement of such a vibrothermographic testing routine through the use of these FE analyses could potentially increase the efficiency of such testing procedures, and drastically reduce required testing times; such a process might beneficially supplement large-scale NDE testing routines for mass-produced structures such as wind-turbine blades.

The process of characterizing flaw geometries (damage areas) within a structure (or family of structures), would require rigorous examination of large quantities of

samples. Furthermore, characterizing the vibrothermal responses at those flaws would also require exhaustive empirical vibrothermographic testing. Once such information has been collected and it can be determined the global modal/harmonic responses along members of particular groups of structures (mass-manufactured structures) are similar to one another, then perhaps those structures could be represented with a generic FE model which is representative of that family of structures.

In the end, if some commonly occurring flaw was extensively studied, and its responses to various testing parameters was accurately characterized, the use of Finite Element Analysis and the methods of this research could likely be used to refine testing procedures, and possibly identify optimal excitation frequencies. At a minimum the FE approach should be able to offer insight into some of the phenomena which might occur at the embedded flaw surfaces; the induced separations at the flaws, due to static pre-loading of the plate, which were noted in the research above are good examples of this.

Step by Step Outline of Procedure

The discussion above points explains some issues that must be addressed prior to implementing the methods explained in these documents with arbitrary structures. Throughout this document the algorithms used and the assumptions corresponding to those algorithms have been discussed in detail. Attempts at validating the FE model results with empirical data have also been explored. For ease of reference the methods and steps by which the various algorithms were designed and tested are outlined below in bulleted format for ease of reference.

Choose Structure (or Family of Structures) to be Analyzed and Modeled.

Modeling of Structure

- Define Assumptions Concerning Structure's Construction for the Purposes of FE Modeling (May Structure be Modeled as Composite, Multi-component, Monolithic etc.)
    - How Should Materials Be Represented within FE Models? (Isotropic, Orthotropic, etc.)

- Assess Behaviour of any Joints within Structure (Bolted Connections, Glued regions, Interference Fits, etc.)
    - Possibility for Large Scale Complex Contact Interactions (de-coupling/impact, nonlinear system stiffness etc...) within the Structure Should be Assessed First and Foremost.

      Possible Causes for Such Behaviour:
        - Large Damage regions
        - Non-rigid Structural support
        - Large Variances in Temperature During Testing
        - Transducer/Structure De-Coupling

- Estimate/Test for Material and System Properties of Physical Structure, for Implementation into FE Models (According to Modeling Assumptions)
    - for material properties
        - Young's Modulus
        - Shear Modulus
        - Mass Density
        - Poisson's Ratio
        - Thermal Conductivities
        - Thermal Capacitance
    - For System Properties
        - System Damping Ratios
          -Attempt to Characterize Damping Ratios through Empirical Testing (Half-Power Bandwidth Method)
          -Frequency Dependent, or Constant Damping Ratio Data Can be Employed within Models
        - Frictional Coefficients/ Friction Model
          -Select Appropriate Friction Model

- Assess Boundary and Loading Conditions that will be Present/Enforced within Structure during Empirical Testing.
    - Methods of Transducer Application
        - Fixed within Testing Structure?
        - Structural Pre-stressing due to Transducer Application?

- Self-Loading due to Gravity?

- Construct FE Models which Adequately Represent the Physical Structure Under Vibrothermographic Testing Conditions.

- Implement Contact/Target Elements at All Complex Contact Regions

Predict Modal frequencies and mode shapes of structure Using FE Modal Analysis

Characterize Vibrational Response of Structure

- Predict Modal frequencies and Mode Shapes of Structure through FE Modal Analyses

- Validate Modal Frequency Results with Empirical Testing (Sand Testing/ Sampling of Relative Accelerations)

Compile Harmonic Structural Response Data for Structure

- Define sub-model Cut-Boundary Regions

- Perform Harmonic Structural Response FE Analysis
  - Over Frequency Bandwidth of Interest
  - Define Solution Resolution (How Many Frequencies Should be Sampled)
  - If available, utilize displacement or force –frequency history data (determined through empirical testing)
  - Implement Damping Ratio Data
  - Save Harmonic Nodal Displacement Results at Sub-Model Cut-Boundary Regions

-If significant non-linear behaviours are expected, then harmonic response analysis should not be relied upon.
-Harmonic Analyses cannot account for transducer/structure de-coupling

Perform Transient Structural Sub-Model Analyses for Each Flaw

- Reduce Model-Size/Computational Costs by Analyzing Responses along Flaw Sub-Models.

- Implement Harmonic Cut-Boundary Nodal Displacements within Transient Structural Sub-model Analyses.

- Post-Process Transient Analysis Results and Estimate Average (per oscillation period) Frictional Heat Dissipation Rates and Corresponding Heat Contributing Surface Area Values.

- Perform FE Model Mesh-Refinement Solution-Convergence Analyses

- Perform Frequency Sweep Analysis for Each Flaw Sub-Model

- Analyze Heat Generation Results (across frequency band) Along Flaw Sites
    - Attempt to characterize the shapes of the heat contributing areas.

Create FE Thermal Diffusion Model

- Create Generic FE in order to Represent Heat Generation at Flaws within the Plate (or structure)
    - Parameterized Thermal Diffusion Model Allows for parameters:
        - Heat Generation Rate ,W/m^2
        - Flaw Size, m^2
        - Flaw Depth, % plate thickness
        - Camera Distance, m
    - Assume Generating Area Shape

- Perform Parameter Permutation Analysis (Vary Parameter Combinations) and Compile Comprehensive Data set which is Representative of Empirical Testing Conditions

Development of Thermal-Detection-Time Predictive Curve-Fit Equation

- Utilize Software (Design-Expert v.8®, MATLAB®, and Excel®) to Develop an acceptable Curve-fit Approximation of Data set.
    - Reduce Data and Model Size where Appropriate to Aid Curve-Fitting Processes
    - Apply Power Transformation to Curve-Fit Equation if Necessary

Attempt to Validate Thermal Detection Results

- Utilize Equation in Predicting Likelihood of Thermal Detection, and Thermal Times, for flaws which were analyzed within Frequency Sweep Analyses
- Attempt to Correlate Results with Empirical Data.
- If Positive Model Validation is Achieved, Continue On

***Utilize Developed Algorithms to Design a Robust Vibrothermographic Testing Routine**

- Analyze Vibrothermal Responses Along Flaws Using FE Methods
- Determine how Testing Parameters (static pre-loading for instance) influence the Vibrational Responses at the Flaw Surfaces
- Refine Vibrothermographic Testing Parameters Using What has been Learned

CONCLUSIONS

As was discussed in the previous section, correlations between empirical thermal detection data and the predictions made by ANSYS for the analyzed flaws are not overly strong. Though a positive validation of the particular FE modeling procedures used wasn't necessarily achieved, a considerable amount of progress has been made with regards to the characterization of such systems through the use of computer aided finite element modeling.

Through the experiences and knowledge gained during the research outlined in this document, numerous points for possible improvement with regards to FE modeling of the vibrothermographic method have been realized. The results of the FE modeling routines have not been substantially validated with regards to correlation with empirical data. At this point, one of the most glaring difficulties in achieving FE model validations is in manufacturing control samples that contain accurate representations of delamination flaws. Flaws within the test samples should ideally exist as simple void space, caused by crack propagation and material debonding. Reliably being able to produce fully-embedded delamination flaws of well-defined geometry however, is a very complicated task. With the goal of representing structural damages, similar to as they would likely occur in the field, in mind, inclusion of foreign materials to produce delamination flaws may not be the best approach. If such inclusions significantly alter the local responses surrounding the area damage, when compared to a void delamination, then attempts to validate the FE modeling procedures as outlined here, may be for naught.

Future empirical testing and FE model validation procedures should investigate the effects of different types of inclusions. It would be interesting to see how the vibrothermographic results surrounding flaws of different constructions would vary. For example, it might be useful to determine whether an inclusion consisting of a single slip of polyurethane film would produce vibrothermographic responses similar to the inclusions utilized in this research.

Furthermore, the effects of inclusion of foreign materials might be mitigated if the material properties of the inclusion are similar (if not identical) to the host structure's material. In this vein, a different approach to inclusion manufacture is suggested. If the same epoxy material that was used in construction of the plate, was used to create two very thin flat slips upon a tooling surface, (by basically pouring the material over a flat surface) which could then be separated from the tool surface and joined together using an appropriate adhesive, then a slip-pair inclusion incorporating identical material properties could be created and implemented within the plate. Some differences in porosity between the host material and the inclusion, due to manufacturing method, would surely exist however. The epoxy inclusion would also likely have to be properly dressed and possibly chemically treated or doped, in order to promote adequate bonding between it and the host material.

In the case of future attempts to validate the FE modeling procedures as outlined in this document, manufacture of the composite plates should be limited to plates with relatively few flaws (perhaps 3 or less, rather than 9), if the assumption that flaws don't significantly affect the global response of the plate/transducer system is to remain a reliable approximation.

The novel approach to predicting thermal detection times, using FEA derived detection time data and curve-fitting procedures, seems to have promise. More accurate estimation of detection times may be possible with improvements to modeling detection criteria algorithms. Due to the manner in which the current thermal analysis model was defined, the system is expected to offer better approximations for flaws occurring at greater depths within the plate and for flaws which exhibit more circular localized heat producing regions. Further improvements to this model might include implementation of algorithms which account for variable heat generation patterns (other than circular localizations). Another possible direction for this method might be to utilize the actual heat generation distributions (averaged over an oscillation period) derived in the transient structural analyses. Providing a comprehensive data set of thermal detection time data for the process of curve-fitting however, might prove to be difficult.

If the thermal detection time responses of flaws didn't necessarily have to be characterized through the use of a "system-wide" empirical equation, then perhaps a better method for characterizing thermal detection time responses at any point within the model space would be to utilize spline or even linear data interpolations. Such a method might include compiling an all-inclusive data set of thermal detection time responses, similar to the one created using methods outlined in this document. From that data set, MATLAB could be used to interpolate thermal detection time data at any point within the data space. Using this method, frequency dependent heat generation and contributing area data could be used to predict likelihood of detection and thermal detection times.

In the future, if a positive validation of results between the FE plate modeling and empirical results can be ascertained, then it might be possible to utilize FE modeling in an

attempt to characterize the effects that system resonance may have on heat generation along flaws. With regards to the information obtained throughout the research discussed in this document, drawing a conclusion on what effects resonance has on flaw heat generation would be premature.

REFERENCES CITED

Sabokkatakin, A. Ibarra-Catanedo, C. Bendada, A. Maldaque, X. Bison, P. Grinzato, E. and Marinetti, S. (2010) 'Finite element analysis of heat generation in ultrasonic thermography' paper presented at 10th International Conference on Quantitative InfraRed Thermography, Québec Canada, 27-30 July 2010.

E.G Heneke, K.L. Reifsnider, W.W. Stinchcomb. Vibrothermography: Investigation, development, and application of a new nondestructive evaluation technique. Technical Report, U.S. Army Research Office, 1986.

ANSYS® *Academic Research*, release number 14.0 ,Help System, Element Library, ANSYS, Inc.

Dimarogonas, A.D., Haddad, S. (1992). Vibration for engineers. *Continuous Systems* (p. 412). Englewood Cliffs, NJ: Prentice Hall.

Gatti, P.L., Ferrari, V. (1999). Applied structural and mechanical vibrations: Theory, methods and measuring instrumentation. *Multiple-degree-of-freedom systems (pp.266-270).*New York, NY: Routledge

ANSYS® *Academic Research*, release number 14.0 ,Help System, Structural Analysis Guide 1-4, ANSYS, Inc.

Dimarogonas, A.D., Haddad, S. (1992). Vibration for engineers. *Forced harmonic vibration*(pp. 142-144). Englewood Cliffs, NJ: Prentice Hall.

Swevers, J., F. Bender, C.G. Ganseman and T. Prajogo (2000). "An integrated friction model structure with improved presliding behavior for accurate friction compensation." *IEEE Transactions on Automatic Control* **45**: 675-685.

Kishore, J., P. Sampathkumaran, S. Seetharamu, P. Thomas, M. Janardhana (2005). "A study on the effect of the type and content of filler in epoxy–glass composite system on the friction and slide wear characteristics." *Wear* **259**: 634-641

Saboktakin,A., C. Ibarra-Castanedo, A. Bendada, X. Maldague, "Analysis of ultrasonic elastic waves in vibrothermography using FEM", Sixth International Workshop, Advances in Signal Processing for Non Destructive Evaluation of Materials (IWASPNDE), London, Ontario, Canada, 25-27 August 2009.

Schön, J. (2000). "Coefficient of friction of composite delamination surfaces." *Wear* 237: 77-89

Peter Lucon, Kyle Kapp. Vibration induced temperature changes for verification of heat conduction/generation model. Technical Report, Resodyn Corporation, July 2011.

Platt, D. (2012). Development of effective numerical schemes for frictional heat generation and diffusion in vibrothermography. Unpublished master's thesis for master's degree., Montana State University, Bozeman Montana, USA

ANSYS® *Academic Research*, release number 14.0 ,Help System, Structural Analysis Guide 3.8.7, ANSYS, Inc.

ANSYS® *Academic Research*, release number 14.0 ,Help System, Contact Technology Guide 3.9.5.4, ANSYS, Inc.

APPENDICES

APPENDIX A

ADDITIONAL SOLUTION MESH/CONVERGENCE DATA

Table 11. Element Mesh Refinement Convergence Data, Heat Generation, SET 2

No. of Contact Elements	Contact Element Edge Length, (m)	Avg. Frictional Heat Dissipation, (W/m^2)	Percent Change Between Values
144	0.004478	2.8594	--
576	0.002239	3.6000	25.92%
1296	0.001493	4.3102	19.71%
2304	0.00112	5.0890	18.07%
Driving Frequency, (Hz)		**17600**	

Table 12. Element Mesh Refinement Convergence Data, Heat Contributing Area, SET 2

No. of Contact Elements	Contact Element Edge Length, (m)	Total Contributing Area, (m^2)	Percent Change Between Values
144	0.004478	1.79-4	--
576	0.002239	7.26E-4	305%
1296	0.001493	7.81E-4	7.54%
2304	0.00112	8.73E-04	11.78%
Driving Frequency, (Hz)		**17600**	

Table 13. Element Mesh Refinement Convergence Data, Heat Generation, SET 3

No. of Contact Elements	Contact Element Edge Length, (m)	Avg. Frictional Heat Dissipation, (W/m^2)	Percent Change Between Values
144	0.004478	2.213	--
576	0.002239	2.668	20.56%
1296	0.001493	2.934	9.97%
2304	0.00112	2.843	-3.11%
Driving Frequency, (Hz)		**27600**	

Table 14. Element Mesh Refinement Convergence Data, Heat Contributing Area, SET3

No. of Contact Elements	Contact Element Edge Length, (m)	Total Contributing Area, (m^2)	Percent Change Between Values
144	0.004478	1.79E-04	1.79E-04
576	0.002239	4.48E-04	4.48E-04
1296	0.001493	5.93E-04	5.93E-04
2304	0.00112	5.97E-04	5.97E-04
Driving Frequency, (Hz)		**27600**	

APPENDIX B

THERMAL DETECTION TIME (FE PREDICTED) DATA

Table 15. Detection Times, Flaw Size equals 0.000129m^2

	Flaw Size, m^2=	0.000129	Generation Rate, W/m^2									
Cam Dist, m	**Depth**	**1**	**10**	**20**	**30**	**40**	**50**	**60**	**70**	**80**	**90**
0.6096	**0.1**	9999	9999	72	32	22	16	14	12	10	10
	0.15	9999	9999	130	52	34	26	22	20	18	16
	0.4	9999	9999	9999	316	160	110	86	72	64	90
	Flaw Size, m^2=	0.000129	Generation Rate, W/m^2									
Cam Dist, m	**Depth**	**1**	**10**	**20**	**30**	**40**	**50**	**60**	**70**	**80**	**90**
1.2192	**0.1**	9999	9999	154	52	32	24	18	16	14	12
	0.15	9999	9999	290	82	48	36	30	24	22	20
	0.4	9999	9999	9999	526	242	158	120	98	86	76
	Flaw Size, m^2=	0.000129	Generation Rate, W/m^2									
Cam Dist, m	**Depth**	**1**	**10**	**20**	**30**	**40**	**50**	**60**	**70**	**80**	**90**
1.8288	**0.1**	9999	9999	1020	168	84	56	42	34	30	26
	0.15	9999	9999	-5	232	110	74	56	44	38	34
	0.4	9999	9999	9999	1140	410	252	184	146	122	106

Table 16. Detection Times, Flaw Size equals 0.000401m^2

	Flaw Size, m^2=	0.000401	Generation Rate, W/m2								
Cam Dist, m	**Depth**	**1**	**10**	**20**	**30**	**40**	**50**	**60**	**70**	**80**	**90**
0.6096	**0.1**	9999	166	42	26	18	16	14	12	10	10
	0.15	9999	240	60	36	28	22	20	18	16	14
	0.4	9999	940	176	104	78	64	56	50	46	42
	Flaw Size, m^2=	0.000401	Generation Rate, W/m2								
Cam Dist, m	**Depth**	**1**	**10**	**20**	**30**	**40**	**50**	**60**	**70**	**80**	**90**
1.2192	**0.1**	9999	194	44	26	18	16	14	12	10	10
	0.15	9999	286	64	38	28	24	20	18	16	14
	0.4	9999	1236	196	114	84	68	60	52	48	44
	Flaw Size, m^2=	0.000401	Generation Rate, W/m2								
Cam Dist, m	**Depth**	**1**	**10**	**20**	**30**	**40**	**50**	**60**	**70**	**80**	**90**
1.8288	**0.1**	9999	274	52	28	20	16	14	12	10	10
	0.15	9999	404	74	42	30	24	20	18	16	14
	0.4	9999	-5	244	136	98	80	68	60	54	50

Table 17. Detection Times, Flaw Size equals 0.000401m^2

	Flaw Size, m^2=	0.000674	Generation Rate, W/m^2								
Cam Dist, m	**Depth**	**1**	**10**	**20**	**30**	**40**	**50**	**60**	**70**	**80**	**90**
0.6096	**0.1**	9999	128	42	26	18	16	14	12	10	10
	0.15	9999	170	58	38	28	24	20	18	18	16
	0.4	9999	406	140	92	72	60	54	48	44	42
	Flaw Size, m^2=	0.000674	Generation Rate, W/m^2								
Cam Dist, m	**Depth**	**1**	**10**	**20**	**30**	**40**	**50**	**60**	**70**	**80**	**90**
1.2192	**0.1**	9999	134	42	26	18	16	14	12	10	10
	0.15	9999	180	58	38	28	24	20	18	18	16
	0.4	9999	446	148	96	76	64	56	50	46	44
	Flaw Size, m^2=	0.000674	Generation Rate, W/m^2								
Cam Dist, m	**Depth**	**1**	**10**	**20**	**30**	**40**	**50**	**60**	**70**	**80**	**90**
1.8288	**0.1**	9999	150	42	26	18	16	14	12	10	10
	0.15	9999	200	60	38	28	24	20	18	18	16
	0.4	9999	518	162	104	80	66	58	52	48	44

Table 18. Detection Times, Flaw Size equals 0.002581m^2

	Flaw Size, m^2=	0.002581	Generation Rate, W/m^2								
Cam Dist, m	**Depth**	**1**	**10**	**20**	**30**	**40**	**50**	**60**	**70**	**80**	**90**
0.6096	**0.1**	9999	124	48	30	24	18	16	14	12	12
	0.15	9999	150	62	40	32	26	22	20	18	16
	0.4	9999	266	132	92	74	64	56	52	48	44
	Flaw Size, m^2=	0.002581	Generation Rate, W/m^2								
Cam Dist, m	**Depth**	**1**	**10**	**20**	**30**	**40**	**50**	**60**	**70**	**80**	**90**
1.2192	**0.1**	9999	130	52	34	26	22	18	16	16	14
	0.15	9999	150	62	40	32	26	22	20	18	16
	0.4	9999	270	134	96	78	66	58	54	50	46
	Flaw Size, m^2=	0.002581	Generation Rate, W/m^2								
Cam Dist, m	**Depth**	**1**	**10**	**20**	**30**	**40**	**50**	**60**	**70**	**80**	**90**
1.8288	**0.1**	9999	130	52	34	26	22	18	16	16	14
	0.15	9999	150	62	40	32	26	22	20	18	16
	0.4	9999	272	134	96	78	66	60	54	50	46